Spring 1-1-2018

Direct Generation of Oxygen via Electrocatalytic Carbon Dioxide Reduction with an Ionic Liquid

Jordan Barr Holquist
University of Colorado at Boulder, jholquist@gmail.com

DIRECT GENERATION OF OXYGEN VIA ELECTROCATALYTIC CARBON DIOXIDE REDUCTION WITH AN IONIC LIQUID

By

JORDAN BARR HOLQUIST

B.S., University of Illinois at Urbana-Champaign, 2012

M.S., University of Colorado Boulder, 2014

A thesis submitted to the

Faculty of the Graduate School of the

University of Colorado in partial fulfillment

of the requirement for the degree of

Doctor of Philosophy

Ann and H.J. Smead Department of Aerospace Engineering Sciences

University of Colorado, Boulder, CO

2018

This thesis entitled:

Direct Generation of Oxygen via Electrocatalytic Carbon Dioxide Reduction with an Ionic Liquid

written by Jordan Barr Holquist

has been approved for the Department of Aerospace Engineering Sciences

_____

David M. Klaus, Ph.D.

_____

James A. Nabity, Ph.D.

Date_____

The final copy of this thesis has been examined by the signatories, and we

Find that both the content and the form meet acceptable presentation standards

ABSTRACT

Holquist, Jordan Barr (Ph.D., Aerospace Engineering Sciences)

Direct Generation of Oxygen via Electrocatalytic Carbon Dioxide Reduction with an Ionic Liquid

Thesis directed by Professor David M. Klaus

The feasibility of long duration crewed space exploration missions will depend on the supply of consumables, such as oxygen, to keep the crew alive. Air revitalization is a function of environmental control and life support systems (ECLSS) employed on any crewed spacecraft. On longer duration missions, such as on the International Space Station (ISS), resource regeneration reduces the amount of consumables that must be provided for the mission. Systems on the ISS recover O_2 from metabolically produced CO_2, which itself is collected from the ISS cabin where astronauts live and work. The current state-of-the-art for O_2 recovery onboard the ISS can only recover up to 54% of the O_2 available in respired CO_2 and relies on the resupplied H_2O to the ISS. An alternative O_2 generation process is solvated electrochemical CO_2 reduction, enabled in spacecraft environments by using a non-volatile ionic liquid (IL) solvent, electrolyte, and catalysis promoter. An electrochemical CO_2 reduction system (ECRS) could improve O_2 recovery from CO_2 by up to 70%, or it could function to recover 50% O_2 from CO_2 without a net water loss, which can be advantageous in missions where in-situ resource utilization (ISRU) of Martian atmospheric CO_2 is desired. Ionic liquid supported electrochemical CO_2 reduction is evaluated to determine its feasibility for space applications. The requirements, sizing, and challenges of including an ECRS are considered for various possible ECLSS or ISRU architectures. The current state-of-the-art for IL supported CO_2 electrolysis is reviewed, and selections of ILs studied experimentally in this work are presented and justified. Thermophysical properties of the ILs as neat and aqueous solutions are measured to aid in understanding and design of the ILs themselves and in systems using them. Aqueous IL solutions are studied using cyclic voltammetry and constant potential electrolysis with gaseous product analysis to determine if and how the selected ILs promote electrochemical CO_2 reduction. A concept for a vacuum-assisted product removal

(VAPR) CO_2 electrolyzer is presented as a possible solution to space application environmental conditions and requirements, and the concept is demonstrated through the design and testing of a prototype electrolyzer.

This work was supported by a NASA Space Technology Research Grant (NNX14AL72H)

This dissertation is dedicated to anyone who dreams and dares to travel to space:

I hope you get there.

ACKNOWLEDGEMENTS

First, I would like to sincerely thank my advisor, David Klaus, for his unwavering support of my education and research throughout my M.S. and Ph.D. I have been lucky to get to share many discussions with him through the years; his encouragement, insights, and advice have been indispensable to me. Dr. Klaus' trust in my efforts to push through challenges has been pivotal on my path to becoming an independent researcher, and I will be forever grateful to him. I also wish to thank my committee members, James Nabity, Allison Anderson, Carl Koval, and Morgan Abney, for serving on my committee. All of them have opened new doors for me, provided critical feedback on my research, and have assisted me in any way they could whenever I asked. They have all been such a pleasure and an inspiration to work with.

There have been so many students and coworkers that I have had the fortune to get to know and become friends with during my time at Colorado. The entire bioastronautics research group is an incredible group of people from whom I would learn new things from every day, and I look forward to seeing them all again throughout our future careers. I want to particularly thank Christine Fanchiang and Chris Massina who made me feel like part of the research group and who were my role models for PhD students when I arrived at Colorado. I could not have made it through the day to day of independent research without the support of my office mate, Emily Matula, right there in the trenches with me. I'd like to sincerely thank Adrian Stang for having the patience and good nature to teach me the critical skills of machining and designing parts for machining. And also a big thanks to Maggie Kolicko and Joanie Wiesman in the accounting department for their support through the years.

This work and the many experiences I had could not have been possible without the support of the NASA Space Technology Research Fellowship (NSTRF). Because of it, I was able to work with and learn from some of the best and brightest at NASA and at the Department of Energy's Joint Center for Artificial Photosynthesis (JCAP). I wish to thank everyone for welcoming and teaching an eager PhD student that showed up at your offices one day: David Donovan, Laurel Karr, Mark S. Paley, Tony Muscatello, Tracy

Gibson, Paul Hintze, Chenxiang Xiang, Lihao Han, Ryan Jones, and Brian Markowicz. I'd also like to thank John Graf and Craig Broerman for providing assistance at a moment's notice when I needed it most.

Outside of my research, I met some of the best friends I've ever had while living in Colorado, and I am so grateful for their support and friendship. Tyler Mixa and Jake Mashburn, who both started at Colorado with me at the same time, and who stayed until the end, were the foundations of my life in Boulder. They, along with Ann Dietrich, Viliam Klein, Trey Laurence, Bryan Costanza, and Valeria Serrano, are such dynamic, exciting, and caring people that have made my life so much more interesting, enjoyable, and fulfilling just for knowing them.

I would especially like to thank my parents, for their unconditional love and support of my dreams. My father, Bob Holquist, instilled the idea of creativity in me at a young age; he taught me to create new things and not to fear failing, so long as I was trying. Lastly, I want to my express my sincere gratitude to and appreciation for my mother, Debi Barr-Holquist. I could not have done any of this without you, as you have provided me with the confidence, support, and love that have allowed me to take big risks and hope for the best.

Table of Contents

List of Tables

List of Figures

Chapter 1 – Research Motivation and Objectives

1.1 Motivation

Environmental Control and Life Support Systems (ECLSS) that can recycle human metabolic waste products back into usable consumables for crew survival, such as water, oxygen, and food, are critical to the feasibility of long distance and long duration crewed space exploration missions. By recycling wastes into consumables instead of bringing all the consumable supplies outright, the initial mass that must be launched from Earth with a human crew to keep them alive and healthy during a mission can be reduced considerably. Recovery of oxygen from carbon dioxide is one area of air revitalization loop closure that can be improved from the current state of the art to reduce the burden of oxygen supply to future missions. Also, because it is well known that carbon dioxide exists in the atmosphere of Mars, the development of carbon dioxide reduction technologies can promote in-situ resource utilization (ISRU), which could further enable the feasibility of human exploration and habitation on the surface of Mars.

Carbon dioxide reduction is already accomplished on the International Space Station (ISS) by the Carbon dioxide Reduction Assembly (CRA), a Sabatier reactor, working with the Oxygen Generator Assembly (OGA), a water electrolysis reactor. At most, these two assemblies together can recover 54% of the available O_2 in metabolically produced CO_2. The limiting factor of this process is the loss of hydrogen in the methane byproduct of the Sabatier reaction. Therefore, it is desirable to investigate and develop technologies that recover O_2 from CO_2 without the loss of hydrogen. Such processes that could improve upon this state-of-the-art include the Bosch reaction series, biological photosynthesis, and carbon dioxide electrolysis in the form of either solid oxide electrolysis or solvated CO_2 electrolysis. While the first three processes have received considerable attention, improvements in solvated CO_2 electrolysis have only recently introduced the possibility of using it in a crewed spacecraft or space habitat environment.

1.2 Overview of Objectives

This dissertation investigates the feasibility of using an ionic liquid (IL)-based electrochemical CO_2 reduction process for the generation of O_2 in spacecraft ECLSS and planetary surface ISRU architectures to enable long duration, crewed space exploration missions. The primary design of this concept converts CO_2 to CO and O_2 in a process that is water-neutral, as water is both oxidized at the anode of the electrolyzer and produced from generated protons and a reclaimed oxygen atom at the cathode alongside CO_2 reduction. The possible reaction pathways, critical electrolyzer design parameters, and state-of-the-art performance metrics related to such a process are reviewed and discussed in terms of how they would affect space exploration applications, and first order sizing estimates for an electrochemical CO_2 reduction system (ECRS) are made based on possible crew sizes and heuristic data from the water electrolyzer OGA on the ISS. Experiments and analysis were performed to measure properties of new IL-aqueous solutions and the performance of these solutions in aiding CO_2 electrolysis. A prototype reactor was designed and tested with the aim to alleviate critical challenges to using an ECRS in a microgravity environment, and while the concept of its operation was proven, many lessons can be learned from the issues of developing and operating such an electrolyzer.

The primary objectives of this research were to:

1. Analyze the performance requirements for an electrochemical CO_2 reduction system for various crewed space exploration mission scenarios and provide a first order estimate of the system sizing, power requirements, and the theoretical O_2 recovery efficiency of the different architectures
2. Identify, select, and synthesize or procure ionic liquids that may be conducive to supporting CO_2 electrolysis, and measure their relevant thermophysical properties in aqueous solutions
3. Parametrically characterize the influence of various ILs in aqueous solutions on the performance of solvated CO_2 electrolysis
4. Design and develop a prototype electrochemical reactor capable of operating in conditions relevant to supporting air revitalization needs of a crew in a space habitat

5. Analytically assess the challenges and opportunities of implementing an ECRS in various missions with relevant upstream and downstream processes and systems, with considerations for microgravity and low-gravity environments

1.3 Dissertation Overview

In addition to Chapter 1, Chapter 2 introduces the crewed space exploration mission constraints and requirements as well as relevant technologies being used and researched for O_2 recovery via CO_2 reduction. Further, the latter sections of Chapter 2 delve more deeply into introductory electrochemistry fundamentals, as well as the background and current state-of-the-art for solvated CO_2 electrolysis with and without ionic liquids. With this knowledge in hand, Chapter 3 analytically assesses the opportunities and challenges related to how an electrochemical CO_2 reduction system can be implemented in various space exploration mission architectures, providing a first order estimation of performance requirements and sizing of a practical system. Chapter 4 discusses the considerations for selecting an IL to use and the justifications for the ILs that were procured, synthesized, and studied in this research. Chapter 4 concludes with experimental results from measuring the thermophysical properties of ILs in binary aqueous solutions throughout the entire composition range. Chapter 5 presents experimental methods and results of the performance of each IL in supporting electrochemical CO_2 reduction, including cyclic voltammetry and constant potential electrolysis with gaseous product quantification, with relevant analyses and discussion of the results. In Chapter 6, the design, development, and experimental assessment of a prototype electrochemical flow cell with a novel vacuum-assisted product removal (VAPR) functionality is presented with analyses and discussion of the results. Finally, Chapter 7 provides conclusions made from this research as to the feasibility of implementing an IL-based ECRS in ECLSS and ISRU architectures for crewed space exploration missions, as well as an assessment of the future work needed to further develop this type of technology.

Chapter 2 – Investigation Rationale and Background

2.1 Introduction

Air revitalization is a necessary function to sustain a safe and breathable atmosphere for humans to live and work in a spacecraft or habitat. In spacecraft that support short duration human missions, this is accomplished largely by capturing carbon dioxide (CO_2) and trace contaminants with adsorptive materials, while supplying oxygen (O_2) from either chemical or physical storages. These open-loop methods become prohibitively expensive from mass and volume standpoints as mission durations increase to the order of months and years, necessitating recycling air handling systems with a high degree of consumable resource loop closure. As part of an environmental control and life support system (ECLSS), reduction of CO_2 to recover O_2 is one function of an air revitalization architecture that can offer considerable consumables mass savings. By capturing CO_2 exhaled from crewmembers (CMs) and processing it to recover O_2 from the CO_2 molecule, a breathable atmosphere can be maintained for longer with less O_2 initially supplied before launch. Similarly, if a human crew lands on Mars, CO_2 from the Martian atmosphere can be captured and processed to provide O_2 as an in-situ resource. Carbon dioxide capture and reduction, then subsequent O_2 generation, are currently accomplished by systems on board the International Space Station (ISS). The current ECLSS configuration is capable of recovering approximately 47–52% of the O_2 available in metabolically generated CO_2 "due to a shortage of H_2 in the system [on the ISS]." (Gatens, Anderson, Broyan, Macatangay, & Shull, 2015; Lange, French, Abney, & Barta, 2018). This has been adequate for the ISS, due to the frequency with which resupply vehicles can be launched from Earth to low Earth orbit (LEO).

2.1.1 Problem Statement

As human space exploration missions venture further away from Earth, resupply becomes more difficult and expensive and improved consumable recycling becomes vital to reduce the initial launch mass of such future missions. Each crew member (CM) nominally consumes 0.816 kg of O_2 per day and exhales 1.04 kg of CO_2 per day (M. S. Anderson, Ewert, Keener, & Wagner, 2015). To put these rates into the

perspective of a possible 5-year trip to and from Mars[1], a crew of 4 would consume 6,096 kg of O_2 and exhale 7,286 kg of CO_2. By recovering all the O_2 available in the metabolically generated CO_2, it is theoretically possible to regenerate up to 0.756 kg O_2 per crew member per day (1/CM-d), or about 92% of the metabolically required O_2 consumption of each crew member. In this example, such recovery would shrink the oxygen deficit from 6,096 kg of O_2 to just 488 kg of O_2. Metabolic conversion of O_2 to water ("Metabolic Water") accounts for the remaining deficit and necessitates water electrolysis in any complete O_2 recovery system. Similarly, in an O_2 recovery system with less than 100% recovery of O_2 from CO_2, water electrolysis is the preferred method of providing additional O_2 (rather than gas tanks), and requires extra payload mass of water in the initial launch. The current state-of-the-art (SOA) for O_2 recovery is only theoretically capable of recovering 54% O_2 from CO_2, and practically capable of less than 50% O_2 recovery (Gatens et al., 2015). Therefore, in the most recent Technology Roadmap Assessment, NASA defined 75–90% O_2 recovery from CO_2 to be a mission *enabling* technology goal for scenarios including a crewed visit to a near Earth asteroid (NEA), the lunar surface, Martian moons, Martian orbit, and the Martian surface ("NASA Technology Roadmaps TA 6: Human Health, Life Support, and Habitation Systems," 2015; "NASA Technology Roadmaps TA 7: Human Exploration Destination Systems," 2015).

A long duration stay on the surface of Mars provides a unique opportunity where the need for such high efficiency for O_2 recovery from CO_2 is not necessary, due to the relative abundance of CO_2 in the Martian atmosphere. In-situ resource utilization (ISRU) of atmospheric CO_2 could provide all the O_2 required for a crewed surface habitat if the CO_2 reduction unit could operate *without* the consumption of hydrogen. In addition, a different system configuration where hydrogen is available (most likely in the form of sub-surface water-ice) could provide both the fuel and oxidizer necessary for propulsion off the surface of Mars (Sanders, 2010).

[1] From the Design Reference Mission (DRM) 5.0: the max surface stay is 500 days, the max transit duration is 620 days with a margin to 900 days (Drake et al., 2013). This totals to 1400 days for mission duration. An additional 30% is added for hardware margin, totaling 1820 days or approximately 5 years.

Oxygen recovery from CO_2 in spacecraft has already advanced significantly since the days of open-loop life support systems, thanks to the development of the ECLSS currently in operation on board the ISS. However, with the goal of destinations more distant than LEO, i.e. the Moon, Lagrange points, Mars, and asteroids, the mass of nearly every system and consumable (including propellant) increases significantly. Complete recovery of O_2 from CO_2 is already technically possible, but the overall process to convert all CO_2 requires an excess of hydrogen, supplied in the form of water that must be electrolyzed into H_2 and O_2. Spacecraft and habitat ECLSS would benefit from a few possible advancements: 1) increased recovery of O_2 from CO_2 **without** an increase in supplied H_2O, 2) decreased overall system mass by electrolyzing CO_2 and H_2O in the same system to eliminate the need for a separate H_2O electrolysis system. As with all space mission-related systems, such a technology would need to be safe and robust. In addition, for space-transit or in-space destinations where long durations are spent in microgravity, a new CO_2 reduction technology would need to function without issues in the absence of gravity.

There are numerous possible reaction schemes and system configurations where improved O_2 recovery from CO_2 overall system size and mass for both ECLSS and ISRU applications. After describing other CO_2 reduction processes, this research investigates and describes the feasibility of using ionic liquid-mediated electrochemical reduction of CO_2 to generate O_2 in a spacecraft environment.

2.2 Background of Spacecraft CO_2 Reduction Processes

The main physio-chemical processes that have been investigated for spacecraft CO_2 reduction include the Sabatier reaction, the Bosch process, and electrochemical CO_2 reduction (Eckart, 1996; Hodgson, Guirgis, & Converse, 2013; H. W. Jones, 2011; Larson & Pranke, 1999; J. Perry et al., 2014; J. L. Perry, Bagdigian, & Carrasquillo, 2010; Sanders, 2010; Swickrath & Anderson, 2012). The SOA aboard the International Space Station (ISS) is a Sabatier reactor contained within the Carbon dioxide Reduction Assembly (CRA). Carbon dioxide is removed from the ISS atmosphere with the Carbon Dioxide Removal Assembly (CDRA) and it is concentrated and pressurized to be used with the CRA. In the CRA, CO_2 and diatomic hydrogen (H_2) are reacted over a catalyst bed at 150-600^oC to produce methane (CH_4) and water

(Samplatsky, Grohs, Edeen, Crusan, & Burkey, 2011). While the CH_4 is vented to space vacuum, the bulk H_2O is cooled, condensed, purified in the Water Processing Assembly, where it can then be fed to the Oxygen Generation Assembly (OGA). The OGA is a proton exchange membrane (PEM) water electrolyzer that produces H_2 and O_2. The product O_2 is provided to the cabin atmosphere for the crew to breathe and the product H_2 is routed back to the Sabatier reactor to continue reducing CO_2. The Sabatier and water electrolysis reactions are summarized in Equations 1 and 2 and a simple schematic with reactions balanced for the overall process can be seen in Figure 1.

Water Electrolysis	$2H_2O \leftrightarrow 2H_2 + O_2$	$\Delta E_0 = 1.23$ V	(1)
Sabatier Reaction	$CO_2 + 4H_2 \leftrightarrow CH_4 + 2H_2O$	$\Delta H^0rxn = -165$ kJ/mol	(2)

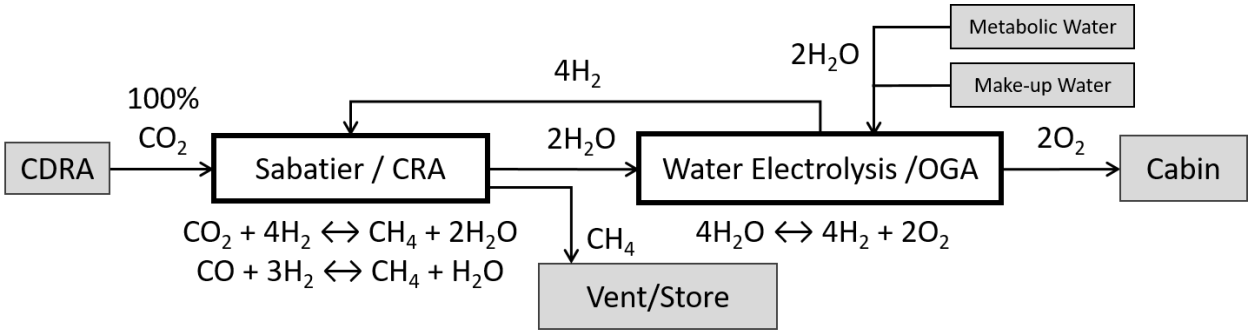

Figure 1. ISS CO_2 Reduction and O_2 Generation System Architecture

Ground testing of this SOA demonstrates recovery of 47−52% of the O_2 from CO_2 (Lange et al., 2018). The theoretical limit from stoichiometry is allows for 50% O_2 recovery from CO_2 due to the loss of H_2 as a reactant in the form of the vented CH_4 (Gatens et al., 2015). However, due to the fact that additional H_2O must be electrolyzed to meet O_2 consumption requirements ("Make-up Water"), there is extra H_2 available to reduce additional CO_2 via the Sabatier reaction. This allows the effective combined theoretical efficiency to be 54% of the O_2 to be recovered from CO_2. Ongoing efforts to improve the efficiency of this system include processing the product methane to generate H_2 that can be fed back to the Sabatier reactor (Abney, Greenwood, et al., 2013; Abney, Miller, & Williams, 2010; Greenwood et al., 2015).

The Bosch process is theoretically capable of recovering 100% of the O_2 from CO_2. The chemical reactions described in Equation 3 (the reverse-water gas-shift (RWGS) reaction), Equation 4 (the CO hydrogenation reaction), and Equation 5 (the Boudouard reaction) each contribute to the Bosch process, the overall reaction shown in Equation 6 (Abney, Mansell, Atkins, Evans, & Nur, 2015). It should be noted that Equations 4 and 5 occur in parallel. Efforts to develop the technical maturity of a Bosch system and address the engineering challenges related to it are ongoing (Abney, Mansell, et al., 2013; Abney & Mansell, 2010; Abney et al., 2015).

RWGS	$CO_2 + H_2 \leftrightarrow H_2O + CO$	$\Delta H^0_{rxn} = 41$ kJ/mol	(3)
CO Hydrogenation	$CO + H_2 \leftrightarrow H_2O + C(s)$	$\Delta H^0_{rxn} = -131$ kJ/mol	(4)
Boudouard	$2CO \leftrightarrow CO_2 + C(s)$	$\Delta H^0_{rxn} = -172$ kJ/mol	(5)
Bosch Process	$CO_2 + 2H_2 \leftrightarrow 2H_2O + C(s)$	$\Delta H^0_{rxn} = -90$ kJ/mol	(6)

Electrochemical CO_2 reduction is another process capable of recovering O_2 from CO_2. While there are many different implementations and possible reaction products, the main desired overall reactions for ECLSS or ISRU purposes are carbon monoxide forming, Equation 7, or methane forming, Equation 8.

Electrochemical CO_2 to CO	$2CO_2 \leftrightarrow 2CO + O_2$	$\Delta E^0 = 1.33$ V	(7)
Electrochemical CO_2 to CH_4	$CO_2 + 2H_2O \leftrightarrow CH_4 + 2O_2$	$\Delta E^0 = 1.06$ V	(8)

The processes described by Equation 7 and 8 alone are capable of a theoretical recovery of O_2 from CO_2 of 50% and 54%, respectively, considering that a system using Equation 8 alone would suffer essentially the same inefficiency suffered by the loss of hydrogen in the form of methane described above by the combination of the ISS CRA and OGA. While it is possible (but difficult) to generate CH_4 from CO_2 electrolysis (Kuhl et al., 2014), the main intent of this work is investigating CO_2 electrolysis to form CO and O_2. The possible benefits from using CO_2 electrolysis to CO and O_2 compared with other chemical reactors are as follows:

1) Equation 7 can proceed without the loss of H_2O, making it H_2-neutral (water-neutral) O_2 recovery

2) Equation 1 and 7 can proceed in a single reactor, producing CO and H_2 via co-electrolysis

3) In solvated CO_2 electrolysis, Equation 7 and 8 can proceed at significantly lower temperatures than any of the other chemical or electrochemical CO_2 reduction reactions

5) Equation 7 could be used with Equations 1 and 2 (as an add-on process) to boost O_2 recovery from CO_2 up to 70%.[2] Similarly, Equation 7 could be used with Equation 8 in separate systems for the same effect.

2.3 Electrochemistry Fundamentals

An electrolysis cell uses electricity to drive a non-spontaneous chemical reduction-oxidation (redox) reaction at two separate electrodes; in contrast to a fuel cell, which uses a spontaneous redox reaction to generate electricity. As the redox reaction proceeds, electrons travel through an external source (or load) and ions travel through the electrolyte to complete an electrical circuit. The standard electrode potential (E^0) is the potential at which a reaction will theoretically occur, as determined by thermodynamics. E^0 is proportional to the change in Gibbs free energy of reaction, as defined in Equation 9. These electrode potentials must be reported with respect to a reference potential to have meaning on a relative scale. E^0 = 0.00 V is thus defined by the standard hydrogen electrode (SHE) for all temperatures. The SHE is a theoretical electrode where hydrogen ions (H^+) are reduced to H_2 (Equation 10) in a solution with unit activity for H^+, i.e. pH = 0.

$$\Delta G^0 = -nFE^0 \tag{9}$$

$$2H^+ + 2e^- = H_2 \qquad E^0 \equiv 0.00\ V \tag{10}$$

where ΔG^0 is the change in Gibbs free energy, n is the number of moles of products, F is Faraday's constant (96,485 C mol^{-1}) and E^0 is the standard electrode potential.

[2] The process combination described by Equations 1 and 2 combined are water (or hydrogen) limited. This leaves an excess of metabolic CO_2 available for alternate processing. If the remaining CO_2 is reacted via Equation 7 with no loss of water or hydrogen, then 50% O_2 recovery from the remaining CO_2 (Equation 18), combined with the original 54% O_2 recovery from CO_2 (Equation 1 and 2) would create a combined system that could theoretically recover 70% of the O_2 available from CO_2.

A common metric used to evaluate energy efficiency of a reaction is the overpotential of the reaction. **Overpotential** (η) is defined as the potential difference between the thermodynamically derived equilibrium potential (E_{eq}) and the experimentally observed potential (E) for a reaction to proceed with a non-zero current, as seen in Equation 11. The difference between E_{eq} and E^0 can be understood from the Nernst equation (Equation 12), where E_{eq} accounts for a departure from standard conditions (i.e. unit activity for each species), but where the net current remains zero.

Overpotential $$\eta = \left|E - E_{eq}\right| \quad (11)$$

Nernst Equation $$E_{eq} = E^0 - \frac{R_{gas}T}{zF}\ln K \quad (12)$$

where R_{gas} is the universal gas constant, T is the temperature, z is the number of electrons transferred, F is Faraday's constant (96,485 C mol^{-1}), K is the ratio of activity of the products over the reactants (or more practically, concentration instead of activity).

Current density (j_T) is useful as a descriptor for the rate of reaction for a given reactor size, but is generally determined experimentally at a small scale by a measure of the total current divided by total working electrode area, as seen in Equation 13.

Current Density $$j_T = \frac{i_T}{A_{WE}} \quad (13)$$

where i_T (A) is the total current at a given time and A_{WE} (cm^2) is the area of the working electrode.

Overpotential should always be reported with current density for a meaningful description of either. Due to Ohm's law ($V = iR$), an increase in voltage will lead to a proportional increase in current, but an efficient and effective process would show a large increase in current for a small increase in voltage (i.e. low resistance).

Faradaic efficiency (FE_k) is the measure that describes the selectivity of the electrochemical system for a particular product, k. It can be experimentally determined by tracking the amount of charge passed in

a given period of time and the number of moles of product generated in that time period, finally calculated by Equation 14. FE_k not only describes the product selectivity of the reaction, but also provides information on how much current was used in driving the desired reaction(s) (Faradaic processes) and how much current was "lost" to ohmic behavior (electrical resistance or non-Faradaic processes). Analytical techniques for quantifying the number of moles of product generated will depend on the expected phase of the products. For this study, NDIR spectroscopy and mass spectrometry are used to analyze gas phase products.

Faradaic Efficiency $$FE_k = \frac{zn_kF}{Q_T} \quad (14)$$

where z is the number of electrons transferred for the formation of product k from the original reactant, n_k is the number of moles of product k (mol), F is Faraday's constant (96,485 C mol^{-1}), and Q_T (C) is the charge passed in the duration of the process.

With these three metrics (η, j_T, and FE_k), an electrochemical cell's overall **energy efficiency** (ε_{energy}) and **process effectiveness** ($\varepsilon_{process}$) can be defined as Equations 15 and 16, respectively. Additionally, an estimate of the reactor size and number of cells can be given based on the $\varepsilon_{process}$.

Energy Efficiency $$\varepsilon_{energy} = \sum \frac{E_{k,eq}FE_k}{E_{k,eq} + \eta_k} \quad (15)$$

Process Effectiveness $$\varepsilon_{process,k} = j_T FE_k \quad (16)$$

where $E_{k\text{-}eq}$ is the equilibrium potential for a certain product k. Process effectiveness is generally referred to as the Faradaic current and can be thought of as the rate at which a desired product is produced per unit area of electrode surface. ε_{energy} is defined on a 0 to 100% scale and $\varepsilon_{process}$ is defined on a scale of units A/cm^2 and can only be compared with a desired process effectiveness, i.e. a product-specific process rate or reactor size requirement. $\varepsilon_{process}$ is typically referred to as Faradaic current density, but the wording is changed here to highlight its importance in determining feasibility of a system using an electrochemical process.

2.4 Electrolysis of CO_2

Electrochemical CO_2 reduction (synonymous with CO_2 electrolysis) has been an active area of research for decades (Hori, Kikuchi, & Suzuki, 1985) and the pathways for implementing CO_2 electrolysis can be generally categorized by the phase and temperature of the reaction (Spinner, Vega, & Mustain, 2012). High temperature (>750°C), gaseous CO_2 electrolysis is the focus of solid oxide electrolysis (SOE) cells; whereas solvated CO_2 electrolysis is possible at low temperatures (<100°C) and ambient pressures using liquid electrolytes and solvents. Solvated CO_2 electrolysis can further be categorized by means of catalysis (homogeneous vs. heterogeneous) and solvent (aqueous vs. non-aqueous), as seen in Figure 2.

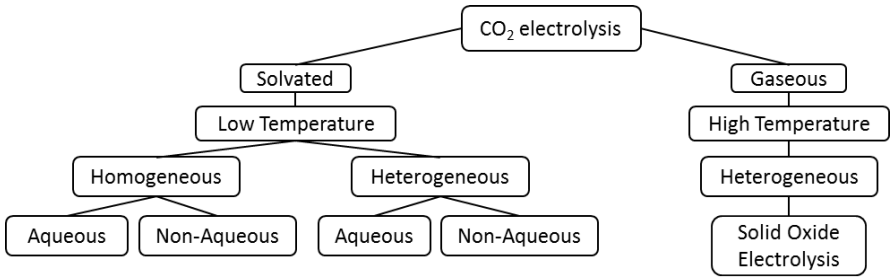

Figure 2. Categorization of CO_2 electrolysis

2.4.1 Solid Oxide Electrolysis

Solid oxide electrolysis for CO_2 reduction has previously been proposed for spacecraft ECLSS and ISRU (Ebbesen, Knibbe, & Mogensen, 2012; Isenberg, 1989; M. G. McKellar, Wood, & Stoots, 2011; Shumar, See, Schubert, & Powell, 1976; Sridhar & Vaniman, 1997), owing to its higher reaction rates, lack of a liquid phase, and narrow product distribution (i.e. product selectivity for CO and O_2) (Zhan & Zhao, 2010). An SOE cell reduces CO_2 at a metal or non-metal electrode to CO and O^{2-} and oxidizes O^{2-} to O_2 at the anode. The O^{2-} is conducted through the solid electrolyte consisting of a ceramic material, usually yttria-stabilized zirconia (YSZ), held at temperatures between 750 and 1000°C to enable ion conduction. It is also possible to co-electrolyze CO_2 and H_2O (steam) to CO and H_2 in a SOE reactor, although recent studies indicate that hydrogen evolution is the predominant cathodic reaction and CO is produced via the RWGS reaction, rather than true electrochemical reduction (M. McKellar et al., 2010; Zhan & Zhao, 2010).

The high temperatures of SOE reactors add to the thermodynamic favorability of both CO_2 and steam electrolysis, as well as increasing reaction rates. However, such high temperatures call for thorough insulation or heat maintenance, and can also lead to issues involving electrode and catalyst deactivation via sintering and coke agglomeration (Graves, 2010a; Moçoteguy & Brisse, 2013). Fragility of the ceramic materials in these reactors has been a concern in the past, as well as difficulty in making durable seals to the ceramic materials, particularly with thermal cycling (Isenberg, 1989). Recent development projects include investigating SOE co-electrolysis reactor integration with a Sabatier reactor, improvements to some aforementioned issues (Iacomini, 2011; Moçoteguy & Brisse, 2013), implementation of a SOE co-electrolysis within a regenerative fuel cell system (Iacomini, Benjamin, & Milobar, 2015), and improving long term durability of SOE cells (Zhang et al., 2013). For clarity, all remaining sections will discuss CO_2 electrolysis only from the standpoint of considering solvated CO_2 electrolysis, not SOE cells.

2.4.2 Solvated CO_2 Electrolysis

Catalyzing solvated electrochemical CO_2 reduction has been a major research interest, with the prospects being possible hydrocarbon fuels or synthesis gas (CO and H_2 mixture) production at low energy costs. Heterogeneous catalysis of aqueous CO_2 reduction with a full product analysis was first reported by Hori et al. (1985), showing favorable CO production on Ag and Au electrodes, and CH_4 production on Cu electrodes (Hori et al., 1985). Thereafter, metal and alloyed electrodes have been the subject of major study for heterogeneous catalysis, due to their high conductivity and ability to form a wide range of products from CO_2 reduction (Hori, 2008; Hori, Wakebe, Tsukamoto, & Koga, 1994; Kumar et al., 2016). The wide range of possible products, including hydrogen in aqueous solvents, however, has kept them from being a solution to industrial CO_2 electrolysis, where 100% product selectivity is desired.

Homogeneous electrochemical CO_2 reduction catalysts are typically transition metal complexes, and compared with heterogeneous catalysts, generally show very high selectivity for CO and O_2. The challenges with homogeneous catalysts have been in improving reaction rates and preventing catalyst decomposition, as well as attempting to attain more reduced species than CO from CO_2 (Matsubara, Grills, & Kuwahara,

2015). Recent reviews by (Costentin, Robert, & Savéant, 2013) and (M. R. Dubois & Dubois, 2009) describe progress in homogeneous catalysis for electrochemical CO_2 reduction. As for heterogeneous catalysis of electrochemical CO_2 reduction, significant work in improving reaction rates (current density) while maintaining product selectivity has been underway, particularly investigating nanostructured catalysts such as nanoparticle coatings and metal organic frameworks for electrodes (Kang et al., 2015; Qiao, Liu, Hong, & Zhang, 2014). Rigorous methods for catalyst comparison have been recently presented in order to homogenize the reporting of experimental data and reactor conditions (Costentin, Drouet, Robert, & Savéant, 2012). To see trends and comparisons between historical and current electrochemical CO_2 reduction efforts, a report on recent advances has been compiled by (J. P. Jones, Prakash, & Olah, 2014). Selected data from these studies are presented later in this paper for the reader's reference.

Aqueous CO_2 electrolysis is attractive because the presence of water allows proton-coupled electron transfer reaction pathways to occur, which require significantly less energy input than the direct, one electron reduction of CO_2 (Matsubara et al., 2015). A list of electrochemical CO_2 reduction half reactions is presented in Table 1, along with the oxidation evolution reaction (OER) and hydrogen evolution reaction (HER) that are especially relevant when water is present within an electrochemical cell. While aqueous CO_2 electrolysis benefits from high ion conductivity and low viscosity, it suffers from low CO_2 solubility and the competition of the HER with CO_2 reduction at the cathode. The low CO_2 solubility limits mass transport of reactant to the electrode surface, ultimately limiting reaction rate. And unless co-electrolysis of both CO_2 and H_2O is desired for the application (e.g. commercial syngas production and some applications discussed later in this dissertation), HER is generally seen as detrimental to cell performance where 100% product selectivity for a particular reduced form of CO_2 is desired for ease of downstream processing.

Table 1. Relevant Electrochemical Half Reactions (Matsubara et al., 2015)

Reactions	E_{eq} vs. SHE
$CO_{2(aq)} + e^- \leftrightarrow CO_2^{\bullet -}{}_{(aq)}$	– 1.90 V
$CO_{2(g)} + 2H^+_{(aq)} + 2e^- \leftrightarrow HCO_2H_{(aq)}$	– 0.61 V
$CO_{2(g)} + 2H^+_{(aq)} + 2e^- \leftrightarrow CO_{(g)} + H_2O_{(l)}$	– 0.52 V
$CO_{2(g)} + 4H^+_{(aq)} + 4e^- \leftrightarrow H_2C(OH)_{2(aq)} + H_2O_{(l)}$	– 0.49 V
$CO_{2(g)} + 6H^+_{(aq)} + 6e^- \leftrightarrow CH_3OH_{(aq)} + H_2O_{(l)}$	– 0.38 V
$CO_{2(g)} + 8H^+_{(aq)} + 8e^- \leftrightarrow CH_{4(aq)} + 2H_2O_{(l)}$	– 0.24 V
$2H^+_{(aq)} + 2e^- \leftrightarrow H_{2(g)}$	– 0.41 V
$H_2O_{(l)} \leftrightarrow 2H^+_{(aq)} + 2e^- + ½O_{2(g)}$	+ 0.81 V

Conditions: pH = 7, T = 25 °C, 1 atm of gases (g), 1 M solutes (aq), in water as solvent (l)

Non-aqueous CO_2 electrolysis has been studied as a means to alleviate some of the issues associated with aqueous CO_2 electrolysis. Organic solvents, such as acetonitrile, propylene carbonate, and methanol have higher CO_2 solubility (especially at higher pressures) and lower proton availability, leading one to expect faster reaction rates and improved product selectivity compared with aqueous CO_2 electrolysis (Grills et al., 2014; Medina-Ramos, DiMeglio, & Rosenthal, 2014). While HER is suppressed with the use of non-aqueous solvents at various electrode materials, reaction products favor CO, but remain largely diverse, including oxalic acid, carboxylic acid, and formic acid, among others (Hori, 2008). The generally volatile nature, environmental hazards, and toxicity of conventional non-aqueous solvents make them unattractive for spaceflight applications. In addition, if electrolysis products include hydrogen, then the solvent itself may contribute as the proton donor, necessitating another proton source (e.g. water or more solvent) for continuous reactor operation to avoid proton depletion.

It is clear that challenges exist in identifying catalyst materials and developing electrochemical cell designs that lower the energy requirement, improve product selectivity, and generate products at a sufficient rate with sufficient performance stability over time. Recent advancements in ionic liquids materials research and the understanding of their interactions in CO_2 reduction electrochemistry introduce the possibility of creating efficient cells using ILs as catalysts (or promoters), solvents, and electrolytes.

2.4.3 Ionic Liquids in CO_2 Electrolysis

Ionic liquids (ILs) are a class of materials that are similar inasmuch as they are salts that are liquid and ionically conductive at ambient temperatures. They generally consist of a large organic cation with low symmetry, and an anion that is either organic or inorganic with a diffuse or protected negative charge (Clare, Sirwardana, & MacFarlane, 2009). ILs exhibit favorable solubility and solvability with many compounds, practically negligible vapor pressure, and both thermal and electrochemical stability. Their main drawback is their moderate-to-high viscosity (pure ILs are generally 1-2 orders of magnitude more viscous than water in units of mPa-s, or cP)

The liquid state of an ionic liquid is thermodynamically favorable at low temperatures due to the large size and conformational flexibility of the constituent ions, which lead to small lattice enthalpies and large entropy changes that favor melting (Krossing et al., 2006). Despite the liquid state, some ordered structure of the ions remains after melting, likely contributing to the extremely low vapor pressure of ionic liquids (Daily, 2008). This ordered structure could also be a contributor to the viscosity of ILs. Common ILs include both cyclic (imidazolium, pyrrolidinium, pyridinium, etc.) and non-cyclic (quaternary phosphonium and ammonium) cations, and fluorinated anions (BF_4^-, PF_6^-, $CF_3SO_3^-$, and $(CF_3SO_2)_2N^-$). The structure of some of these cations and anions can be seen in Table 2, along with common abbreviations. Interestingly, these types of cations and anions are also the ones most commonly used in electrochemical CO_2 reduction studies to date, highlighting the narrow scope of research into IL-assisted CO_2 reduction. For a history of the development of ionic liquids to their widely popular forms today, the reader is directed to a review by (Angell, Ansari, & Zhao, 2012).

Table 2. Names, Abbreviations, and Structures of common IL cations and anions (all structures generated at chemspider.com)

Cations	1-butyl-3-methylpyridinium [bmpy] 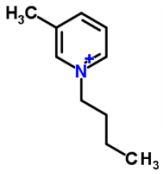	1-butyl-1-methylpyrrolidinium [bmpyrr] 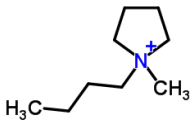	1-ethyl-3-methylimidazolium [emim] 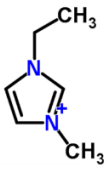	N,N,N,N-trimethylbutylammonium [N_{4111}] 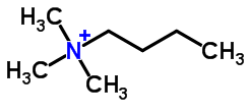
Anions	Hexafluorophosphate [PF_6] 	Tetrafluoroborate [BF_4] 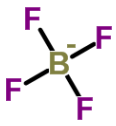	Trifluoromethanesulfonate [OTf] 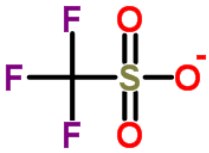	Bis(trifluoromethylsulfonyl)-imide [Tf_2N] 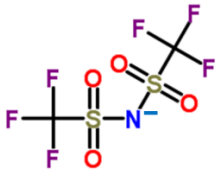

Many ILs have a number of possible favorable properties depending on variation of the ion structures including: non-volatility, electrochemical stability, thermal stability, chemical stability, stability in air and water, relatively high ion conductivity, moderate viscosity, high polarity, flame resistance, favorable solubility with many compounds, and designability (Armand, Endres, MacFarlane, Ohno, & Scrosati, 2009; Holbrey & Seddon, 1999). The wide applicability of materials with these properties has led to an exponential increase in the number of research articles published on ionic liquids in the past two decades (L. E. Barrosse-Antle et al., 2010). As they relate to CO_2 reduction electrochemistry, ILs are inherently attractive as solvents and electrolytes that are safer and more stable than many traditional solvents and electrolytes (Ohno, 2005). A variety of properties and transformations of CO_2 in ILs (mainly synthetic chemistry) are described thoroughly in a review by (Jutz, Andanson, & Baiker, 2011), and a concise tabulation of electrochemical CO_2 reduction studies in ILs is presented by (Alvarez-Guerra, Albo, Alvarez-Guerra, & Irabien, 2015).

A highly visible study presented by (B. A. Rosen et al., 2011) revealed a catalytic effect from the presence of an IL for CO_2 electrochemical reduction. CO_2 was reduced on a silver electrode in water with

18mol% [emim][BF_4], producing CO with >96% selectivity (Faradaic efficiency) and less than 0.2 V of overpotential (thermodynamically efficient), but at low rates, c.a. 0.25 mA/cm^2. This spurred a handful of research groups to further investigate a number of electrode-IL combinations for their effect on the CO_2 reduction reaction mechanism and performance enhancement (Mohammad Asadi et al., 2014; Medina-Ramos, Pupillo, Keane, Dimeglio, & Rosenthal, 2015; Brian A Rosen et al., 2013; Sun, Ramesha, Kamat, & Brennecke, 2014; Tanner, Batchelor-McAuley, & Compton, 2016), most of which are present in a compilation review by (Alvarez-Guerra et al., 2015). ILs have also been seen to enhance the catalytic activity of homogeneous CO_2 reduction catalysts, such as *fac*-ReCl(bpy)$(CO)_3$, in both the rate constant and overpotential (Grills et al., 2014; Matsubara et al., 2015).

Through most of these studies, the ILs employed have been from the imidazolium, quaternary ammonium, or quaternary phosphonium cation families, and had an anion with physical solubility for CO_2 and a high fluorine atom count. The viscosity and ionic conductivity of the ammonium and phosphonium-based ILs appear to be prohibitive to their use in a practical electrochemical system. Imidazolium and pyrrolidinium cation which, compared to the commonly used anions, have been found to be the main contributors to the observed catalytic effects for CO_2 reduction (Tanner et al., 2016; Zhao, Horne, Bond, & Zhang, 2016).

The anions of the ILs have received much more attention in the design of new ILs due to observations that show they have the largest contributions to IL CO_2 solubility and viscosity, and due to the fact that there is broader interest in CO_2 capture (J. L. Anderson, Dixon, & Brennecke, 2007). Where solubility of CO_2 in water is $6.22x10^{-4}$ mole fraction (25°C, 101.325 kPa, 100% CO_2) (Carroll, Slupsky, & Mather, 1991), it can be as high as $3.08x10^{-2}$ mole fraction (25°C, 100 kPa, 100% CO_2) in a common IL (e.g. [bmim][Tf_2N]) (Anthony, Anderson, Maginn, & Brennecke, 2005), and c.a. 0.8 mole fraction (22°C, 100 kPa, 100% CO_2) in a tailor-made IL (e.g. [emim][2-CNPyr]) that exhibits chemical complexation with the CO_2 (Seo et al., 2014). Carbon dioxide solubility at low partial pressures remains more favorable in IL systems than in water and some other solvents, allowing the possibility that an IL as solvent in an

electrochemical system can provide sufficient reactant at lower CO_2 concentrations to support CO_2 reduction (Hanioka et al., 2008).

The difference between ILs such as [bmim][Tf_2N] and [emim][2-CNPyr] is that the [Tf_2N] anion adsorbs CO_2 physically, whereas the [2-CNPyr] adsorbs CO_2 by forming a chemical complex. There are a significant number of anions that belong to both categories, but the understanding for how adsorption mechanism affects CO_2 electrolysis performance is still largely unexplored. After a thorough search, it appears that only one chemically adsorbing anion, acetate (i.e. in [bmim][acetate]), has been tested with solvated CO_2 and an applied electrochemical potential: it appeared that CO_2 sorption in this IL was not easily reversed, suggesting that some anions may bind CO_2 too strongly for reversible CO_2 capture or reduction , and there was no mention of gaseous electrochemical products (Laura E Barrosse-Antle & Compton, 2009). For ILs with physical solubility for CO_2, the reaction products can change between differences in anion, cation, and electrode material, among other factors (Alvarez-Guerra et al., 2015). A more complete discussion on possible reaction mechanisms and design of ILs for electrochemical CO_2 reduction, which ultimately leads to a selection of ILs to investigate in this work is presented in Chapter 4.

With all of this in mind, solvated CO_2 electrolysis processes are essentially absent from space exploration ECLSS and ISRU literature, largely owing to the low technology readiness level (TRL) from lack of development of such systems (Muscatello & Santiago-Maldonado, 2012; NASA, 2018; Sanders et al., 2015). There has, however, been significant development in this field within the renewable and carbon-neutral energy communities that are primarily interested in large-scale fuel production. The requirements on energy efficiency, production rate, product selectivity, and capital cost for these other research interests show that CO_2 electrolysis is not yet at an effective level of technical maturity for practical implementation (H. R. M. Jhong, Ma, & Kenis, 2013; Kondratenko et al., 2013). In the related commercial applications, these performance metrics are tied to their associated capital and operational costs. For example, platinum, iridium, and ruthenium are some of the best materials for the anode of CO_2 electrolyzers, but the high up-front cost of the materials make them cost-prohibitive if the product formation rate per electrolyzer size is

low (i.e. if a lot of platinum, etc. is required). While the dollar value of a system is still important in space applications, its mass, volume, and energy efficiency are much higher weighted cost metrics due to the weight, size, and power restrictions imposed ultimately by expensive launch costs. Second-order considerations are also important for space missions, i.e. if the product gases from a process are not pure or are mixed with liquids, then an additional gas purification or gas-liquid separation step may be necessary, implicitly increasing the mass, power, and volume associated with a CO_2 electrolysis reactor. However, drivers for space exploration implementation can vary significantly from commercial industrial requirements, and as such, these technologies may be closer to feasibility for ECLSS and ISRU applications than for terrestrial purposes. As such, even if a technology is not yet commercially viable, it may still prove feasible for space exploration applications if the more stringent technical requirements are met. Based on current literature and experimental work from this study, it is estimated that IL-based CO_2 electrolysis for space exploration applications is approximately at TRL 3 (NASA, 2018).

2.5 Related Presentations and Publications:

Holquist, J. B., Klaus, D. M., Nabity, J. A., and Abney, M. A. (2016). Electrochemical Carbon Dioxide Reduction with Room Temperature Ionic Liquids for Space Exploration Missions, ICES-2016-314, pp. 1–19.

Electrochemical Carbon Dioxide Reduction with Room Temperature Ionic Liquids for Space Exploration Missions. *46th International Conference on Environmental Systems* (ICES), Vienna Austria, July 2016 (presentation)

Chapter 3 – CO_2 Electrolysis for Space Exploration

3.1 Introduction to Flow Cell Electrolyzers

An electrochemical CO_2 reduction system assisted by ILs has a number of possible designs depending on the environment in which it is employed and the supporting systems with which it can be designed to function. In general, to produce O_2 at a sufficient rate in a continuous reactor, it will be necessary to have a stack of flowing electrolyte electrochemical cells with cathode and anode compartments separated by ion permeable membranes that prevent gaseous product crossover and isolate anolyte from catholyte. To further clarify the concept in this context, the aqueous, heterogeneous electrolysis of CO_2 requires the solvation of CO_2 into an aqueous IL solution, which would be pumped into the cathode compartment of a proton exchange membrane (PEM)-separated electrolysis cell where the CO_2 would be electrochemically reduced at the cathode and converted to reduced products, such as CO or CH_4 (the following generic examples are presented with CO as the main reduction product for simplicity and relation to most later-discussed applications). On the anode compartment side of the electrolyzer, water would be oxidized to O_2 and protons, which travel across the cell to assist in reducing the CO_2 at the cathode, in turn creating water as a byproduct with the reclaimed oxygen atom from CO_2.

A layout of a generic single cell in this representation can be seen in Figure 3, which assumes that CO_2 is solvated in the IL/H_2O mixture prior to being introduced to the cathode compartment, and that product separation occurs outside of the cell. While its simplicity is attractive, one of the major issues with this type of cell is mass transport limitations imposed by requiring CO_2 to be in a solvated phase. In a traditional recirculating electrolyte electrolyzer like this, CO_2 is only introduced to the cathode in solution. This configuration inherently limits the reaction rate based on the bulk solubility of CO_2 in the catholyte, governed by Equation 17, and is affected by mass transport limitations (Najafabadi, 2013).

$$i_L = nFK_mC_b \tag{17}$$

where, i_L is the limiting current density (mA/cm^2), n is the electron stoichiometry coefficient for the reaction (n=2 for CO_2→CO and 8 for CO_2→CH_4), F is Faraday's constant = 96,485 C/mol, K_m is the mass transfer coefficient (K_m = 1x10^{-5} m/s for CO_2 in water), and C_b is the bulk concentration of the reactant species (C_b = 0.03 kmol/m^3 in water). For electrochemical CO_2 reduction in CO_2-saturated water, the limiting current density is thus calculated as i_L = 6 mA/cm^2, where the area is the electrochemically active surface area. The transport limitation is governed by the diffusion layer thickness between the catalyst and the bulk solution and the diffusion rate of CO_2 in the solution. These types of electrolyzers also require a down-stream gas-liquid separation process. In addition, if micro- or nano-structured cathode materials are used (which often exhibit the most favorable performance metrics, (M. Asadi et al., 2016)), reduced CO_2 products can remain in the pores, inhibiting accessibility of reactants to the catalyst surface and degrading the performance of the electrolyzer over time.

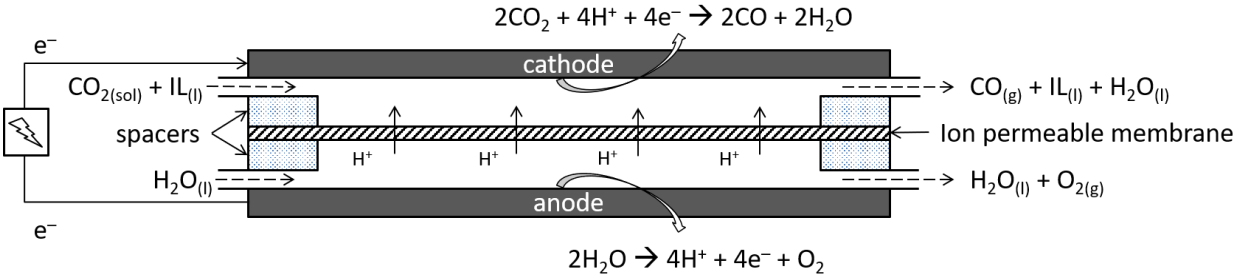

Figure 3. Generic, single flow cell for CO_2 electrolysis with ILs (ex: 100% CO production)

Contrary to the cell shown in Figure 3, a generic layout of a cell with gas diffusion electrodes (GDEs) is shown below in Figure 4. GDEs in this configuration allow gas contact with the liquid and electrode within the pores or on the liquid-solid interface of the electrode, possibly eliminating the need for upstream CO_2 concentration or contactors (though to meet necessary production rates in small reactors, this may not be feasible). Introduction of gas phase CO_2 immediately adjacent to the catalyst and electrolyte inherently improves the mass transport restrictions imposed by low solvated CO_2 mobility in solution without needing to increase the temperature or pressure of the reactor, which introduces other design concerns.

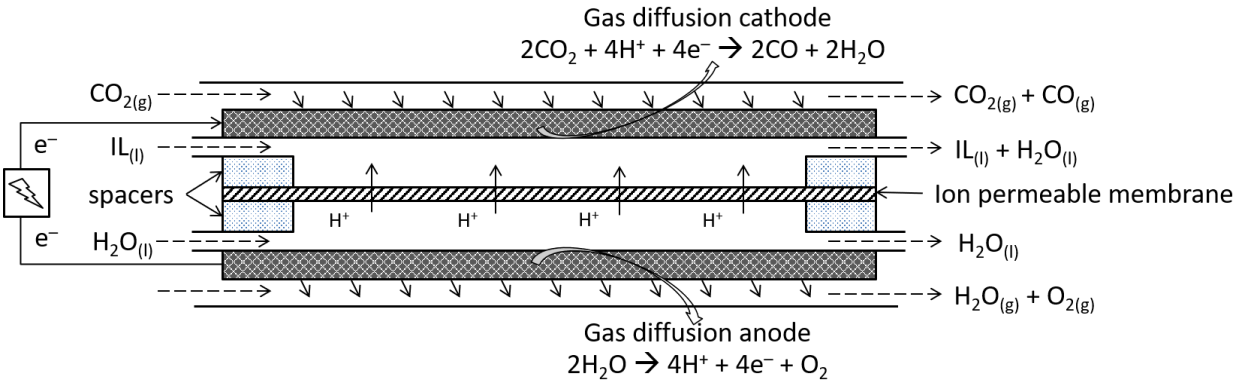

Figure 4. Generic, single flow cell for CO_2 electrolysis with ILs and GDEs

The schematics shown in Figure 3 and Figure 4 represent the two most prevalent forms of flow cell electrolyzers for CO_2 electrolysis present in literature (Weekes, Salvatore, Reyes, Huang, & Berlinguette, 2018). These designs have inherent issues related to space applications, namely gas-liquid separation, two-phase fluid handling, concentration of the CO_2 in either the gas or solvated phase, and purifying the product gases, with the former three issues being of particular importance in a microgravity environment. While the system-level implications of these issues are considered for each application presented in this chapter, a more thorough discussion of component level issues in a practical electrolyzer is presented in Chapter 6, along with the design, development, and testing of a prototype electrolyzer that may alleviate implementation concerns.

3.2 Applications of Electrochemical CO_2 Reduction Systems

The two factors that will have the most significant effects on the design and integration of an Electrochemical CO_2 Reduction System (ECRS) are the availability of CO_2 and the level of gravity in the operational environment of the mission in which it is employed. Possible near-term future mission destinations can be described by these two factors: 1) the surface of Mars (quasi-unlimited source of CO_2, 3/8 Earth gravity), 2) the surface of Earth's Moon (CO_2 supply limited to metabolic production, 1/6 Earth gravity), and 3) an asteroid, a small moon, in-orbit, or in-transit (CO_2 supply limited to metabolic production, ~0 gravity). In the non-Mars-surface cases, CO_2 reduction would be used entirely for

regenerable ECLSS, but on the surface of Mars it can facilitate both an ECLSS O_2 recovery and ISRU-facilitated O_2 production (and CH_4 production, with a supply of ISRU water).

Conceptual designs of system architectures that use an ECRS with ILs are presented in detail below in Applications 1–7, categorized by environment, desired reaction, and the supporting systems the design includes. Each Application's overall qualities are summarized in Table 3. In general, Applications 1 and 2 are envisioned for scenarios on the surface of Mars, and Applications 3 – 7 are more relevant (though not exclusively) to destinations without a source of CO_2 other than metabolically produced CO_2. In terms of gravity field effects at the destination of the mission scenario, the major concern will be *how* the ECRS is designed to manage gas-liquid contacting, fluid mixing and two-phase flow, and gas-liquid separation. Clearly, if there is gravity present, reactor designs similar to those used on Earth can be used, but care must be taken due to the increased influence that fluid surface tension and resulting capillary forces will have in a reactor over gravity-driven buoyancy and convection. While not the primary subject of this dissertation, electrolysis of CO_2 to CH_4 is included as an extension of the analysis due to commonality of the considerations necessary for CH_4 production with CO production.

Table 3. Applications of an ECRS that uses ILs with supporting resources and systems, with qualitative advantages and challenges summarized

CO_2 Electrolysis Processes	Application number	used with Martian CO_2 atmosphere	used with Sabatier reactor	used with Water electrolysis	used before/with 2nd stage Bosch	used with upstream CO_2 capture	Advantages	Challenges
$CO_2 \rightarrow CO + (1/2)O_2$	1	√			~	~	Indefinite O_2 production on Mars (ISRU)	Dust, CO_2 contactor, H_2O volatility
$CO_2 + 2H_2O \rightarrow CH_4 + 2O_2$	2	√				~	Low temp. CH_4 and O2 production (ISRU/propellant)	H_2O source, volatility, dust, propellant containment
$CO_2 \rightarrow CO + (1/2)O_2$	3		√	√		√	~70% O_2 from CO_2, add-on to SOA, possible for ISS payload	Large total system mass, integration with SOA
$CO_2 + H_2O \rightarrow CO + H_2 + (3/2)O_2$	4		√			√	~70% O_2 from CO_2, lower system mass than SOA	Product ratio tuning and variation based on need
$CO_2 + H_2O \rightarrow CO + H_2 + (3/2)O_2$	5				√	~	100% O_2 recovery, replace RWGS with low temp. reactor	Product ratio tuning and variation based on need
$CO_2 + H_2O \rightarrow CO + H_2 + (3/2)O_2$	6				~		No extra CO_2 capture system mass, no solid adsorbers	Balance CO_2 removal and O_2 production rates
$CO_2 + H_2O \rightarrow CO + H_2 + (3/2)O_2$ $CO_2 + 2H_2O \rightarrow CH_4 + 2O_2$	7					~	~70% O_2 from CO_2, single system (lower mass)	Product ratio tuning, single point failure

√ = the above statement is true for this application; ~ = the above statement could or could not be true, depending on reactor configuration, see Figures 2 and 3; "blank" = the above statement is not true for this application

3.2.1 Application 1 – Mars ISRU & ECLSS for all O_2 provisions

With an essentially infinite supply of CO_2 in the atmosphere, a hydrogen-neutral CO_2 reduction system could generate the metabolically required O_2 for an entire crew for any duration of a surface stay on Mars. This application would be best served by an ECRS used to selectively produce CO and O_2 (Equation 7, $CO_2 \rightarrow CO + ½O_2$), and suppress the hydrogen evolution reaction (HER) (Equation 2, $2H^+ + 2e^- \rightarrow H_2$). Electrochemical CO_2 reduction cells with aqueous/IL mixtures have been shown to selectively produce CO over H_2 at a silver electrode, despite significant water content (Brian A Rosen et al., 2013). The difficulties of implementing this type of system would be in preventing dust contamination while allowing for gas contact between CO_2 and the liquid solvent; separating product CO from water vapor; and ensuring H_2O does not escape to the atmosphere. The Martian atmosphere, while rich with CO_2 (~96%), is significantly less dense than Earth's atmosphere. It may be necessary to pressurize the concentrated CO_2 before it is introduced to an ECRS to ensure saturation of the electrolyte with CO_2. Dust could also be filtered from

the gas during the pressurization step, possibly eliminating it as a concern within an ECRS. However, with some ILs having high affinity for CO_2 even at low partial pressures, it may be possible to concentrate dilute CO_2 in the IL solution itself, thereby only necessitating filtration of the dilute CO_2 before introducing it to the IL. In order to meet metabolic O_2 provisions, this conceptual system would need to electrolyze 51 moles CO_2/CM-d.

3.2.2 Application 2 – Mars ISRU for CH_4 propellant and metabolic O_2 requirements

Similarly, Application 2 also utilizes Mars' nearly infinite supply of CO_2. If propellant production is a primary goal of the system, an electrochemical CO_2 reduction system could be used to produce both CH_4 and O_2 by means of Equation 8 ($CO_2 + 2H_2O \rightarrow CH_4 + 2O_2$), given a supply of water. CH_4 is a much more difficult product to selectively produce than CO, given that it requires an 8-electron reduction. Such a system should be sized larger (or faster rates would be preferred if kinetics and mass transport allow) based on the amount of propellant required; the design in Application 1 would be more preferable if intending to size only for metabolic O_2 requirements.

As long as metabolic O_2 requirements are met by a methane producing ECRS, then any excess O_2 and all of the CH_4 would be considered propellant. Even a slightly oversized ECRS compared to one sized to meet metabolic O_2 rates could meet propellant production requirements if sufficient time is allowed and sufficient water is available as reactant (water availability may actually be the greatest challenge for this process). However, using the assumptions of a 500 day maximum surface stay (Drake, Hoffman, & Watts, 2013), propellant production only performed during surface stay, and 6570 kg of CH_4 required for an ascent vehicle (Sanders et al., 2015), one can see that either more time or a much larger reactor is required. Using the data available in Table 4, 12.8 moles CH_4/CM-d at a 4 CM-rate and over 500 days only produces 25,500 moles of CH_4 or 408 kg of CH_4. Therefore, at a given current density, a propellant production plant would need to have 16 times the electrode area as that necessary for metabolic O_2 requirements. Increasing the electrode area by this much would account for O_2 required as oxidizer (22,900 kg) in addition to that

required metabolically (Sanders et al., 2015). Balance of plant considerations would likely increase in mass and size as well, but not necessarily at a 1:1 ratio with electrode surface area. Similar implementation difficulties exist between designs for Applications 1 and 2, but Application 2 will additionally require the separated concentration, pressurization, and storage of both CH_4 and O_2.

3.2.3 Application 3 – ECRS in support of SOA ISS CO_2 reduction and O_2 generation

As stated in the introduction and background, the SOA on board the ISS is theoretically capable of recovering 54% of the O_2 from CO_2 and actually recovers less than 47–52% in practice. In this scenario, more than half of the metabolically available CO_2 is left unreacted. If an ECRS is added to the ISS SOA to process all of the remaining CO_2 via Equation 7 ($2CO_2 \rightarrow 2CO + O_2$) without the loss of hydrogen to methane, such as in the architecture diagram shown in Figure 5, it would appear that the stoichiometric O_2 recovery efficiency from CO_2 would reach roughly 75% (~50% O_2 from Sabatier & OGA working together, then the other half of the metabolic CO_2 processed in Equation 7 with CO_2:O_2 = 2:1, resulting in an additional 25% O_2 recovery). However, this CO_2 distribution scheme would produce O_2 in excess of crew metabolic needs.

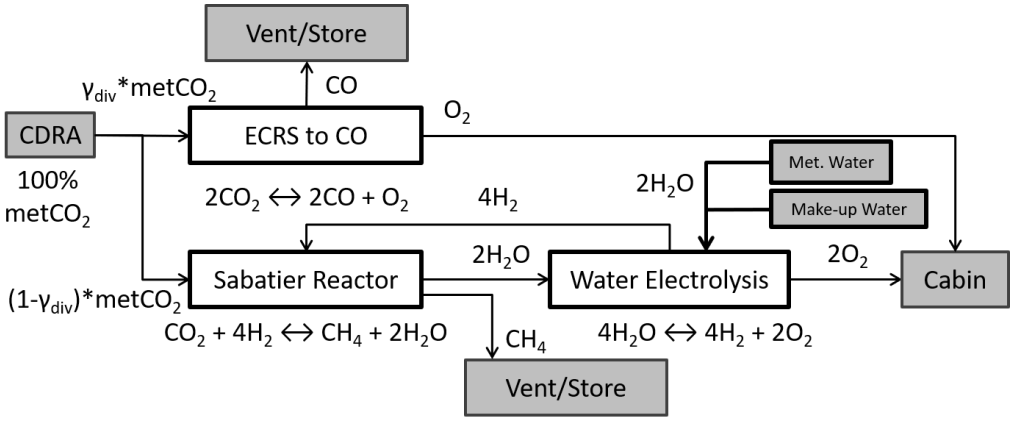

Figure 5. Block diagram of material interfaces and systems comprising Application 3

Since the end goal of O_2 recovery from CO_2 is to reduce the amount of initially supplied consumable mass, it would be best to completely process all metabolically generated CO_2 and in turn, reduce the amount of water necessary for electrolysis. Yet, by electrolyzing less water, the Sabatier reactor has less available

hydrogen available as reactant and therefore would use less CO_2, allowing more CO_2 to be processed by an ECRS. Steady-state, stoichiometric calculations were used based on the diagram in Figure 5 to determine the optimal ratio of CO_2 to divert to an ECRS against that which should be diverted to a Sabatier reactor. The amount of CO_2 available was held fixed at the per-crewmember metabolic rate (23.63 mol CO_2/CM-d) and the amount of water "supplied" varied proportionally with how much water was necessary to produce enough hydrogen to react all of the CO_2 that was diverted to the Sabatier reactor (i.e. 4 times the molar amount of metabolic CO_2 diverted to the Sabatier reactor, $4*(1-\gamma_{div})*metCO_2$). What follows is the plot shown in Figure 6, where the amount of O_2 produced by each individual system (ECRS and Sabatier) is shown with their combined O_2 production, alongside the horizontal green line of the nominal, per-crewmember, molar amount of O_2 required. In the greyed zone between $\gamma_{div} = 0$ and γ_{div} = c.a. 0.46, too much O_2 is produced, regardless of operating an ECRS, and implies that too much water is "supplied" in the analysis. The border between the left grey zone and the yellow zone is essentially the nominal case for operating only a Sabatier reactor and a water electrolyzer, i.e. the SOA on the ISS. Within the yellow zone between γ_{div} = c.a. 0.46 and γ_{div} = c.a. 0.61, too much O_2 is produced by the combined operation of an ECRS and Sabatier reactor, still showing that too much water is "supplied." The scenario that uses the lowest water mass, represented by the green zone where the total O_2 produced crosses the horizontal, nominal pre-crewmember O_2 requirement, γ_{div} = 0.614, would electrolyze 18.25 mol H_2O/CM-d, with 38.6% of metabolic CO_2 reacted in the Sabatier reactor and 61.4% reacted by the ECRS, yielding a theoretical best efficiency of 69.3% of O_2 recovered from CO_2. Any combination of an ECRS and Sabatier reactor operating with γ_{div} = c.a. 0.62 and γ_{div} = 1.0 would result in insufficient O_2 production, as the total O_2 production rate would approach the single-system efficiency of 50% recovery of O_2 from CO_2, to which the ECRS producing 100% CO is beholden. In this case, the "supplied" water is reduced to zero as γ_{div} approaches 1.0, because no H_2 is needed to react CO_2 in a Sabatier reactor if no CO_2 is being supplied to the reactor. To present this case more realistically, water would still be supplied to make up the O_2 production rate deficit, but without CO_2 being supplied to a Sabatier reactor, an excess of unused H_2 would be produced.

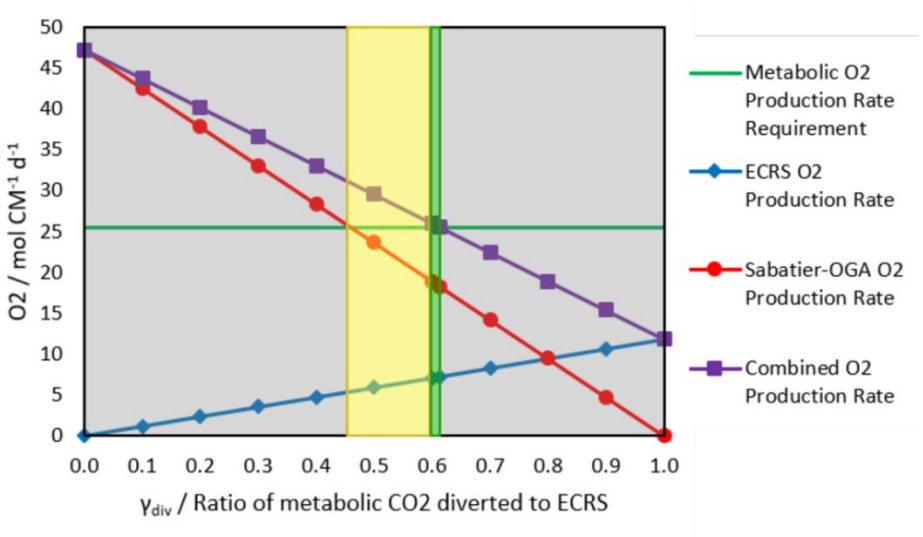

Figure 6. O_2 production rate of an ECRS and Sabatier reactor in the Application 3 architecture to determine the optimal diversion ratio of metabolic CO_2 to an ECRS (γ_{div}) that minimizes the "supplied" water (i.e. meets crewmember metabolic O_2 production rate requirements).

Compared to the ISS SOA alone, adding an ECRS would save an additional 0.13 kg H_2O/CM-d (7.25 mol H_2O/CM-d). These water savings and the related O_2 recovery percentages can viewed in Figure 7 in comparison to Application 5, as well as the ISS SOA (Figure 1) for O_2 recovery and an open-loop case where only the OGA is used to electrolyze water to generate O_2 for crew metabolic needs (Figure 8).

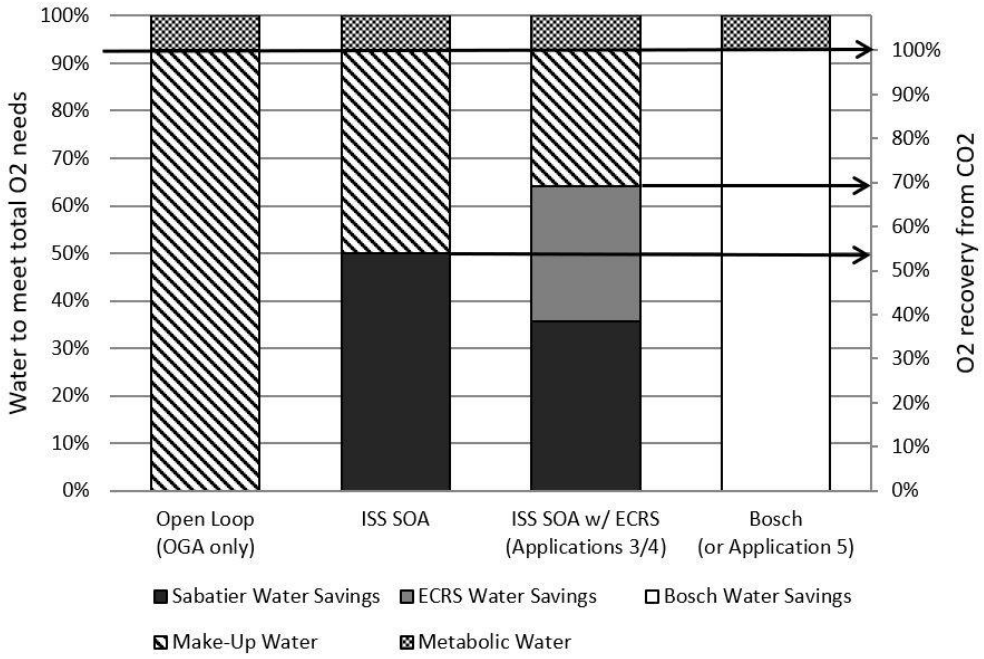

Figure 7. Comparison of system architecture water saving and O_2 recovery efficiencies for the similar Applications 3, 4, and 5 (i.e. where metabolic CO_2 is the only source of CO_2, CO_2 capture mechanism is neglected, and the ECRS products are either CO or CO and H_2)

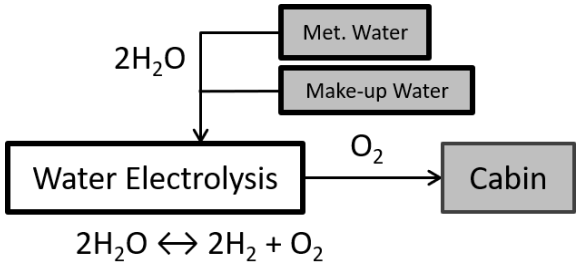

Figure 8. Block diagram of material interfaces and systems comprising an Open Loop case where all crew O_2 needs are met by electrolyzing water without any CO_2 reduction (i.e. OGA only)

3.2.4 Application 4 – ECRS for co-electrolysis to CO and H_2 with CRA support

If the product stream of an ECRS can be tuned to the proper ratio of CO to H_2 in the cathodic compartment (balanced by O_2 generation via water oxidation on the anodic side) and these products can be generated at the proper rates (see Table 4), an ECRS could replace the need for a separate water electrolyzer (e.g. the OGA) with the added functionality of co-electrolyzing CO_2. The mixed product stream of CO and H_2, produced from Equation 7 ($2CO_2 \rightarrow 2CO + O_2$) and Equation 1 ($2H_2O \rightarrow 2H_2 + O_2$) could be fed to a

Sabatier reactor to recover water; however, the CO methanation reaction, Equation 17, only generates 1 mole of water for every 3 moles of H_2.

CO Methanation $CO + 3H_2 \leftrightarrow CH_4 + H_2O$ $\Delta H^0_{rxn} = -206$ kJ/mol (17)

Ultimately, this CO_2 utilization scheme could yield the same efficiency of O_2 recovery from CO_2 as Application 3– 69.3% of O_2 from CO_2, but with one fewer large system. It is important to note that this reaction (Equation 17) alone is usually seen as undesirable because it can risk carbon formation as an unintended side-reaction, the product of which would foul the catalyst of the Sabatier reactor. In this case, the ratio of CO_2 to CO that is fed to the Sabatier reactor, along with reactor conditions, must be closely monitored. In reactors involving the co-methanation of CO and CO_2 mixed gas in the presence of H_2, it appears that having CO_2 present, rather than just CO and H_2, prevents carbon formation (and catalyst fouling), possibly through blocking the disproportionation reactor of CO to CO_2 and CO (Habazaki et al., 1998). Another practical issue that designers using this configuration would need to keep in mind is that if water needs to be electrolyzed independent of CO_2 in the same reactor (e.g. no CO_2 is available but O_2 still needs to be produced), the system must have material configurations (i.e. IL selection, electrode material) that enable HER from water at sufficient rates with no or minimal CO_2 present (which would make the solution pH higher).

3.2.5 Application 5 – ECRS with 2nd stage series Bosch reactor (replace RWGS reactor)

Similar to Application 4, an ECRS could be used to generate a mixed product stream of CO and H_2 via Equations 7 and 1, but the products could be fed to the 2nd stage reactor of a "series Bosch" system (i.e. Equations 4: CO hydrogenation, and Equation 5: Boudouard reaction), instead of to a Sabatier reactor. A Bosch reactor can theoretically reach an O_2 recovery efficiency from CO_2 of 100%. The concept of a series Bosch system, originally described by (Manning, 1976), has seen renewed interest in recent development and experimental efforts by NASA due to 1) the aforementioned need for improved O_2 recovery from CO_2, and 2) the serial aspect of the reactors allowing each reactor to be optimized for one stage of the reactions

that make up the overall Bosch process (Abney et al., 2014, 2015; Abney, Mansell, et al., 2013; Abney & Mansell, 2010, 2011; Stanley et al., 2018). In these recent efforts, membrane separators are used to remove and recycle CO_2 and excess H_2 from the feed gas to the 2nd stage reactor (a carbon formation reactor, or CFR) to promote the most favorable conditions for the formation of solid carbon via Equations 4 and 5. This architecture for a series Bosch system is shown in Figure 9 for comparison.

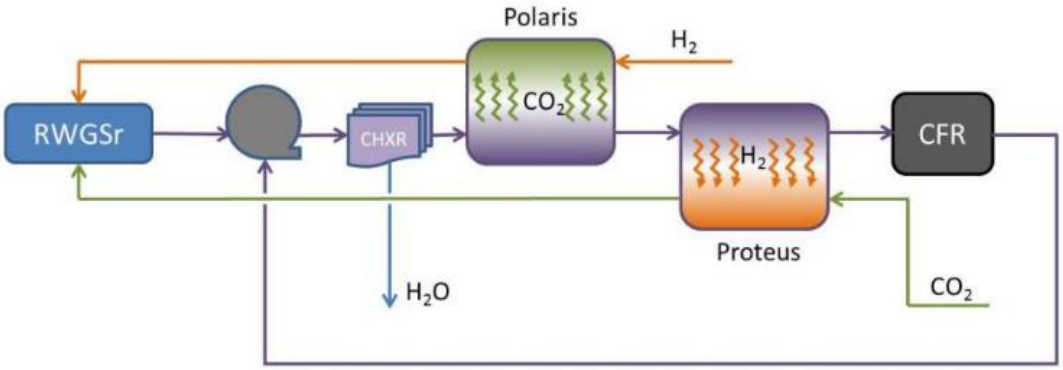

Figure 9. "Series-Bosch Approach for Oxygen Recovery" as presented by (Abney et al., 2015) – NOTE: CHXR stands for condensing heat exchanger, and "Polaris" and "Proteus" are trade names given to the CO_2 and H_2 separating membranes, respectively

In this Application case, the ECRS would effectively replace the 1st stage of a series Bosch reactor (Equation 3, the RWGS reaction) and reduce or eliminate the need for membrane separators in the reactor series. An ECRS would operate at a significantly lower temperature (c.a. 20−40°C, i.e. room temperature) than a RWGS reactor (recent RWGS reactor temperature setpoints have been c.a. 700°C) (Stanley et al., 2018) and produce the desired feed for the CFR, or 2nd stage of the series Bosch (typical reactor temperature 475-600°C), of CO and H_2. Unreacted CO and H_2 could be looped back to the ECRS with the product CO_2 and H_2O to increase overall system efficiency if it can be shown that they either do not represent a significant portion of the post-CFR gas or that they do not adversely affect operation of the ECRS. A representative schematic of this system architecture is shown in Figure 10. A comparison of this Application architecture with Applications 3 and 4, the ISS SOA, and a baseline case of only water electrolysis used to support O_2 production for crew metabolic O_2 needs can be seen in the previously shown Figure 7.

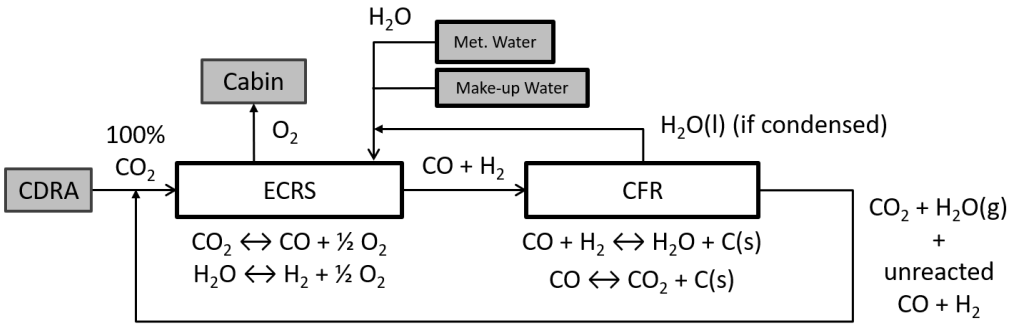

Figure 10. Block diagram of material interfaces and systems comprising Application 5

3.2.6 Application 6 – ECRS without CDRA

Currently aboard the ISS, the Carbon Dioxide Removal Assembly (CDRA) removes CO_2 from the cabin atmosphere and stores it as concentrated, high pressure CO_2 (Knox, 2000). The CDRA uses thermal/pressure-swing adsorption/desorption cycles of zeolite canisters to concentrate CO_2, and a pump to compress it. There have been issues with dust generated from the solid material fouling filters and valves that have caused numerous maintenance issues (Gentry & Cover, 2015). It was already discussed that some ILs have high solubility for CO_2, which is why there is interest in using them in CO_2 capture and separation systems (Noble & Gin, 2011; Seo et al., 2014; Wickham, Gleason, Engel, & Systems, 2015). One system configuration could concentrate CO_2 in an IL as part of a CO_2 adsorption system, and then transfer the CO_2-laden IL to an ECRS for reducing the CO_2 present in the IL. Using the generic cell presented in Figure 4, a continuous ECRS could be designed where CO_2 is introduced through a gas diffusion electrode as the electrochemical process is driven simultaneously. The CO_2 could also be introduced into the IL in an upstream contactor, microgravity versions of which have been a subject of recent investigation (Arquilla et al., 2017). The balance between CO_2 solubility, CO_2 concentration in the atmosphere, gas flow rates, liquid flow rates, CO_2 removal rates, and required O_2 generation rates would require careful consideration in such a system.

3.2.7 Application 7 – ECRS to replace ISS SOA as All-in One or All-in-Two

CO and CH_4 can be produced simultaneously in an ECRS, but other reaction products usually occur as well; in general, this wide of a product distribution is seen as undesirable, but such a mixed product

stream could be beneficial if the products are formed in the proper ratios (J. P. Jones et al., 2014). Such a process combination in one reactor (Equation 1: $2H_2O \rightarrow 2H_2 + O_2$; Equation 7: $2CO_2 \rightarrow 2CO + O_2$; Equation 8: $2CO_2 + 2H_2O \rightarrow CH_4 + 2O_2$) would need to produce 71.5% CH_4 and 28.5% CO to meet the metabolic O_2 requirements of the crew and minimize the amount of water that would need to be initially supplied. If an ECRS can be designed to produce these product ratios consistently, it could effectively replace the need for both a water electrolyzer and Sabatier reactor, and it would have additional O_2 recovery from CO_2 (69.3%) compared with the SOA (54%). This is true even if the products of CO, H_2, and CH_4 are all vented. Product utilization could further improve the utility of this version of an ECRS but would require an additional reactor or means of product separation.

3.3 Process Rate and Reactor Sizing

Feasibility for implementing an electrochemical CO_2 reduction system for the various spaceflight applications can be established to a first order approximation based on energetic efficiency (derived from overpotential and faradaic efficiency) and process effectiveness (derived from current density and faradaic efficiency). In these applications, emphasis is placed on mass, volume, and power as primary metrics to determine if a process should be considered for technology development system design. Safety, robustness, reliability, and lifetime (i.e. performance stability) are all dependent on the design, assessment, and thorough testing of the resultant system. Energetic efficiency and the necessary production rates can be translated to power requirements for an ECRS. Process effectiveness can be directly translated to reactor size and indirectly translated to system mass, based on referencing the size, mass, and O_2 production rate of the OGA because of the similarities in process controls required for water electrolysis with the OGA compared to an ECRS.

Depending on the application and supporting systems, an electrochemical CO_2 reduction system will be required to reduce a certain amount of CO_2 and/or H_2 and CH_4 per day. From Faraday's first law of electrolysis (Equation 18) one can determine how much charge needs to be passed for a given reaction, i.e.

CO_2 to CO or H^+ to H_2, and because charge (Q) is current multiplied by time, we can solve for the constant current supply necessary for daily production rate requirements.

Faraday's First Law of Electrolysis $$i = F \cdot z \cdot n_k / t \quad (18)$$

where n = number of moles of product k, i is the amount of current passed, t is the duration of the process, F is Faraday's constant, z is the number of electrons required per the half-reaction.

As an example, to electrolyze all of the CO_2 generated by one crew member (CM) per day (1.04 kg CO_2/CM-d or 23.64 moles CO_2/CM-d) to CO (a 2-electron reduction), it would require 1267 A-h or a constant 53 A for 24 hours. From stoichiometry (Equation 7) we can see that this in turn provides 11.8 moles O_2/CM-d. Table 4 shows this calculation carried out for each application described in the previous section, assuming that all current goes towards the process reaction(s) (i.e. no losses). This is useful in that it allows determination of the necessary working electrode area of an electrochemical cell with a given a Faradaic current density (process effectiveness).

Table 4. Reactant supply, Faradaic efficiency, O_2 generated, process current, and process effectiveness required for an ECRS in each application 1-7, per 1 crew member (CO and H_2 require a 2-electron reduction, CH_4 requires an 8-electron reduction)

Application	Reactant req. by ECRS (mol/CM-d)		Faradaic efficiency (FE) for each product (%)			O_2 generated by ECRS (mol/CM-d)	Total Faradaic current (A/CM)	Faradaic current for each product (A/CM)		
	CO_2	H_2O	CO	H_2	CH_4			CO	H_2	CH_4
A1	51	-	100	-	-	25.5	114	114	-	-
A2	12.8	25.5	-	-	100	25.5	114	-	-	114
A3	14.5	-	100	-	-	7.3	32	32	-	-
A4	23.6	27.4	46.5	53.5		25.5	114	53	61	-
A5	23.6	27.4	46.5	53.		25.5	114	53	61	
A6	23.6	27.4	46.5	53.5		25.5	114	53	61	
A7	23.6	18.2	28.5	-	71.5	25.5	114	33	-	81

Note: CO and H_2 require a z = 2 electron reduction and CH_4 requires a z = 8 electron reduction, for calculations using Equation 18. All values normalized to the necessary O_2 production rate to support 4 CM in each application.

Faradaic current density (or $\varepsilon_{process}$) of an electrochemical process can be determined experimentally based on product analysis, the working electrode surface area, and the current response at an applied voltage

for the experiment. A Faradaic current is current that goes entirely towards driving reaction progress, not towards ohmic losses (non-Faradaic current) within the cell or system, and it is essentially a measure of reaction kinetics. As discussed previously, catalyst design, electrode material and surface morphology, solvent, and electrolyte can all play a role in affecting the Faradaic current density of an electrochemical system in response to an applied voltage. Assuming that the Faradaic current density (or at least current density and Faradaic efficiency) are reported for a given electrochemical CO_2 reduction experiment, the necessary electrode area to meet the O_2 production rates for spaceflight applications can be determined.

For reference to experimental research, one of the more recent investigations of electrode materials and ILs looked at using molybdenum disulphide (MoS_2) with molybdenum-terminated edges as a cathode material in water with 4 mol% [emim][BF_4] (Mohammad Asadi et al., 2014). This electrochemical system, with a cathode consisting of vertically aligned MoS_2 edges, was able to achieve a current density of 130 mA/cm^2 with a FE_{CO} of c.a. 98% at a cathode potential of –0.764 V vs. reversible hydrogen electrode (RHE) in a CO_2 saturated solution. The bulk MoS_2-based cathode was tested for 10 h with c.a. 43 mA/cm^2 at –0.764 V vs. RHE with 96 mol% water (4 mol% [emim][BF_4]) with no apparent loss in current density.

To compare current density and electrode area with size and mass of an ECRS, the OGA (also an electrolysis process) can be used as a reference. The OGA has a current density of 220 mA/cm^2 while operating at 1.67 V across each cell, representing an overpotential of 0.45 V for water electrolysis (Mitlitsky, Myers, Weisberg, & A, 1999; K. C. Takada, Ghariani, & Van Keuren, 2015). It was originally sized to meet the metabolic O_2 needs of 6.5 crew members on a day/night cycle (5.44 kg O_2/d), but operated continuously could produce O_2 needs of 11.1 crew members (9.27 kg O_2/d) (Schaezler & Cook, 2015). The area of each cathode can be roughly calculated as 250 cm^2 and there are 28 cells, for a total working area of 7000 cm^2. The maximum current supply to the OGA is 1540 A for the whole cell stack, with each cell receiving up to 55 A. In this configuration on the ISS, the OGA is 386 kg for the entire assembly, including power supply, pumps, containment, etc. and fits within the space of ¾ of an ISS International Standard Payload Rack (Cloud et al., 1999). If the OGA's electrochemical cell stack were to be scaled down linearly

to meet the demands of 4 crew members (a reasonable estimate for the crew size of upcoming missions (Gatens et al., 2015)), then the OGA would only need a total working electrode area of 2520 cm^2, rather than 7000 cm^2. For the given current density of 220 mA/cm^2, this 4 CM-scaled total working electrode area tracks very closely with the minimum required electrode area to meet the nominal, or average, O_2 production needs for a crew of 4, as seen in Figure 11. It is, however, likely that the unit would need to be sized larger in its practical application to be able to account for metabolic variation in crew O_2 needs.

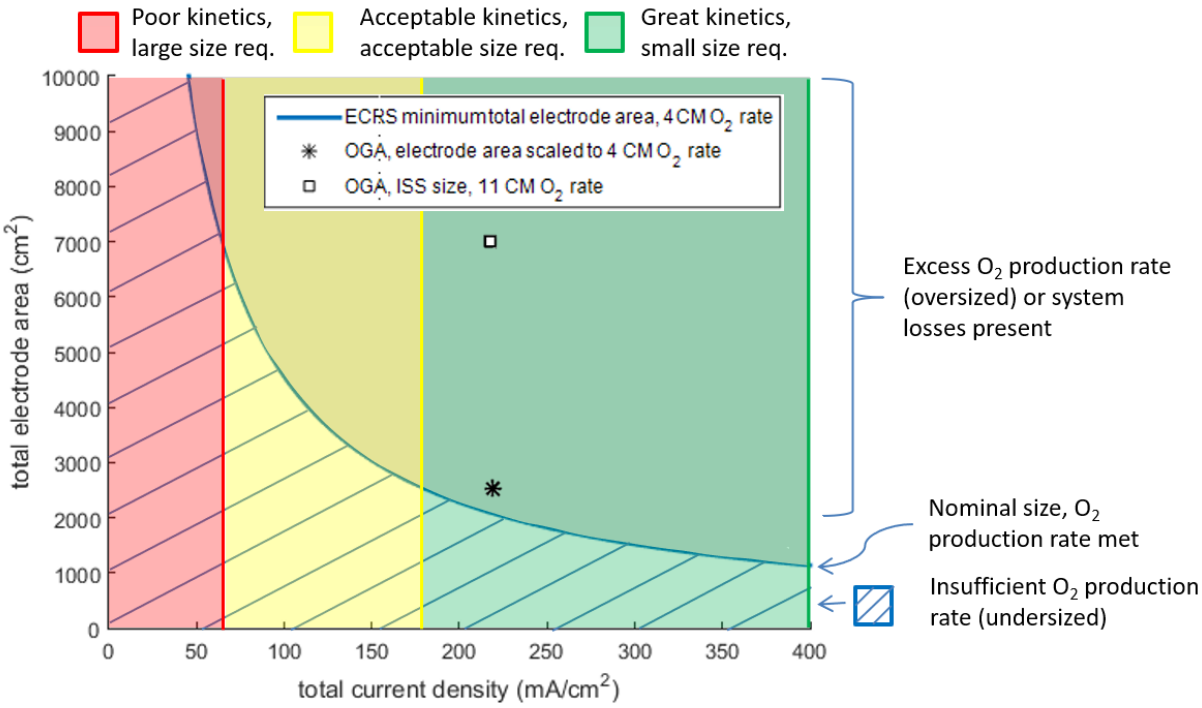

Figure 11. For a given total current density, the curve represents the minimum total electrode area that is required to meet the nominal metabolic O_2 needs of a crew of 4. The hashed area below the curve represents insufficient electrode area for a given current density to meet O_2 needs; and the area above the curve represents an excess of electrode area for a given current density to meet O_2 needs. The nominal curve assumes 100% Faradaic efficiency for the desired products.

Faradaic current density from an experimental measurement can serve as a proxy for system size and mass through the required electrode area: higher current density capability requires a smaller reactor size and small current density requires a large reactor. The question becomes: what current density needs to be achieved for an ECRS to be a reasonable size and mass, assuming it is capable of generating the desired product selectivity for the application?

Based on sizing an ECRS to meet the metabolic O_2 consumption requirements of a crew of 4, and the required total Faradaic current per crew member (114 A/CM) for an ECRS in Table 4, the minimum total electrode area of an ECRS is calculated and shown in Figure 11 (Applications 1, 2, and 4–7). This calculation assumes an ideal product distribution (i.e. Faradaic efficiencies reported in Table 4) and that all current drives a reaction (i.e. no ohmic losses). While this is an ideal case, it provides a lower limit for reactor size at a given total current density.

Drawing from the curve in Figure 11, a total Faradaic current density of c.a. 65 mA/cm^2 would result in an ECRS with a working electrode area on the order of 7000 cm^2, whereas a total Faradaic current density of c.a. 180 mA/cm^2 would result in an ECRS electrode area on the order of 2500 cm^2. The total electrode surface area values of 7000 cm^2 and 2500 cm^2 correspond to the total electrode surface area of the present-day ISS OGA and a 4 CM-scaled OGA, respectively. It is assumed that because water electrolysis and solvated CO_2 electrolysis are similar enough processes, we can infer that an ECRS with a similar electrode surface area and producing O_2 would be on the same order of magnitude of mass and size as the OGA. Due to the lower required processing rate for either an ECRS or OGA scaled to produce O_2 at a 4 CM consumption rate (i.e. less total flow reducing pump, component, and plumbing size), this order of magnitude estimate is likely conservative. It is important to note that the size and mass of the ISS OGA includes balance of plant components, while estimates for these components are not made for the proposed ECRS. These would be application-specific and dependent upon such conditions as reactor kinetics and transport issues, type of electrodes, CO_2 solubility and CO_2 capture interface, product distribution and the necessity of product separation.

This allows us to estimate zones of feasibility based on current density and overlay them on Figure 11. On the left of the figure is the area lower than 65 mA/cm^2, representing relatively poor kinetics that would require a large amount of electrode area to meet O_2 production rate requirements, and thereby an ECRS that is likely larger and more massive than the present-day OGA. In the middle, between 65 mA/cm^2 and 180 mA/cm^2, is the zone of acceptable electrode area where an ECRS would be expected to be on the same

order, or slightly lower, of mass and size as the OGA. Finally, on the right of Figure 11, above 180 mA/cm^2, an ECRS would be expected to be slightly smaller and less massive than the OGA. Not shown in this figure but for Application 3, if an ECRS only needs to process 14.5 moles CO_2/CM-d and is used with a Sabatier reactor and the OGA in a system designed to meet the metabolic O_2 needs of 4 crew members, a Faradaic current density of just 50 mA/cm^2 would yield an ECRS with a working electrode area of 2500 cm^2.

It should be noted that in recent papers by Takada et al. (2015) and (2018), advancements to a new generation of the OGA are suggested that could decrease the mass of the OGA from 386 kg to approximately 248 kg (K. Takada et al., 2018; K. C. Takada et al., 2015). These modifications include removing the massive (125 kg) hydrogen dome container and replacing it with a lightweight shroud and downsizing the power supply (45 kg resized to 32 kg) to meet actual power needs instead of the excessive power for meeting the O_2 production rate of 11.1 CM. With these modifications in mind, an ECRS may be similarly sized to a new generation OGA and therefore, 248 kg would be a more suitable comparison mass for such a system (not including spare parts).

3.4 Energy Efficiency and Power Demands

Electrochemical CO_2 reduction generally has a high overpotential which can be thought of as an activation energy barrier to reducing a very stably oxidized molecule. ILs in combination with certain electrode materials have been seen to lower this activation energy barrier to further reduced products, and therefore decreasing the power demands of an ECRS.

The power required to run an electrochemical process depends both on the current and the applied voltage across the electrodes ($P = iV$) at a given temperature. From a system standpoint, the applied potential (independent of resistive losses) will also determine if the process is endothermic or exothermic, based on the thermoneutral voltage (E_{TH}). The thermoneutral voltage can be calculated based on enthalpy of reaction (ΔH^0_{rxn}), rather than the Gibb's free energy. Applying a voltage above the thermoneutral voltage will require heat removal (exothermic), whereas applying a voltage below it will require heat addition

(endothermic). At temperatures below 100°C, E_{TH} for both CO_2 electrolysis to CO and H_2O electrolysis are approximately 1.47 V across a cell. If the environment temperatures are similar to the operating temperatures for an ECRS, the impact of (likely) excess thermal energy will be small compared to the impact of electrical power requirements for the process. Still, this aspect should be kept in mind, especially in microgravity settings where thermal management becomes much more difficult without free convection. More detailed discussions of how this can affect electrolyzer power consumption at a system level are available in papers by (Graves, 2010b) and (Iacomini & Sridhar, 2005), the latter of which pays particular attention to Applications 1 and 2 where Mars surface temperatures could significantly affect the required input heat.

The theoretical equilibrium potential for CO_2 reduction to CO (-0.52 V) and for water oxidation (0.81 V) at pH 7 would require a total of 1.33 V across the cell. Where CO is the desired reduction product, applied cell potentials in excess of 1.33 V are overpotentials that contribute to decreased energy efficiency of the electrochemical cell. However, overpotential is required to overcome the activation energy barrier to drive a reaction at desired rates, and its relation to current can be understood from the Butler-Volmer equation, Equation 19 (Sridhar & Vaniman, 1997).

Bulter-Volmer equation
$$i = i_o \left[\exp\left(\frac{\eta}{\beta_a}\right) - \exp\left(\frac{-\eta}{\beta_c}\right)\right] \quad (19)$$

where i is current, i_o is exchange current (dependent on temperature, concentration, and catalyst), η is overpotential, and β_a and β_c are dependent on electrode kinetics at the a anode, and c cathode.

Based on the necessity of overpotential and how energy efficiency is defined for an electrochemical process (Equation 15), it is clear that a system with 100% energy efficiency will be of no use, as no meaningful amount of current will flow. Therefore, energy efficiency must be reported with respect to current or current density to be meaningful and relevant. It is important to note that the described energy efficiency does not consider the energy required for heating, pumping, product separation, etc. associated with an entire CO_2 reduction system, nor the losses due to cell resistance that result in heat production.

As a baseline, the power directly supplied to the electrolysis process is considered. In Applications 1, 2, and 4–7, a constant current of 114 A/CM is required to meet the desired O_2 production rates per crew member. The cell equilibrium potentials fall within 1.05 and 1.33 V for all of the reactions desired in each Application (H_2, CO, and CH_4). Because it is likely that future missions will feature a crew of 4, a constant current of 456 A will be required to meet O_2 consumption demands. As a lower limit (albeit impossible to achieve), this amount of current at 1.05 and 1.33 V would require a constant power draw of 478–606 W. For a more reasonable and practical range, cell overpotentials could be on the order of 0.4 V (typical of water electrolysis) to 1.7 V (upper limit for CO_2 electrolysis) in an optimized cell (minimized cell resistance). As an example, in the case of CO and O_2 production from only CO_2 ($E_{eq,cell}$ = 1.33 V), these overpotentials would necessitate a constant power draw of 789 (η = 0.4V) to 1,381 W (η = 1.7V), with a respective process energy efficiency of 77% and 44%. For comparison, an OGA scaled down to produce O_2 at a 4-crew member rate would operate at 1.67 V and still require 456 A of current, yielding a constant power draw of 761 W at a process energy efficiency of 74%. If Application 3 is considered instead (a constant 32.41 A/CM or 129.64 A, total) with the same overpotential range, such an electrolysis process would require 224 W (η = 0.4V) to 393 W (η = 1.7V).

3.5 Conclusions

There are a number of mission scenarios in which an ECRS could be viable for meeting or assisting in meeting crewmember metabolic O_2 requirements, assuming that proposed current density, faradaic efficiency, and overpotentials can be achieved. One major design consideration will be how the CO_2 is introduced to the electrolyzer (either in gas phase or in solution). Dilute CO_2 could be concentrated in the IL upstream of the electrolyzer, eliminating the need for a separate CO_2 capture system, if production rates are allowed to be slow (i.e. long term O_2 production on Mars) or system size can be made larger to accommodate inherently limited solvated CO_2 electrolysis rates. But if CO_2 is concentrated and/or pressurized in a separate system, the gas-phase CO_2 introduced at a gas diffusion electrode could improve

O_2 production rates significantly, as has already been seen in other studies, making for smaller reactors capable of on-demand processing (Weekes et al., 2018).

First order estimates for system size and power requirements were estimated based on crew size, metabolic requirements, and recent and reasonable performance metrics for an ECRS. These metrics can be used by system concept designers and future technology developers to justify more research and development into such CO_2 electrolyzers for improved performance and/or testing of long term reliability, safety, and robustness.

3.6 Related Presentations and Publications:

Holquist, J. B., Klaus, D. M., Nabity, J. A., and Abney, M. A. (2015). Opportunities and Challenges for Direct Oxygen Generation using Electrochemical Carbon Dioxide Reduction Catalyzed by Room Temperature Ionic Liquids (poster, 2nd place), *45th International Conference on Environmental Systems*, Bellevue, WA.

Holquist, J. B., Klaus, D. M., Nabity, J. A., and Abney, M. B. (2016). Ionic Liquid Selection and Initial Test Results for Electrochemical Carbon Dioxide Reduction (poster, 1st place), *46th International Conference on Environmental Systems*, Vienna, Austria.

Holquist, J. B., Klaus, D. M., Nabity, J. A., and Abney, M. A. (2016). Electrochemical Carbon Dioxide Reduction with Room Temperature Ionic Liquids for Space Exploration Missions, ICES-2016-314, pp. 1–19.

Electrochemical Carbon Dioxide Reduction with Room Temperature Ionic Liquids for Space Exploration Missions. *46th International Conference on Environmental Systems* (ICES), Vienna, Austria, July 2016 (presentation).

Chapter 4 – Ionic Liquid Selection & Property Measurements

4.1 Ionic Liquid Selection Rationale

An extensive literature review was conducted on the current state-of-the-art IL and electrochemical cell technology with a focus on CO_2 capture and reduction, specifically to the products CO and O_2. Studies utilizing ILs have shown that the IL in particular can affect product selectivity, overpotential, and/or current density when coupled to the appropriate selection of electrode material (Mohammad Asadi et al., 2014; DiMeglio & Rosenthal, 2013; Medina-Ramos et al., 2014, 2015; J. Rosen, 2016; Sun et al., 2014). A thorough review of CO promoting ILs was conducted by (Alvarez-Guerra et al., 2015) in early 2015. The majority of IL-based electrochemical CO_2 reduction has focused on cations that have imidazole as the parent heterocycle (e.g. 1-ethyl-3-methylimidazolium [emim] and 1-butyl-3-methylimidazolium [bmim]). Many analogous CO_2 reduction studies have seen that added nitrogen groups to an electrode or homogeneous catalyst (e.g. pyridinic and pyrrolic nitrogen) can affect CO_2 reduction (Barton Cole et al., 2010; Kumar et al., 2013; Lim, Holder, Hynes, & Musgrave, 2014; Lim, Holder, & Musgrave, 2013; Smith & Pickup, 2010; Tornow, Thorson, Ma, Gewirth, & Kenis, 2012; Wu et al., 2015). It appears reasonable to postulate that the number of nitrogen atoms in an IL, particularly in the cation's heterocyclic ring, could have a major effect on performance of the IL in affecting electrochemical CO_2 reduction without causing undue negative effects.

Looking further into the reaction mechanisms of CO_2 reduction assisted by ILs, recent work by (Tanner et al., 2016) tested the mechanism proposed by (B. A. Rosen et al., 2011) that a radical carbon dioxide anion interacts with the cation of the IL, after the slow, rate determining electrochemical step of reduction of CO_2 to the radical anion. Tanner et al. showed that varying the cation structure (using [emim], [pmim], [bmim], and [bmpyrr]) caused an observable shift in peak current density by a factor of 2 using otherwise the same cell and electrodes. While the electrode material selection could change the current density by a factor of 6 in the tested electrodes (silver induced a 6 times higher current density than gold, when both were used in conjunction with the same ionic liquid), the cation effect is still appreciable and shows that an

alternative mechanism for CO_2 reduction is at play. The mechanism proposed by Tanner et al., described below in Figure 12, suggests that the cation binds to the silver surface first, desorbs, and allows a CO_2 molecule to access the silver surface prior to an irreversible reduction of the CO_2. In Figure 12, RDS stands for rate determining step and M represents the cation of the IL.

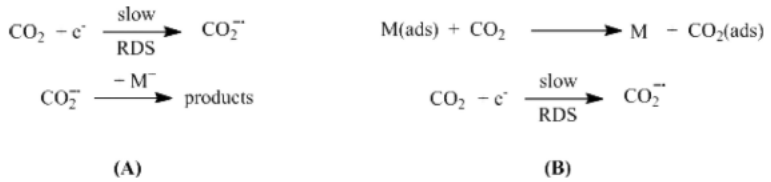

Figure 12. Two proposed mechanisms of CO_2 reduction, whereby (A) represents the mechanism previously proposed by Rosen et al. 2011 and (B) the mechanism proposed, whereby a chemical, desorption step precedes an irreversible electron transfer." (Brian A Rosen et al., 2011; Tanner et al., 2016)

This study by Tanner et al. suggests that if the cation plays a role in enhancing the CO_2 reduction kinetics, alternative cations may also have contributory effects of varying degrees. In fact, this very idea was followed up on by a study by (Zhao et al., 2016) where cations including imidazolium, pyrrolidinium, ammonium, phosphonium, and (trimethylamine)-(dimethylethylamine)-dihydroborate with various anions each exhibited a catalytic effect for electrochemical CO_2 reduction at a silver electrode in CO_2 saturated acetonitrile (MeCN) with 0.1 M tetrabutylammoniumhexafluorophosphate (*n*-Bu_4NPF_6) as the supporting electrolyte. Both cyclic voltammetry and constant potential electrolysis tests were performed to characterize the current-potential response and both gaseous and liquid products. The study suggests that many ILs co-catalytically promote electrochemical CO_2 reduction, albeit by different pathways. Specifically, it is proposed that the active form of the imidazolium co-catalyst is the reduced imidazolium radical, which forms a complex with CO_2 before the CO_2 is reduced. For most of the other cations, the catalytic activity is attributed to an electrochemical double layer effect where the cations are concentrated on the electrode surface due to the very negative charge of the cathode. Zhao et al. propose that the small cation [bmpyrr] allows a closer approach of CO_2 to the electrode surface to facilitate electron transfer, and the nitrogen site on [bmpyrr] may provide a binding site for CO_2 and stabilize the intermediate CO_2 radical anion.

While many other cations exhibited the double layer CO_2 reduction enhancement effect, the authors noted that apparently the onset and peak potentials for CO_2 reduction in solutions containing ionic liquids with nitrogen heteroatoms were significantly more positive (i.e. required a lower magnitude cathodic overpotential) than those with phosphonium-based cations. This was attributed to the more electronegative nitrogen heteroatom. For the ILs that exhibit an electrochemical double layer effect on CO_2 reduction, Zhao et al. observed that the smallest cations with the highest charge density had the best catalytic effects. This is still based on the idea that the smaller cation allows a closer approach of CO_2 to the cathode surface and that the high charge density can more effectively stabilize the CO_2 radical anion, facilitating CO_2 reduction.

Zhao et al. believe they have confirmed imidazolium mediated electrochemical CO_2 reduction via a mechanism described in a theoretical study by (Y. Wang, Hatakeyama, Ogata, & Wakabayashi, 2015), shown in Figure 13, whereby the hydrogen at the C2 position of [emim][BF_4] is considered to be the proton source that attaches to CO_2 forming the key intermediate and water acts as a co-catalyst for the source of the second proton. This is supported by the pK_a of the C2 hydrogen is estimated at 23.8 and the pK_a of the C4 and C5 hydrogen of [emim] are estimated at 34.2 and 34.4, respectively.

Mentioned by Wang et al., but not explicitly studied, was the fact that the [BF_4] anion hydrolyzes to form HF and other fluoroborates, which, as stated by (Sowmiah, Srinivasadesikan, Tseng, & Chu, 2009), can cause an apparent catalytic effect in electrochemical CO_2 reduction other than the proposed pathways. These hydrolysis products (e.g. HF and other fluorine-containing salts) are generally detrimental to overall cell health due to eventual corrosion, etching, and electrode deactivation; not to mention that HF poses an extreme health hazard to humans.

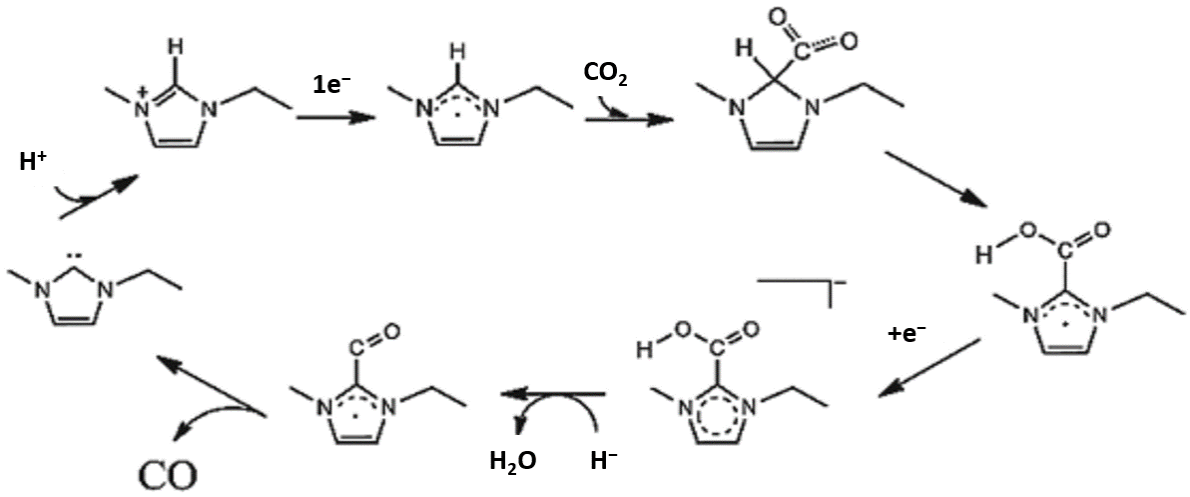

Figure 13. Scheme of CO_2 reduction mediated by imidazolium, proposed by (Y. Wang et al., 2015)

Contrary to the mechanism proposed by Wang et al. and demonstrated by Zhao et al., (Lau et al., 2016a) propose that the C2 position hydrogen on [emim] is not vital for catalysis of electrochemical CO_2 reduction, but that the C4 and C5 position hydrogens are vital. This was recognized by experimental results where the C2 position in [emim] (of [emim][BF_4]) was methylated (forming 1-ethyl-2-methyl-3-methlimidazolium [emmim]) and the onset potential of reduction and the corresponding current density improved (tests occurred in dry acetonitrile with 0.1 M *n*-Bu_4NPF_6 at a planar silver electrode). When the C4 and C5 positions on the imidazolium ring were methylated in addition to the C2 position, the reductive potential went significantly more negative and the reducing current magnitude decreased, corresponding to a decrease in catalytic activity. Their proposed mechanisms of interactions of the [emim] cation and CO_2 are described in Figure 14, where the anion radical of CO_2 is stabilized on the silver surface by 1 or 2 cations via hydrogen bond interactions.

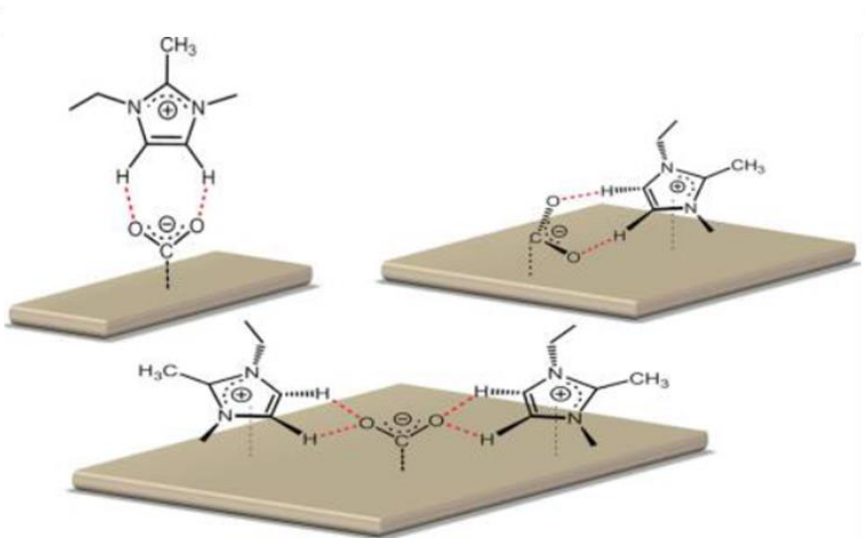

Figure 14. Scheme of CO_2 reduction mediated by imidazolium, proposed by (Lau et al., 2016b)

Additional ILs synthesized by Lau et al. attempted to investigate changing the electronic nature of the C4 and C5 protons by adding weakly electron withdrawing phenyl substituents at the C2 position. All of the ionic liquids investigated showed improved catalytic effects compared to [emim][BF_4], but no difference between one another; it was also observed via single crystal x-ray diffraction that the aromatic systems of the imidazolium and phenyl rings are not conjugated. Ionic liquids with strong electron withdrawing groups attached at the C2 position (trifluoromethyl, CF_3) were seen to decompose in the presence of CO_2 and a reductive current (although their cyclic voltammetry (CV) scans alone simply indicate a mass transport limited reduction, not necessarily decomposition).

One summary of the investigation by Lau et al. was that the imidazolium salts mainly provide a CO_2-activating effect, but do not act as an electron shuttle− in contrast to the mechanism proposed and investigated by Wang et al. and Zhao et al., respectively. Lau et al. also point out, however, that their mechanism may not be the only contributor to electrocatalytic CO_2 reduction.

4.1.1 Concentration dependence

In the study by Zhao et al., the concentration of the ionic liquid [dmim][BF_4] was varied as 2.0, 4.0, 50.0, and 100.0 mM in the MeCN (0.1 M *n*-Bu_4NPF_6) solution, with either N_2 or CO_2 sparged through the

solution. From this study, the authors conclude that, with low concentrations (2.0 and 4.0 mM [dmim][BF_4]), the CO_2 reduction reaction is first order in CO_2 concentration due to the large excess of CO_2. However, as the concentration of [dmim][BF_4] increases, the partial depletion of CO_2 near the electrode occurs and mass transport of CO_2 from the bulk solution to the electrode surface limits the current response of the electrochemical CO_2 reduction pathway (CV in an unstirred cell). Therefore, while having a higher concentration of IL may increase the CO_2 concentration in solution, mass transport limitations can occur at higher IL content, possibly due to the IL blocking access of the CO_2 to the electrode.

4.1.2 Water Dependence & Stability

Zhao et al. observed that, in the absence of a proton source (e.g. water) the imidazolium-based ionic liquids were deactivated over time with bulk electrolysis for CO_2 reduction. Upon addition of water (or if water was deliberately added to the original solution), the imidazolium cation was reactivated. For the other ionic liquids that only had an electrochemical double layer effect on CO_2 reduction, added water did not significantly affect the process.

The presence of water as a proton donor also significantly affects the faradaic efficiency for various products when the imidazolium cation is present. It does not have a significant effect on products when the pyrrolidinium cation is present. These results can be seen in Table 5 from Zhao et al.

Table 5. Products formed by bulk electrolysis of CO_2 at a Ag cathode in MeCN (0.1 M *n*-Bu_4NPF_6)", (Zhao et al., 2016)

Additives	E_{appied}/V *vs.* Fc/Fc^+	Charge /C	FE/%			
			H_2	CO	$C_2O_4^{2-}$	HCO_2^-
without IL[a]	-2.6[b]	12.5	0.2	53.9	39.3	0.8
2.0 mM [C_{10}mim][BF_4][a]	-2.3	28.5	0	45.1	53.4	0.4
2.0 mM [C_4mpyrd][BF_4][a]	-2.3	50.1	0	66.4	28.4	0.8
without IL + 1.0% H_2O	-2.3	15.3	87.4	9.5	3.5	---
2.0 mM [C_{10}mim][BF_4] + 1.0% H_2O	-2.3	61.8	1.8	70.4	27.1	0.4
2.0 mM [C_4mpyrd][BF_4] + 1.0% H_2O	-2.3	50.2	0.4	58.4	42.6	0.8

[a] Water content: 5.0 mM.
[b] This more negative potential was chosen to achieve a reduction rate that is comparable to that found in the presence of IL additive.

Other studies of electrochemical CO_2 reduction in aqueous imidazolium ionic liquid solutions show that significantly higher water concentrations improve the faradaic efficiency for carbon monoxide over other species at relatively low current densities (Neubauer, Krause, Schmid, Guldi, & Schmid, 2016b; Brian A Rosen et al., 2013). Still, at higher current densities (50, 100, 200 mA/cm^2), the hydrogen evolution reaction will begin to prevail and the stability of the ionic liquid may be in jeopardy. The proposed mechanism of [emim][OTf] instability at high current densities by Neubauer et al. is that local hot spots of high pH (high OH^- concentration) close to the electrode initiate decomposition of [emim], as high basicity can cause decomposition of imidazolium cations by attack at the C2 position (Sowmiah et al., 2009).

4.1.3 pH Dependence

To minimize this possible decomposition pathway of imidazolium, (Z. Liu et al., 2015) have employed ionic liquids such as [emim][Cl] with added HCl to tune the pH of the solution (using [Cl] as the anion also eliminates the hydrolytic stability issue of anions like [BF_4] and [PF_6]). By adjusting the pH lower (higher H^+ concentration), the hydrogen evolution reaction becomes more favorable, reducing the faradaic efficiency for CO and adjusting the ratio of product H_2 to CO to be more favorable for H_2. Importantly, H_2/CO ratios in the range of 1/1 to 4/1 are desirable in Fisher-Tropsch synthesis of fuels, and such ratios are termed "syngas," short for synthesis gas. These ratios may also be desirable for feeding into a Sabatier reactor or into a Boudouard reactor used in spacecraft CO_2 reduction applications.

4.2 Summary and Ionic Liquid Selection

To summarize the discussion above and apply it to selection of ILs for further study, the following points are made:

1) There is strong indication that nitrogen heterocycle cation-based ionic liquids have a co-catalytic effect for electrochemical CO_2 reduction with a silver electrode surface

2) Multiple reaction mechanisms may be at play for imidazolium cations, including nucleophilic attack of CO_2 by the imidazolium cation at the C2 position with the C2 hydrogen being donated to CO_2 and

subsequently regenerated in the presence of a proton donor, such as water; and a mechanism through hydrogen bond interaction of the C4 and C5 protons of imidazolium with the CO_2 anion radical. For pyrrolidinium ionic liquids, an electrochemical double layer effect may be the cause of facilitating electrochemical CO_2 reduction while suppressing the hydrogen evolution reaction in aqueous media.

3) The pK_a of the various hydrogens attached to carbon atoms in the heterocyclic ring of the ionic liquid cation may affect the reaction mechanism by proton donation.

4) Reduced forms of the cations may also be the electroactive species.

5) Positively charged nitrogen atoms in the heterocyclic ring may be a point of CO_2 anion radical stabilization.

6) Some instability of the imidazolium cation is present in strong bases due to the reactivity of the C2 position hydrogen of the imidazolium cation. The presence of proton donating buffers (water) minimize but do not eliminate this decomposition pathway.

7) $[BF_4]$ and $[PF_6]$ anions should not be used in any electrochemical cell with water present, due to hydrolysis of the anion to form HF and other adventitious reactants.

8) More acidic ionic liquids, e.g. [emim][Cl], have been used to mitigate basic decomposition of ionic liquids with positive results (the chloride anion with added, chloride-based supporting electrolyte serving to buffer hydroxide anions generated in CO_2 reduction, or to force the reaction pathway through a proton generating mechanism, rather than hydroxide generating).

With all of these thoughts in concert, it appears that the exact reaction mechanism remains unclear. Changing the base structure of the nitrogen heterocycle cations of ILs may alter the interaction of the cation with CO_2 by varying the pK_a of the hydrogen atoms bonded to carbon atoms in the heterocyclic ring and by changing the location and magnitude of charge density on the ring, among other possible but unknown mechanisms. Therefore, aromatic, heterocyclic cations were selection with a varied number of nitrogen

atoms in the aromatic ring to probe their effect in catalytic activity for CO_2 reduction to CO. The seven ionic liquids below in Table 6 have been selected to be investigated for supporting electrochemical CO_2 reduction as solvent, electrolyte, and co-catalyst.

Table 6. List of the ionic liquids selected for synthesis and/or procurement

Cation Structure	Abbrev.	Cation Name	Anion Structure	Abbrev.	Anion Name
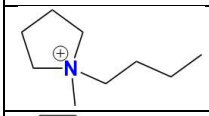	[bmpyrr]*	1-butyl-1-methylpyrrolidinium	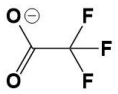	$[TFA]^-$	trifluoro-acetate
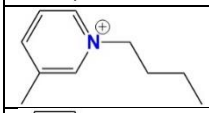	[bmpy]*	1-butyl-3-methylpyridinium	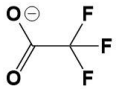	$[TFA]^-$	trifluoro-acetate
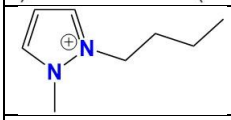	[bmpz]*	1-butyl-2-methylpyrazolium	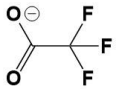	$[TFA]^-$	trifluoro-acetate
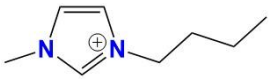	[bmim]†	1-butyl-3-methylimidazolium	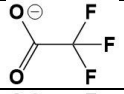	$[TFA]^-$	trifluoro-acetate
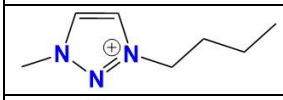	[bm3tri]*	1-butyl-3-methyl-1,2,3-triazolium	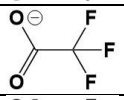	$[TFA]^-$	trifluoro-acetate
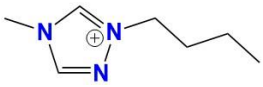	[bm4tri]*	1-butyl-4-methyl-1,2,4-triazolium	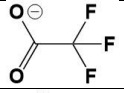	$[TFA]^-$	trifluoro-acetate
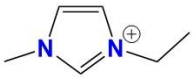	[emim]†	1-ethyl-3-methylimidazolium	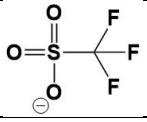	$[OTf]^-$	trifluoro-methane-sulfonate

*synthesized by Mark S. Paley at NASA Marshall Space Flight Center
†procured from Iolitec, Inc (USA)

Pyrrolidinium and imidazolium-based ionic liquids were selected to compare with literature. Pyridinium was selected to test it in a similar system to the other ionic liquids and observe if catalytic behavior at other electrode materials translates to catalytic behavior at silver (or similar electrodes) for CO_2 reduction to CO. Pyrazolium, 1,2,3-triazolium, and 1,2,4-triazolium cation-based ionic liquids were selected to probe the effect of changing the base structure of the nitrogen heterocycle.

Trifluoroacetate was selection as the anion due to its expected miscibility with water throughout concentration ranges (Zhou et al., 2012), and the weaker acidity compared with other fluorinated anions (i.e. triflate is the counter anion to the super acid triflic acid or trifluoromethanesulfonic acid), allowing for

reduced concern of corrosion of electrochemical cell materials in an application environment and a weakly acidic environment for CO_2 reduction.

The IL [emim][OTf] was selected and procured in a large quantity (500g) because its properties have been reported in literature (Berthod, Ruiz-Ángel, & Carda-Broch, 2008; Ohno & Yoshizawa, 2002; Soriano, Doma, & Li, 2009; Tenney et al., 2014), it was commercially available (Iolitec), and it has been used for supporting electrochemical CO_2 reduction (Neubauer, Krause, et al., 2016b; Neubauer, Schmid, Reller, Guldi, & Schmid, 2016; Reche, Gallardo, & Guirado, 2014). As reported by (Neubauer, Krause, et al., 2016b), the [emim][OTf] IL is a good baseline IL to choose because 1) the imidazolium cation is catalytically active with silver for CO_2 reduction, 2) it is less viscous and more conductive than imidazolium cations with a longer alkyl group, 3) it is electrochemically stable from -2.6 to +2.0 V verses Fc^+/Fc, 4) it can be present in both anode and cathode compartment without decomposition, 5) with this cation, the [OTf] anion enables complete miscibility with water, 6) the anion [OTf] does not hydrolyze, as other anions are known to do, 7) the [OTf] anion has a smaller Henry's constant for CO_2 than other anions attached to [emim], without chemical absorption.

4.3 Thermophysical Properties

While some of the selected ILs have been studied in literature previously, many have not been thoroughly characterized with respect to both thermophysical properties and their influence on CO_2 electrolysis. The density, viscosity, and ionic conductivity of each neat IL and each IL in a binary solution with water throughout the entire composition range were experimentally determined. This was done because the thermophysical properties of an IL and an IL-aqueous solution can influence the performance of an IL in CO_2 electrolysis, because these properties are useful in engineering design and process control, and because understanding the influence of cation or anion selection on the nature of the IL is useful for analyzing and designing new ILs.

The ionic liquids [emim][OTf] and [bmim][TFA] were procured from Iolitec Inc. with purities of 99%. 1-butyl-1-methylpyrrolidinium bromide (99%, Iolitec) and 1-butyl-3-methylpyridinium bromide were both purchased from Iolitec Inc. with purities of 99%. Trifluoroacetic acid (99%), pyrazole (98%), 1,2,4-triazole (98%), sodium methoxide (25 wt% in methanol), and iodomethane (99%) were all purchased from Sigma Aldrich. 1-methyl-1H-1,2,3-triazole (96%+) was purchased from Ark Pharm, Inc.

4.3.1 Synthesis and Purification of Ionic Liquids

The ionic liquids [emim][OTf] and [bmim][TFA] were procured from Iolitec, both with purities of 99%. Both were dried at −30 inHg and 60°C in a vacuum flask for 24 hours, then further dried at 8 mbar and 30°C for 2 weeks. The nuclear magnetic resonance (NMR) spectra were obtained with a Bruker AV-III 300MHz, and are presented below. The synthesis and purification procedures of all remaining ILs are also presented in detail, and the images of the NMR spectra are shown in Appendix C.

4.3.1.1 1-ethyl-3-methylimidazolium trifluoromethanesulfonate, [emim][OTf]

^{1}H NMR (300 MHz, D2O, δ): 1.51 (t, 3H, CH3, J = 7.3 Hz), 3.90 (s, 3H, CH3), 4.23 (q, 2H, CH2, J = 7.3 Hz), 7.42 (s, 1H), 7.49 (s, 1H), 8.71 (s, 1H); 13C NMR (75 MHz, D2O, δ): 14.40, 35.53, 44.74, 121.83, 123.41, 135.50; 19F NMR (282 MHz, D2O, δ): −78.79 (s, 3F, CF_3S).

4.3.1.2 1-butyl-3-methylimidazolium trifluoroacetate, [bmim][TFA]

^{1}H NMR (300 MHz, D_2O, δ): 0.95 (t, 3H, CH_3, J = 7.3), 1.34 (t, 2H, CH_2, J = 7.64), 1.87 (quint, 2H, CH_2, J = 7.53), 3.92 (s, 3H, CH_3), 4.22 (t, 2H, CH_2, J = 7.1 Hz, 2H), 7.45 (s, 1H), 7.50 (s, 1H), 8.73 (s, 1H). ^{13}C NMR (75 MHz, D_2O, δ): 12.57, 18.71, 31.22, 35.56, 49.25, 114.43 (COO^-), 118.30 (CF_3), 122.20, 123.45, 135.79 (m). ^{19}F NMR (282 MHz, D_2O, δ): −75.55 (CF_3COO^-).

4.3.1.3 1-butyl-1-methylpyrrolidinium trifluoroacetate, [bmpyrr][TFA]

1-butyl-1-methylpyrrolidinium bromide (99%, Iolitec) dissolved in distilled water to a concentration of 0.20 mol/L was poured down an anion exchange column (Amberlite IRA-410 type II, strong acid anion exchange resin, 20-25 mesh, 1.25 meq/mL exchange capacity) to yield a solution of 1-butyl-1-

methylpyrrolidinium hydroxide in water (c.a. 1.5 – 2.0 L). The resulting hydroxide solution was converted to the trifluoroacetate form by adding 0.3 mol of trifluoracetic acid (99%, Sigma Aldrich) to the solution, just enough to make the solution weakly acidic (pH c.a. 3 – 4). The remaining water was removed by vacuum evaporation with a rotary evaporator first, then by vacuum oven for one week (−30 inHg, 80°C), leaving approximately 60g of 1-butyl-1-methylpyrroidinium trifluoroacetate. ^{1}H NMR (300 MHz, D_2O, δ): 0.95 (t, 3H, CH_3, J = 7.4), 1.39 (q, 2H, CH_2, J = 7.5), 1.78 (m, 2H, CH_2, J = 7.7 Hz), 2.21 (m, 4H), 3.03 (s, 3H, CH_3), 3.26 – 3.38 (m, 2H), 3.50 (br, 4H); ^{13}C NMR (75 MHz, D_2O, δ): 12.74, 19.21, 21.26, 25.05, 47.95 t, 64.16 t, 64.20 t, 114.43 (s, COO−), 118.30 (s, CF_3); ^{19}F NMR (282 MHz, D_2O, δ):−75.54 (CF_3COO−).

4.3.1.4 1-butyl-3-methyl-pyridinium trifluoroacetate, [bmpy][TFA]

1-butyl-3-methylpyridinium bromide (99%, Iolitec) dissolved in distilled water to a concentration of 0.20 mol/L was poured down an anion exchange column to yield a solution of 1-butyl-3-methylpyridinium hydroxide in water. The hydroxide anion was converted to trifluoroacetate and the resulting ionic liquid was dried using the procedure described above, yielding approximately 80g of 1-butyl-3-methylpyridinium trifluoroacetate. ^{1}H NMR (300 MHz, D_2O, δ): 0.93 (t, 3H, CH_3, J = 7.5 Hz), 1.35 (h, 2H, CH_2, J = 7.5 Hz), 1.96 (quin, 2H, CH_2, J = 7.5 Hz), 2.54 (2, 3H, CH_3), 4.55 (t, 2H, J = 7.2 Hz), 7.92 (t, 1H, J = 7.1 Hz), 8.35 (d, 1H, J = 8.1 Hz), 8.59 – 8.72 (m, 2H). ^{13}C NMR (75 MHz, D_2O, δ): 12.60, 17.56, 18.66, 32.51, 61.47, 114.39 (COO^-), 118.26 (CF_3), 127.35, 139.87, 141.25, 143.65, 145.87; ^{19}F NMR (282 MHz, D_2O, δ): −75.54 (CF_3COO^-).

4.3.1.5 1-butyl-2-methylpyrazoilum trifluoroacetate, [bmpz][TFA]

Pyrazole (98%, Sigma Aldrich, 0.30 mol) was reacted with slightly over 0.30 mol of methyl iodide (99%, Sigma Aldrich) and sodium methoxide (25wt% in methanol, Sigma Aldrich). The resulting 1-methylpyrazole was alkylated with 1-bromobutane in acetonitrile (99%, Sigma Aldrich) to form 1-butyl-2-methylpyrazolium bromide. This hydroxide anion was replaced with trifluoroacetate and the resulting ionic liquid was dried using the anion exchange and drying methods described above, yielding 70g of 1-butyl-2-

methylpyrazolium trifluoroacetate. ^{1}H NMR (300 MHz, D_2O, δ): 0.97 (t, 3H, CH_3, J = 7.4), 1.40 (h, 2H, CH_2, J = 7.67 Hz), 1.92 (quint, 2H, CH_2, J = 7.67 Hz), 4.15 (s, 3H, CH_3), 4.46 (t, 2H, CH_2, J = 7.12 Hz), 6.77 (s, 1H), 8.16 (s, 1H), 8.22 (s, 1H). ^{13}C NMR (75 MHz, D_2O, δ): 12.58, 18.77, 29.93, 36.46, 49.67, 107.15, 114.42 (COO^-), 118.28 (CF_3), 136.59, 137.81. ^{19}F NMR (282 MHz, D_2O, δ): 75.54 (CF_3COO^-).

4.3.1.6 1-butyl-3-methyl-1,2,3-triazolium trifluoroacetate [bm3tri][TFA]

1-methyl-1-H-1,2,3-triazole (95+%, ArkPharm) was alkylated with 1-bromobutane to form 1-butyl-3-methyl-1,2,3-triazolium bromide. This was converted to 1-butyl-3-methyl-1,2,3-triazolium trifluoroacetate using the anion exchange and drying methods described above, yielding 76g. ^{1}H NMR (300 MHz, D_2O, δ): 0.94 (t, 3H, CH_3, J = 7.5), 1.36 (h, 2H, CH_2, *J* = 7.5 Hz, 2H), 1.98 (quint, 2H, CH_2, J = 7.6 Hz), 4.33 (s, 3H, CH_3), 4.64 (t, 2H, CH_2, J = 7.4 Hz), 8.49 (s, 1H), 8.53 (s, 1H); ^{13}C NMR (75 MHz, D_2O, δ): 12.47, 18.68, 30.55, 39.61, 53.48, 114.40 (COO^-), 118.26 (CF_3), 130.11, 131.07; ^{19}F NMR (282 MHz, D_2O, δ): −75.58 (CF_3 COO^-)

4.3.1.7 1-butyl-4-methyl-1,2,4-triazolium trifluoroacetate [bm4tri][TFA]

1,2,4-triazole (98%, Sigma Aldrich) was reacted with 1-bromobutante to form 1-bromo-1,2,4-triazole, which was then alkylated with methyl iodide to form 1-butyl-4-methyl-1,2,4-triazolium iodide. The iodide was replaced with trifluoroacetate and the resulting aqueous ionic liquid solution was then dried using the anion exchange column and drying methods described above, yielding 50g of 1-butyl-4-methyl-1,2,4-triazolium trifluoroacetate. ^{1}H NMR (300 MHz, D_2O, δ): 0.96 (t, 3H, CH_3, J = 7.3), 1.37 (h, 2H, CH_2, J = 7.6 Hz), 1.96 (quin, 2H, CH_2, J = 7.7 Hz, 2H), 4.01 (s, 1H), 4.45 (t, 2H, CH_2, J = 7.1 Hz), 4.79 (s, 1H), 8.83 (s, 1H), 9.77 (s, 1H); ^{13}C NMR (75 MHz, D_2O, δ): 12.53, 18.67, 30.01, 33.89, 52.17, 114.42 (COO^-), 118.29 (CF_3) 142.32, 145.33; ^{19}F NMR (282 MHz, D_2O, δ): −75.55 (CF_3 COO^-).

4.3.1.8 Additional purification procedures

The anion exchange resin was converted to its hydroxide form prior to each synthesis procedure by running a solution of 1 mol/L aqueous sodium hydroxide down the column. This was done until the eluent tested negative for halide ion by taking approximately 0.75 mL of eluent, adding 10 drops of concentrated

nitric acid, followed by 0.75 mL of 1 mol/L silver nitrate solution. When the eluent remained perfectly clear for at least 30 minutes (no precipitate or turbidity) test was considered negative and the solution qualitatively halide-free. Typically, this required about 6 flushes of 4 liters each of 1 mol/L sodium hydroxide to remove all the halide ion from the column. Once this was achieved, the column was then flushed with distilled water until all of the excess hydroxide was removed, as determined using pH paper. The column was then ready for use to convert the IL-halide precursors to their corresponding hydroxides.

While the other ILs were originally of a clear to light yellow hue in coloration, [bmpz][TFA] and [bm4tri][TFA] appeared to be a darker yellow color. Due to the suspicion of impurities or unreacted base materials, these ILs were further cleaned with activated charcoal (Sigma Aldrich). The activated charcoal was cleaned of impurities by boiling in 1 M nitric acid for 8 hours, then boiled in 3-4 fresh baths of ultrapure water with draining in between each bath. Roughly 7g of cleaned activated charcoal was added to each original bottle of [bmpz][TFA] and [bm4tri][TFA] and the respective mixtures were heated to 60°C and stirred for approximately 24 hours. Afterwards, the charcoal was filtered out and both ILs appeared similar in color to the other ILs with clear to light yellow hues.

4.3.1.9 Sample Preparation

Immediately prior to and after finishing each measurement series, IL samples were further dried in two stages, different from the procedures already described. First, bulk water removal was accomplished with an oil-free, diaphragm vacuum pump (−30 inHg) with the IL sample in a 250 cm^3 side-arm Erlenmeyer flask, heated to 55°C for 24 hours. Next, the IL sample was transferred to a 22 cm^3 glass vial and left to dry in a vacuum chamber, held at < 10 mbar for two weeks. Immediately prior to removal of the sample, the vacuum chamber was back-filled with nitrogen (Airgas, 99.999%). Upon opening the vacuum chamber, the glass sample vial was sealed with a Teflon backed screw-cap and wrapped with wax paper.

The aqueous IL solutions were prepared sequentially for each series of measurements. Starting with the neat IL, water was added gravimetrically using a Cole Parmer Symmetry-224 balance, with a repeatability of $\pm 2 \times 10^{-4}$ g. The ultrapure water added to prepare each solution was deionized and polished

water from a US Filter PureLab Plus, measured to be 18.2 MΩ-cm resistance. Solutions were stirred with a glass rod following water addition. After each measurement was made, the solution was returned to its sample vial for the measurement series and the residual solution lost between each measurement was quantified gravimetrically. Water was added to the solution for the next measurement such that the cumulative total of water in the sample reached the desired concentration, correcting for loss of sample due to residual liquid that remained in or on the measurement apparatus after each measurement. Additional ultrapure water was added to the already diluted solution for the next concentration. This process was repeated until the last measurement was made at the highest water concentration.

In between every measurement, the measurement apparatus was thoroughly rinsed with ultrapure water, then dried under a flow of nitrogen before being used for the next measurement. Each apparatus was dry (assessed gravimetrically) within 15 minutes and allowed to equilibrate with room temperature for another 15 minutes after drying. Between each measurement, the aqueous IL solution being studied was kept sealed in a screw-cap glass vial with a Teflon-backed cap to minimize exchange with the air, though the headspace in the vial was ambient air (10% RH, 12.2 psia). As per the analysis of other studies (Rodríguez & Brennecke, 2006), it is expected that experimental error is introduced in the water content of each sample through exchange with the air. At low water concentrations in the sample, it would be expected that the sample would uptake water, and at high water concentrations, the sample would be expected to desorb water. No attempt was made to quantify this error, but the time in which samples were open to the air (i.e. not capped) was minimized.

4.3.2 Experimental Methods

4.3.2.1 Density Measurements

Experimental densities were measured gravimetrically at atmospheric pressure (12.2 psia in Boulder, CO, USA) using a calibrated, 5 cm^3 pycnometer (Blaubrand). The calibrated volume of the pycnometer is 5.0462 cm^3 ± 0.0100 cm^3. Ambient temperature was monitored with a temperature and humidity meter (ThermoPro) in a temperature-controlled room. At each measurement, the sample equilibrated with the

ambient temperature of the room over 30 minutes. Room temperature was maintained at 295.4 ± 1.0 K (more exact temperature and deviations reported with each measurement). The uncertainty of the density values is estimated to be ± 0.002 g•cm^{-3}, and the uncertainty of the excess molar volume values is estimated to be ± 0.01 cm^{3}•mol^{-1}, both derived on the basis of the accuracy of the scale and the pycnometer. The uncertainty of density measurements of the comparative study, (Rodríguez & Brennecke, 2006), is estimated to be better than ± 5 × 10^{-5} g•cm^{-3}

4.3.2.2 Conductivity Measurements

Experimental conductivity measurements were made using an Omega Portable Conductivity Meter equipped with a two-platinum-electrode glass dip cell with selectable ranges of 0-200 µS•cm^{-1} (0.001), 0-2 mS•cm^{-1} (0.01), 0-20 mS•cm^{-1} (0.1), 0-200 mS•cm^{-1} (1). The resolution of each range is listed in parentheses after the range, and the accuracy for each range is ± 0.1% of the reading. Conductivity measurements were made with the same samples used for density measurements, immediately before each density measurement. All measurements were stable within a few seconds of inserting the dip cell, but were watched for two minutes to ensure no change in the measurement value over time.

4.3.2.3 Viscosity Measurements

Experimental viscosities were measured using a Gilmont falling ball viscometer (GV-2300) with a range of 20–1000 cP and a manufacturer's nominal uncertainty of 1% of the reading. To confirm the repeatability of the measurements, viscosity was measured ten times for each concentration of IL-water mixture. The maximum recorded standard deviation was 2% of the recorded value (though most standard deviations were around 1% of the measured value, reported with viscosity data below). The nominal uncertainty of the viscosity values from reference data, (Rodríguez & Brennecke, 2006), is ± 2%, but uncertainties are estimated by the authors to be closer to ± 1 cP for values below 50 cP and ± 2 cP for values reported above 50 cP, due to sample water losses to evaporation at higher water content. No attempt was made to estimate actual uncertainty due to such water loss for this study due to the unavailability of equipment to determine absolute water content of the samples (i.e. Karl Fischer titration).

4.3.3 Results and Discussion

Experimental density ρ, excess molar volume V^E, and conductivity κ of each binary mixture of water (x_1) and six different ILs (x_2) across the entire composition range are reported in Table 10, and the experimental dynamic viscosity η and excess viscosity $\Delta\eta$ for the same are reported in Table 11. In order to validate the experimental approach, comparisons are made between data from (Rodríguez & Brennecke, 2006), (Lin, Soriano, Leron, & Li, 2011), and data collected in this study for the binary system of water and [emim][OTf]. These data are shown in Table 7,

Table 8, and Table 9, then compared in Figure 15, Figure 16, and Figure 17. Discrepancies between the data from this study and that from (Rodríguez & Brennecke, 2006) are due to the c.a. 7 K difference between measurement temperatures, initial water content of the IL sample, atmospheric pressure, and any absorbed or desorbed humidity between measurements. The differences between the data from this study and that from (Lin et al., 2011) are also likely due to the same reasons, but the temperature difference between the two data sets is only 2.2 K.

Table 7. Comparison of data for experimental density and excess molar volume of the binary mixture of water (x_1) and [emim][OTf] ($1-x_1$) between this study (left) and (Rodríguez & Brennecke, 2006) (right). Also presented is the conductivity κ of the same from this study.

x_1	ρ/g·cm^{-3}	V^E/cm^3·mol^{-1}	x_1	ρ/g·cm^{-3}	V^E/cm^3·mol^{-1}
(x_1) H_2O + (1 – x_1) [emim][OTf] at T = 295.4 K ± 0.2 K			*(x_1) H_2O + (1 – x_1) [emim][OTf] at T = 288.15 K ± 0.1 K*		
1.0000	0.9977*	0.0000	1.0000	0.99913	0.000
0.9900	1.0351	-0.0281	0.9924	1.02864	−0.010
0.9750	1.0801	-0.0410	0.9712	1.09364	−0.043
0.9500	1.1356	-0.0492	0.9353	1.16597	−0.065
0.8999	1.2055	-0.0515	0.8608	1.24716	−0.061
0.7995	1.2762	-0.0306	0.7825	1.29174	−0.037
0.7000	1.3112	0.0196	0.6157	1.33887	0.037
0.4997	1.3474	0.0719	0.4310	1.36387	0.120
0.3518	1.3619	0.0979	0.2295	1.37981	0.135
0.1481	1.3751	0.0618	0.0000	1.38360	0.000
0.0000	1.3820	0.0000			

*values provided as reference from (Haynes, 2014) and used in calculations of V^E

Table 8. Comparison of data for experimental viscosity, standard deviation thereof, and excess viscosity of the binary mixture of water (x_1) and [emim][OTf] (1-x_1) between this study (left) and (Rodríguez & Brennecke, 2006) (right).

x_1	η/mPa·s	σ/ mPa·s	Δη/mPa·s	x_1	η/mPa·s	Δη/mPa·s
(x_1) H_2O + (1 − x_1) [emim][OTf] at T = 295.4 K ± 0.2 K				*(x_1) H_2O + (1 − x_1) [emim][OTf] at T = 288.15 K ± 0.1 K*		
1.0000	0.95*	0.00	0.00	0	61	0
0.9467	2.79	0.27	-0.69	0.2286	32	-15
0.8958	3.54	0.49	-2.34	0.4324	20	-15
0.7999	5.42	0.57	-5.00	0.6159	13	-11
0.7009	7.53	3.59	-7.56	0.783	7	-7
0.5037	13.45	0.28	-10.97	0.9352	4	-1
0.3520	19.97	0.33	-11.61			
0.1525	32.50	0.43	-8.53			
0.0000	48.23	0.42	0.00			

*values provided as reference from (Korson, Drost-Hansen, & Millero, 1968), used in calculations of Δη.

Table 9. Comparison of data for experimental conductivity of the binary mixture of water (x_1) and [emim][OTf] (1-x_1) between this study (left) and (Lin et al., 2011) (right)

x_1	κ/mS·cm^{-1}	x_1	κ/mS·cm^{-1}
(x_1) H_2O + (1 − x_1) [emim][OTf] at T = 295.4 K ± 0.2 K		*(x_1) H_2O + (1 − x_1) [emim][OTf] at T = 293.2 K*	
0.9900	18.92	0.8	34.37
0.9750	28.8	0.6	23.47
0.9500	34.7	0.4	16.36
0.8999	36.4	0.2	11.65
0.7995	31.9		
0.7000	26.7		
0.4997	18.48		
0.3518	14.06		
0.1481	9.79		
0.0000	7.54		

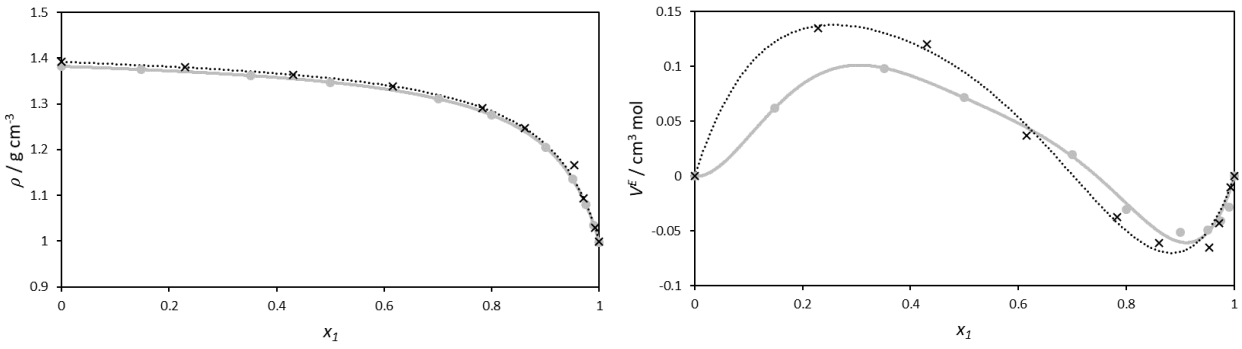

Figure 15. (left) Density ρ for the binary mixture of water (x_1) as a molar fraction and [emim][OTf] (1-x_1) and (right) excess molar volume V^E of the same mixture. (X), (…) = data from (Rodríguez & Brennecke, 2006); (●), (−) = data from this study.

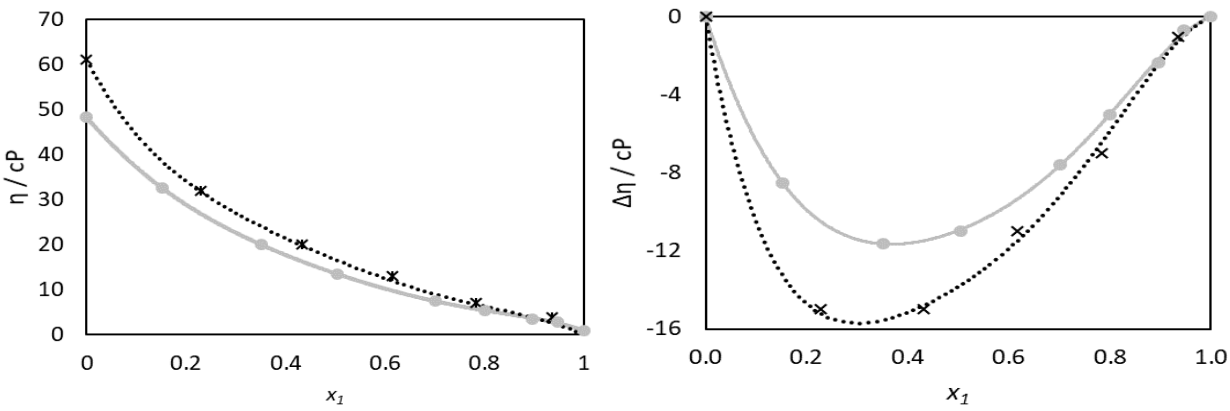

Figure 16. (left) Viscosity η for the binary mixture of water (x_1) as a molar fraction and [emim][OTf] (1-x_1) and (right) excess viscosity $\Delta\eta$ of the same mixture. (X), (…) = data from (Rodríguez & Brennecke, 2006); (●), (−) = data from this study.

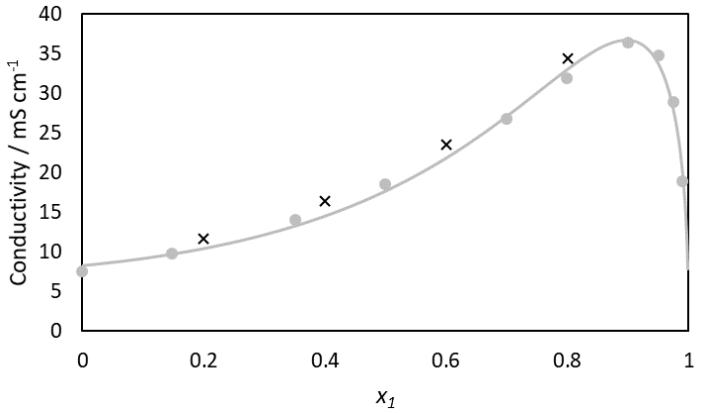

Figure 17. Conductivity κ for the binary mixture of water (x_1) as a molar fraction and [emim][OTf] (1-x_1). (X), (…) = data from (Lin et al., 2011); (●), (−) = data from this study.

Table 10. Density, excess molar volume, and conductivity reported for concentrations of H_2O (x_1) in each IL ($1–x_1$), including [bmpyrr][TFA], [bmpy][TFA], [bmpz][TFA], [bmim][TFA], [bm3tri][TFA], and [bm4tri][TFA].

x_1	ρ/g·cm^{-3}	V^E/cm^3·mol^{-1}	κ/mS·cm^{-1}
(x_1) H_2O + ($1 – x_1$) [bmpyrr][TFA] at T=296.2 K ± 0.2 K			
1.0000	0.9975*	0.0000	–
0.9901	1.0173	-0.0238	16.19
0.9750	1.0442	-0.1267	22.9
0.9499	1.0745	-0.2530	24.5
0.8999	1.1089	-0.4169	21.6
0.8001	1.1380	-0.5335	14.54
0.6998	1.1517	-0.6181	10.41
0.4993	1.1630	-0.5684	6.33
0.3499	1.1667	-0.4491	4.80
0.1504	1.1691	-0.1629	3.44
0.0000	1.1706	0.0000	2.72
(x_1) H_2O + ($1–x_1$) [bmpz][TFA] at T=296.2 K ± 0.2 K			
1.0000	0.9975*	0.0000	–
0.9901	1.0233	-0.0196	21.2
0.9750	1.0577	-0.1265	30.4
0.9500	1.0956	-0.1979	32.1
0.8999	1.1418	-0.3199	28.1
0.7997	1.1846	-0.4116	19.32
0.6993	1.2044	-0.4344	13.20
0.4993	1.2231	-0.3745	6.54
0.3535	1.2302	-0.3177	4.21
0.1488	1.2356	-0.1043	2.36
0.0000	1.2385	0.0000	1.510
(x_1) H_2O + ($1–x_1$) [bm3tri][TFA] at T=294.7 K ± 0.2 K			
1.0000	0.9979*	0.0000	–
0.9900	1.0257	-0.0526	20.1
0.9750	1.0608	-0.1679	30.5
0.9500	1.1003	-0.2682	32.9
0.8998	1.1472	-0.4003	30.5
0.7999	1.1895	-0.4723	22.2
0.7000	1.2096	-0.4904	15.91
0.5005	1.2282	-0.4122	8.32
0.3526	1.2350	-0.2924	5.51
0.1489	1.2409	-0.1335	3.33
0.0000	1.2437	0.0000	2.16

x_1	ρ/g·cm^{-3}	V^E/cm^3·mol^{-1}	κ/mS·cm^{-1}
(x_1) H_2O + ($1–x_1$) [bmpy][TFA] at T=295.0 K ± 0.2 K			
1.0000	0.9979*	0.0000	–
0.9901	1.0222	-0.0432	20.3
0.9750	1.0534	-0.1564	27.6
0.9499	1.0886	-0.2895	27.1
0.8999	1.1282	-0.4496	22.9
0.8000	1.1640	-0.6430	15.37
0.6996	1.1788	-0.6650	10.34
0.5005	1.1930	-0.6852	5.58
0.3484	1.1971	-0.5031	3.81
0.1510	1.1996	-0.1495	2.57
0.0000	1.2016	0.0000	2.00
(x_1) H_2O + ($1–x_1$) [bmim][TFA] at T=294.6 K ± 0.2 K			
1.0000	0.9979*	0.0000	–
0.9900	1.0212	-0.0170	17.50
0.9753	1.0524	-0.1305	25.3
0.9500	1.0881	-0.2329	28.1
0.8999	1.1287	-0.3376	26.3
0.7956	1.1690	-0.5198	19.00
0.6999	1.1881	-0.7403	13.80
0.5472	1.2006	-0.7373	8.99
0.3496	1.2084	-0.6402	5.49
0.1490	1.2114	-0.3133	3.73
0.0000	1.2125	0.0000	2.77
(x_1) H_2O + ($1–x_1$) [bm4tri][TFA] at T=295.7 K ± 0.2 K			
1.0000	0.9976*	0.0000	–
0.9900	1.0273	-0.0679	23.6
0.9750	1.0647	-0.2045	34
0.9500	1.1075	-0.3488	35.7
0.9000	1.1569	-0.5069	31.4
0.8000	1.2005	-0.5712	21.9
0.6990	1.2208	-0.5449	14.51
0.5019	1.2390	-0.3651	7.16
0.3517	1.2464	-0.2340	4.49
0.1510	1.2530	-0.1015	2.67
0.0000	1.2563	0.0000	1.699

*values provided as reference from (Haynes, 2014) and used in calculations of V^E

Table 11. Viscosity and excess viscosity reported for concentrations of H_2O (x_1) in each IL (1–x_1), including [bmpyrr][TFA], [bmpy][TFA], [bmpz][TFA], [bmim][TFA], [bm3tri][TFA], and [bm4tri][TFA].

x_1	η/mPa·s	σ/ mPa·s	Δη/mPa·s
(x_1) H_2O + (1–x_1) [bmpyrr][TFA] at T=295.5 K ± 0.1 K			
1.0000	0.95*	-	0.00
0.9500	3.53	0.06	-1.92
0.9000	5.86	0.06	-4.09
0.8003	13.18	0.09	-5.74
0.6992	20.59	0.20	-7.43
0.5002	37.66	0.37	-8.28
0.3498	52.02	0.25	-7.46
0.1490	74.00	0.45	-3.55
0.0000	90.96	0.32	0.00
(x_1) H_2O + (1–x_1) [bmpz][TFA] at T=296.3 K ± 0.2 K			
1.0000	0.93*	-	0.00
0.9500	3.22	0.05	-4.73
0.9000	4.61	0.06	-10.37
0.8009	10.37	0.09	-18.51
0.6997	16.87	0.21	-26.23
0.4988	32.89	0.27	-38.41
0.3529	52.11	0.24	-39.68
0.1505	93.74	0.46	-26.46
0.0000	141.34	0.37	0.00
(x_1) H_2O + (1–x_1) [bm3tri][TFA] at T=295.2 K ± 0.1 K			
1.0000	0.95*	-	0.00
0.9500	3.07	0.06	-1.81
0.9000	4.37	0.03	-4.44
0.8001	8.06	0.06	-8.59
0.6994	12.91	0.10	-11.64
0.4991	25.22	0.27	-15.05
0.3504	36.94	0.16	-15.01
0.1533	57.38	0.69	-10.04
0.0000	79.46	0.23	0.00

x_1	η/mPa·s	σ/ mPa·s	Δη/mPa·s
(x_1) H_2O + (1–x_1) [bmpy][TFA] at T=295.1 K ± 0.2 K			
1.0000	0.97*	-	0.00
0.9501	3.66	0.27	-1.88
0.9000	5.93	0.30	-4.21
0.8040	11.99	0.34	-6.95
0.7005	19.37	0.22	-9.06
0.4995	37.86	0.18	-9.00
0.3478	54.84	0.31	-5.92
0.1533	77.90	0.37	-2.37
0.0000	92.66	0.41	0.00
(x_1) H_2O + (1–x_1) [bmim][TFA] at T = 296.0 K ± 0.2 K			
1.0000	0.94*	-	0.00
0.9500	3.17	0.08	-1.56
0.9000	4.78	0.08	-3.74
0.8000	9.29	0.09	-6.81
0.7011	14.74	0.22	-8.87
0.5031	27.64	0.21	-10.98
0.3503	41.82	0.37	-8.39
0.1495	60.93	0.40	-4.50
0.0000	76.77	0.31	0.00
(x_1) H_2O + (1–x_1) [bm4tri][TFA] at T=296.2 K ± 0.1 K			
1.0000	0.93*	-	0.00
0.9500	3.08	0.04	-2.78
0.9000	4.47	0.06	-6.32
0.8002	8.75	0.07	-11.85
0.6998	13.95	0.16	-16.55
0.4978	27.33	0.25	-23.06
0.3495	43.10	0.23	-21.89
0.1484	72.85	0.27	-11.95
0.0000	99.41	0.33	0.00

*values provided as reference from (Korson et al., 1968), used in calculations of Δη.

4.3.3.1 *Effect of Composition on Density*

Experimental density ρ is plotted against molar fraction of water x_1 for each binary mixture of water and six different ILs in Figure 18, along with the corresponding excess molar volume V^E for each binary mixture. The excess molar volume is calculated by Equation 20.

$$V^E = \frac{x_1 M_1 + x_2 M_2}{\rho_{1,2}} - \frac{x_1 M_1}{\rho_1} - \frac{x_2 M_2}{\rho_2} \quad (20)$$

where x_1 is the molar fraction of water, x_2 (or $1-x_1$) is the molar fraction of the IL, M_1 is the molar mass of water, M_2 is the molar mass of the IL, ρ_1 is the density of pure water, ρ_2 is the density of the pure IL, $\rho_{1,2}$ is the density of the mixture of water and the IL. The data points represent actual measurements and the curves in both panels of Figure 18 are fits derived from the fourth order Redlich-Kister (RK) fit to V^E, calculated using Equation 21, where $A_{0...4}$ are the RK fitting coefficients.

$$V^E = x_1 x_2 \{A_0 + A_1(1-2x_1) + A_2(1-2x_1)^2 + A_3(1-2x_1)^3 + A_4(1-2x_1)^4\} \quad (21)$$

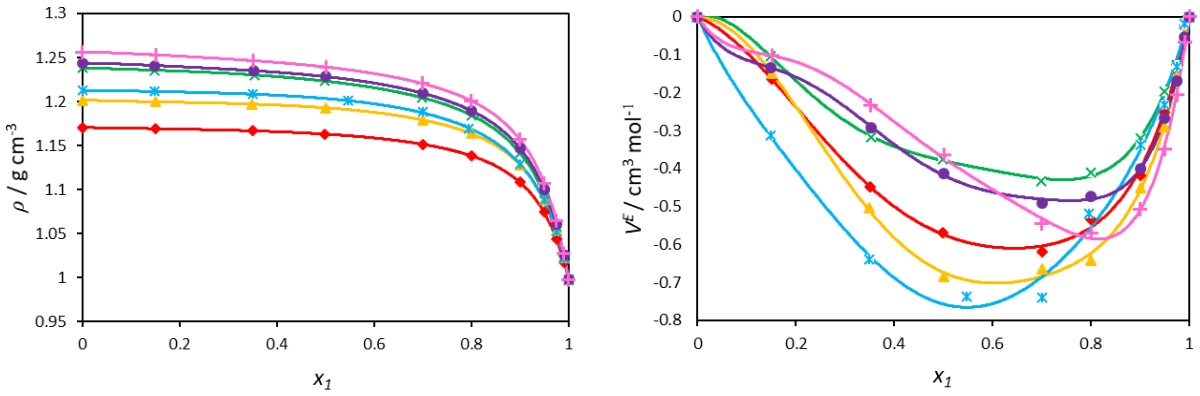

Figure 18. (left) Density ρ for the binary mixture of water (x_1) as a molar fraction and ($1-x_1$) of each of the following: (◆) [bmpyrr][TFA], (▲) [bmpy][TFA], (✕) [bmpz][TFA], (✱) [bmim][TFA], (●) [bm3tri][TFA], and (✚) [bm4tri][TFA], and (right) excess molar volume V^E of the same mixtures. Solid curves of the corresponding colors are fit to the data for each mixture from RK fitting coefficients, calculated from V^E.

The anion of the IL has been observed to have the strongest influence on the interactions of an IL with water (i.e. whether or not IL is miscible with water), while the length of alkyl chains on the cation appears to have a secondary effect (Seddon et al., 2000). Because all the ILs studied here have the trifluoroacetate anion (except for [emim][OTf] and cation alkyl chains of similar lengths, it is expected that each IL−water

system will have a similar excess molar volume. Indeed, in Figure 18, each of the solutions exhibit negative deviations from ideality, i.e. volume contractions, with a similar order of magnitude, confirming the stronger interaction and the complete miscibility of these ILs with water.

4.3.3.2 Effect of Composition on Viscosity

Experimental viscosity η and excess viscosity $\Delta\eta$ for each binary mixture of water and IL are plotted against molar fraction of water in Figure 19. Excess viscosity was calculated using Equation 22, where $\eta_{1,2}$ is the viscosity of the mixture, η_1 is the viscosity of pure water, and η_2 is the viscosity of the pure IL.

$$\Delta\eta = \eta_{1,2} - x_1\eta_1 - x_2\eta_2 \tag{22}$$

The data points represent actual measurements and the curves in both panels of Figure 19 are fits derived from the fourth order Redlich-Kister fit to $\Delta\eta$, calculated using Equation 23, where $A_{0\ldots4}$ are the RK fitting coefficients. As can be seen in Figure 19 and in the table of fitting coefficients in Appendix B, a fourth-order RK polynomial provides a reasonably good fit.

$$\Delta\eta = x_1x_2\{A_0 + A_1(1-2x_1) + A_2(1-2x_1)^2 + A_3(1-2x_1)^3 + A_4(1-2x_1)^4\} \tag{23}$$

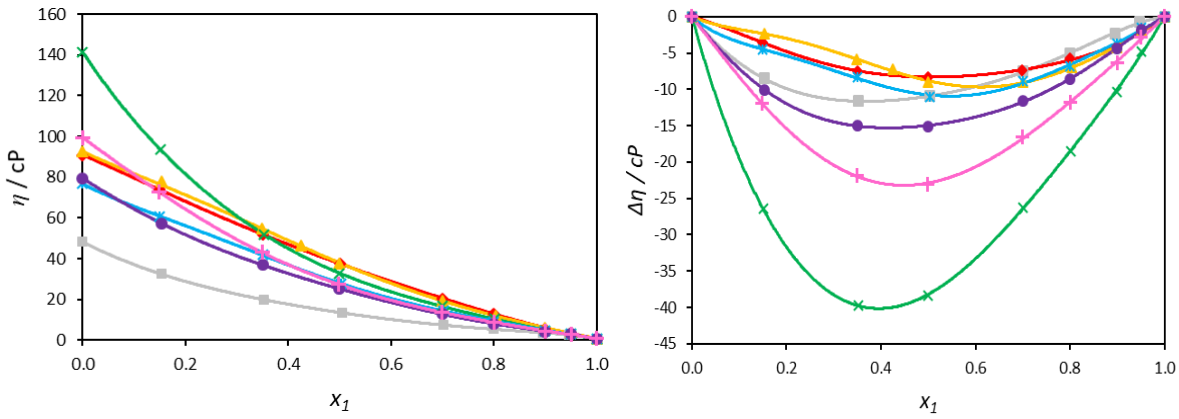

Figure 19. (left) Viscosity η for the binary mixture of water (x_1) as a molar fraction and (1-x_1) of each of the following: (◆) [bmpyrr][TFA], (▲) [bmpy][TFA], (×) [bmpz][TFA], (✳) [bmim][TFA], (●) [bm3tri][TFA], (✚) [bm4tri][TFA], and (■) [emim][OTf], and (right) excess viscosity Δη of the same mixtures. Solid curves of the corresponding colors are fit to the data for each mixture from RK fitting coefficients calculated from Δη.

All of the IL–water systems exhibit negative excess viscosity deviations, with [bmpz][TFA] solution showing the greatest decrease in viscosity, by a maximum factor of 2, compared with the other IL–water systems which have negative excess viscosity deviations in a smaller range. Even minor water additions to the pure ILs reduce viscosity of the system significantly. It is important to keep in mind that even a 0.5 molar fraction of each constituent in the solution has only a minor amount of water present by weight fraction, due to the generally 20-times larger molecular weight of the ILs than water's molecular weight.

4.3.3.3 Effect of Composition on Conductivity

Experimental conductivity κ is plotted against water concentration as a molar fraction for each binary mixture of water and IL in Figure 20. The data points represent actual measurements and the curves are simulated based on the coefficients derived from the data using the Casteel-Amis fit, Equation 24, for conductivity of a binary mixture.

$$\kappa = \kappa_{max}\left(\frac{x_2}{x_{2,max}}\right)^a \exp\left\{b(x_2 - x_{2,max})^2 - \frac{a}{x_{2,max}}(x_2 - x_{2,max})\right\} \quad (24)$$

Where κ_{max} is the maximum conductivity of the mixture, x_2 is the molar fraction of the IL, $x_{2,max}$ is the molar fraction of the IL at k_{max}, a and b are the fitting coefficients. Note that while Equation 24 uses the molar fraction of the IL, the fit of conductivity is plotted against the molar fraction of water in Figure 20 to maintain consistency across all plots.

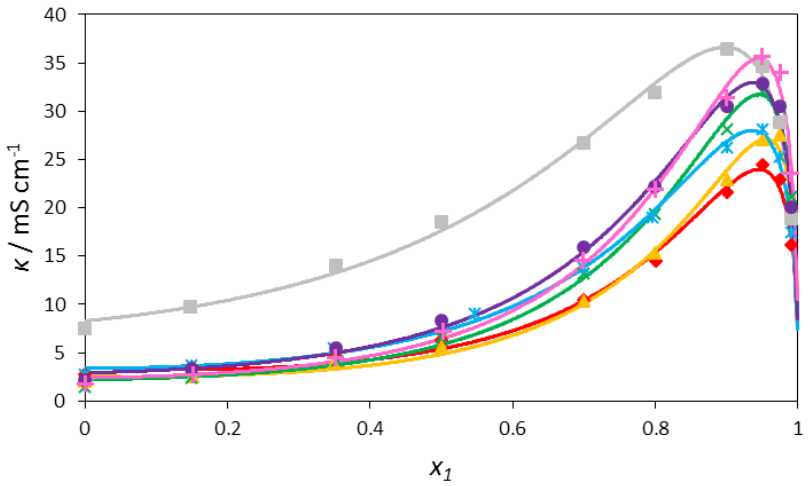

Figure 20. Conductivity κ for the binary mixture of water (x_1) as a molar fraction and ($1-x_1$) of each of the following: (◆) [bmpyrr][TFA], (▲) [bmpy][TFA], (✕) [bmpz][TFA], (✳) [bmim][TFA], (●) [bm3tri][TFA], (✚) [bm4tri][TFA], (■) [emim][OTf]. Solid curves of the corresponding colors are fit to the data for each mixture from Casteel-Amis fitting coefficients calculated from κ.

Conductivity for each IL−water system reaches a maximum in the range of 90−95 mol% water concentration (or 10−5 mol% IL concentration). Other than temperature, which was relatively constant throughout each measurement series and within two degrees Celsius between each IL−water system for conductivity measurements, the prime factors affecting the conductivity of each solution are the viscosity and the availability of charge carriers (electrolyte, i.e. IL). At lower water contents, the cation−anion associative interactions are stronger, keeping them from contributing to the ion mobility of the system. This effect is reduced as increased water content decreases the association of cations and anions, allowing greater ion mobility, to the inflection point where there are an insufficient number of charge carriers to counteract the resistive nature of ultrapure water (Cao et al., 2015). Similar to other studies of the conductivity of aqueous IL solutions, there appears to be a water-rich and a salt-rich region to the binary mixture conductivity curve (W. Liu, Cheng, Zhang, Wang, & Yu, 2008).

4.4 Summary

Each selected IL was either synthesized or procured, and further purified when necessary. The density, viscosity, and ionic conductivity were measured for each pure IL and the binary mixture of each IL with water over the entire composition range at a single temperature and pressure. From these measurements,

secondary correlations were made (excess molar volume and excess viscosity) to further understand the solutions and to empirically fit the data for accurate determination of the properties at non-measured intermediate values. A primary correlation was also made for conductivity with an empirical fitting equation so that it could be calculated for each IL-water solution at non-measured intermediate values. These correlations can help inform engineering design and process control, can help other researches to understand how different cations and anions contribute to the properties of ILs and aqueous IL solutions, and provide value in understanding the contribution of the ILs to electrochemical CO_2 reduction.

4.5 Related Presentations and Publications:

Holquist, J. B., Paley, M. S., and Klaus, D. M. (20XX). Density, Viscosity, and Conductivity of Seven Binary Mixtures of N-Heterocycle Cation-Varied Ionic Liquids and Water. [Working Title – In Preparation]

Holquist, J. B., and Klaus, D.M. (20XX). Experimental Evaluation of Trifluoroacetate Ionic Liquids with 7 Varied N-Heterocycle Cations for Electrochemical Reduction of Carbon Dioxide in Aqueous Solutions at Silver Electrodes. [In prep – Working Title].

Chapter 5 – Ionic Liquid Performance for Electrochemical CO_2 Reduction

5.1 Introduction

The first study to experimentally observe the co-catalytic effect of ILs for CO_2 reduction to CO was published in 2011 by (Brian A Rosen et al., 2011). Since then, following studies have explored IL-promoted CO_2 reduction with variations in IL cation, IL anion, cathode catalyst material and structure, water concentration in the IL, and added supporting electrolytes. While the catalyst material and morphology have the most effect on the rate and product selectivity of the electrolysis reaction, the parameters with the largest unexplored design space are the IL cation and anion, and of those, variation of the anion has been the focus of more study than the cation. This is due in large part to the observation that the anion has the most influence over the CO_2 solubility in the IL (Anthony et al., 2005). While solution-based CO_2 electrolysis is generally limited by sluggish kinetics, electrolysis with silver (and some other metals, see (Hori, 2008)) cathodes improve the kinetics of CO_2 reduction to the point where the reaction becomes diffusion limited in H-cells. Recalling the discussion from Chapter 4, by finding ILs with anions that improve the CO_2 solubility and diffusion coefficient while maintaining CO_2 in an active form, the diffusion limited response can be reduced to improve the rate of the reduction reaction. (Tanner et al., 2016) also suggest that local solvent structure at the electrode interface may also be a factor in the IL's effect on CO_2 reduction. On the other hand, the IL cation has been proposed to affect the coordination of the CO_2 molecule with the catalyst surface, to stabilize the high activation energy reaction intermediate ($CO_2^{\bullet-}$), or to affect the access of CO_2 to the cathode through the double layer via desorption from the electrode of the IL cation. It has been demonstrated that the selection of IL cation can affect the current density, overpotential, and product selectivity of the CO_2 reduction reaction in aqueous solution at silver and other electrodes, but the probing of different IL cation structures has been limited.

In this chapter, a range of IL cation structures are investigated for their performance in aqueous solution to electrochemically reduce CO_2 at a silver macroelectrode. Silver is chosen as the cathode material due to its proven selectivity and catalytic effect for CO production from CO_2 reduction, as well as its lower

cost than gold (another good CO_2 to CO catalyst material). The ILs being studied and justification for their selection is described in Chapter 4, along with their thermophysical properties in aqueous solutions. Electrochemical experiments in this chapter are conducted in a membrane-separated glass H-cell. Cyclic voltammetry is conducted to probe the response of reducing potentials on the IL-water solution with only argon in the cell, and then again with only CO_2 in the cell to compare the response. Constant potential electrolysis is conducted over 30 minutes at parametrically varied potentials where CO_2 reduction appears to occur in order to analyze the gaseous products of the reaction.

5.2 Experimental Methods and H-Cell Apparatus

5.2.1 Materials

The ionic liquids used in these experiments are [emim][OTf], [bmpyrr][TFA], [bmpy][TFA], [bmim][TFA], [bmpz][TFA], [bm3tri][TFA], and [bm4tri][TFA]. The synthesis and purification procedures for each of the ILs (or the procurement information) can be found in Chapter 4. All ILs were degassed in a vacuum filter flask at -30 inHg and a minimum of 50°C for 24 hours, then kept under 10 mbar vacuum in a chamber for a minimum of two weeks. Before removing the IL samples from the vacuum chamber, the chamber was back-filled with UHP N_2 gas (99.999%, Airgas). Samples were kept capped and had a secondary wax seal to prevent contact with air prior to testing. All water used was ultrapure water (18.2 MΩ-cm) produced from a USFilter PureLab PLUS. A solution of 0.1 M H_2SO_4 was prepared from concentrated sulfuric acid (99%, Sigma Aldrich). Research grade argon (99.999%, Airgas) and CO_2 (99.999%, Airgas) were used for "blank" and analyte-saturated tests, respectively. Nafion® 212 (2 mil. Thick, Fuel Cell Store) was cut to a square to cover the glass H-cell compartment interface, then soaked in ultrapure water for 24 hours prior to being used in an experiment. A solution of 1 M HCl was prepared from concentrated hydrochloric acid (99% Sigma Aldrich) diluted with ultrapure water. Silver foil (0.28 mm thick, 99.9%, Sigma Aldrich) and silver wire (0.5 mm diameter, 99.9%, Sigma Aldrich) were used for the working and reference electrodes as described below. Platinum wire mesh (85 mesh, 99.9% Alfa Aesar) and platinum wire (0.5 mm, 99.9%, Sigma Aldrich) were used for the counter electrode.

5.2.2 Electrochemical Apparatus

Electrochemical experiments (cyclic voltammetry and constant potential electrolysis) were performed in a custom split-compartment glass cell using an EZStatPro potentiostat (NuVant). The working electrode was a 0.5 cm x 0.5 cm x 0.28 mm thick silver sheet hooked and wrapped once on a silver wire through 2 small holes drilled into the corners of the silver sheet. Approximately 3 cm of each silver wire attachment was submerged in the solution during electrolysis, making the approximate active area of the working electrode 1.03 cm^2. The silver wire was passed through a glass tube and sealed with Hysol-1C epoxy (3M) at the end away from the solution (such that no solution contacted the epoxy). The counter electrode was a 3-cm x 2-cm platinum mesh wound into a coil, hooked and pressed onto a platinum wire. The reference electrode was a silver wire coated with AgCl by electrodeposition, described below. Gas was sparged into the cell with a glass tube with a coarse glass fritted outlet (Prism Glass Products). For cyclic voltammograms (CVs), prior to the blank measurements, Ar was sparged into the cell for 30 minutes to make sure the solution was free of CO_2, and for the CO_2 voltammograms, CO_2 was sparged into the cell for 15 minutes before each measurement to ensure saturation of the electrolyte. For constant potential electrolysis (CPE), CO_2 was sparged into the cell at a rate of 75 sccm for the duration of the experiment (30 minutes). Flow rate was controlled by an Alicat MCE mass flow controller and the mass flow was measured with an Alicat Whisper Series mass flow meter just upstream of a non-dispersive infrared (NDIR) CO analyzer (California Analytical Instruments/Fuji Electric Instrumentation, ZRE model). Both Alicat units recorded temperature and pressure of the gas flow. A Drierite® column was in-line upstream of the mass flow meter to remove humidity from the gas stream before allowing the gas through the NDIR analyzer. A quadrupole mass spectrometer (MKS Cirrus) was continuously sampling from a gas sample flask in-line, downstream of the NDIR analyzer, in order to detect H_2 at mass-to-charge ratio $m/z=2$. A detailed schematic of the gas handling and analysis system is presented in Figure 35 of Chapter 6.

Figure 21 shows a picture and a schematic of the small volume glass cell that was custom fabricated for these experiments. Ace Glass #7 fittings were used to seal the gas bubbler, gas outlet connection,

working electrode, and reference electrode connected to the cathode compartment of the cell, while the anode compartment was left open to vent to atmosphere. To make the catholyte solutions, ultrapure water was added to the dried ILs on a mass basis until the desired molar fraction of water was achieved. The anolyte was 0.1 M H_2SO_4 for all experiments. A Nafion® 212 membrane was placed in between the two compartments to keep the electrolyte solutions separate, sealed by two Viton® O-rings and a standard clamp.

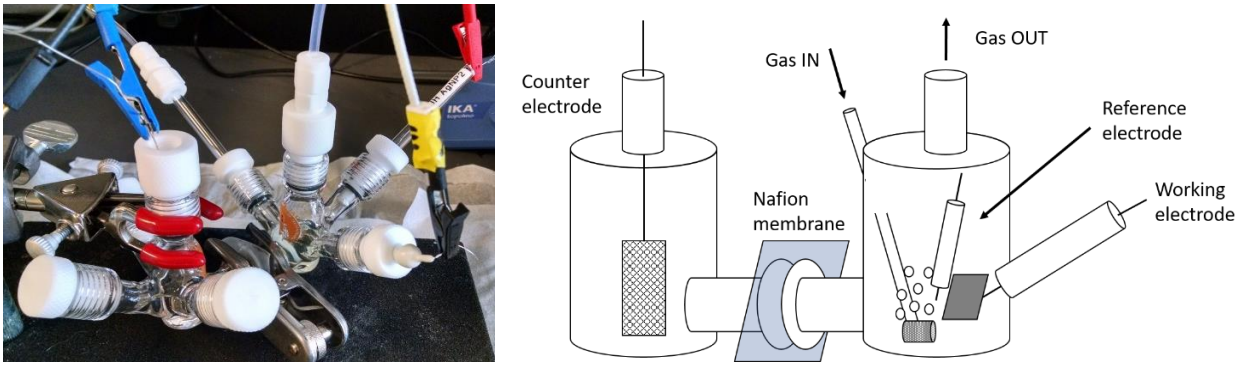

Figure 21. (left) A picture of the H-cell (right) A simplified schematic of the H-cell

5.2.3 Reference electrode preparation

To prepare the reference electrode, a silver wire was dipped in 1 M HCl, connected as the working electrode, and a constant current of 10 mA was applied for 60 seconds, followed by a current of −5 mA for 3 seconds (counter electrode and reference electrode were both platinum). This constant current process was repeated 5 times until a uniform dark purple-to-black color coated the wire's surface. On the last cycle, the reductive current was omitted. The AgCl electrodeposited wire was supported in an open-ended glass tube (protruding into the cell) and sealed on the back side with epoxy in a similar manner to the working electrode. A new reference electrode was prepared for each experiment series with each different IL, totaling 7 reference electrodes. Each was checked against a lab master (Ag/AgCl reference electrode in a glass housing, filled with 4 M KCl solution with a fritted glass tip) in 4 M KCl solution immediately prior to and following the experiment series. Prior to use in CV, each electrodeposited AgCl wire reference electrode was −2.4 mV vs. the lab master (standard potential: $E^0_{Ag/AgCl(4\ M\ KCl)}$ = 0.197 V).

5.2.4 *Experimental Methods*

5.2.4.1 *Cyclic Voltammetry*

Cyclic voltammetry (CV) is a method where the working electrode potential is quickly (~10-1000 mV/s) cycled with the current across the working and counter electrodes measured. This method allows for a quick determination of the onset potential in a given cell design for CO_2 reduction, the potential at which diffusion limitations begin, the reversibility of the electrochemical reaction, and the scale of current response across a wide range of potentials under quiescent conditions. It is used to check for differences between electrolysis in an aqueous ionic liquid solution with an inert gas sparge (Ar or N_2) or a reactive gas sparge (100% CO_2).

For each IL-water solution, the catholyte was sparged with Argon for 30 minutes to ensure the first set of potential scans would be free of CO_2. Potential was cyclically scanned from the equilibrium potential with no current flowing to a potential within the electrochemical window of the IL vs. Ag/AgCl for 20 cycles to ensure stability of the scans. All reported scans are the last scan in a series of cycles. Afterwards, CO_2 was sparged through the catholyte for 15 minutes to saturate the solution. Due to the physical solubility of CO_2 in the solution, simple gravimetric experiments showed that even pure IL of each candidate IL would saturate with CO_2 after sparging with pure CO_2 for less than 5 minutes. Next, a series of potential scans at parametrically varied scan rates were performed to test scan rate dependence of the cyclic potential scans and elucidate the diffusion coefficient from experimentally determined CO_2 solubility in the ILs. In between each scan rate dependence test, CO_2 was sparged again for 15 minutes.

5.2.4.2 *Constant Potential Electrolysis*

Constant potential electrolysis (CPE) is a method of bulk electrolysis that will generate enough gaseous product over time to meet the detection limits of the NDIR CO gas detection equipment. Using a membrane separated cell, the gaseous products from the anode and cathode compartments are already separated upon generation, and the reduction products from the cathode are continuously sampled in the downstream flow.

CPE was conducted with each aqueous IL solution that had a CV warranting (details below) gaseous product analysis. For each of these series of tests, the potential was held constant for 30 minutes and gaseous product signal data was recorded, along with flow rate, pressure, and temperature. A waiting period after each potential test was imposed to ensure all products were removed from the gas handling plumbing and IL solution, such that gas product signal had reset back to the baseline. No attempt at liquid product analysis was made, but the water content of the IL prior to and after each experiment was assessed via conductivity to determine amount of water loss from the IL due to HER and water vapor removal from gas sparging.

This section compares the current response of the IL-water solutions with a silver working electrode to cyclically applied potential scans response. For IL-water solutions with a current response that indicates a reaction with CO_2 the solubility of CO_2 in the system was determined using a Randles-Sevcik analysis as detailed by (Reche et al., 2014) and assuming the diffusion coefficient of CO_2 where it was not already known from literature. Finally, for those same systems that have an increased current response in the presence of CO_2, gaseous products were analyzed by means of NDIR spectroscopy tuned for CO and CH_4.

It must be noted here that the measurements for CO concentration from the NDIR analyzer are likely underestimated in both this chapter and Chapter 6, due to the time delay for full-scale response from the NDIR analyzer, as shown in Figure 22.

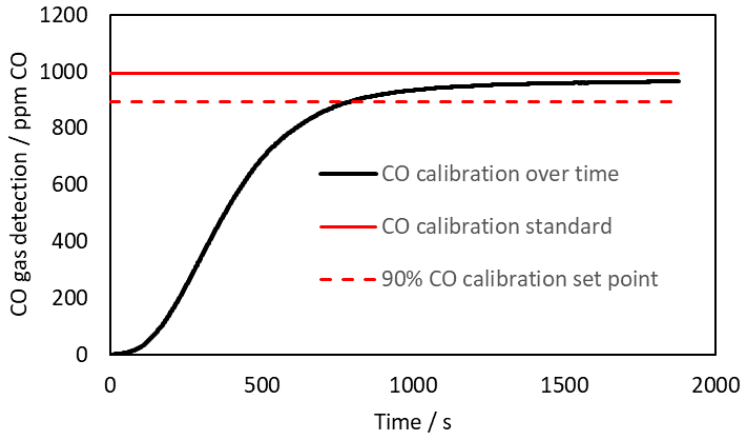

Figure 22. Response delay of NDIR gas analyzer to 75 sccm calibration gas flow (992.4 ppm CO)

The minimum flow rate for the NDIR analyzer is 300 sccm, but the maximum flow rate that has been used in this work is c.a. 86 sccm, causing the NDIR to respond much more slowly to achieving a full-scale response than its nominal rate of response. The time delay to 90% of full scale measurement with 75 sccm of calibration gas (Airgas, 992.4 ppm CO) flowing through the entire experimental apparatus is 787 s, and more than 2000 s for 100% full scale. Given that experiments reported herein are 600−1800 s in duration (10−30 min), a full-scale response is likely never recorded, and any reaction without 600 s of steady state operation likely does not come close to even the 90% full-scale measurement of CO concentration in the gas stream. However, the results can still be used qualitatively to compare each system of IL-water against one another with respect to CO_2 reduction performance.

5.3 Results and Discussion

To compare the response of each system to the presence and absence of CO_2, each system was scanned after being purged with Argon, and then again after being saturated with CO_2. In each plot shown in Figure 23, the grey line is the argon-purged system's response and the colored line is the same system's response while saturated with CO_2. A current response indicating CO_2 reduction can be clearly seen in Figure 23(a) [emim][OTf], Figure 23(b) [bmpyrr][TFA], and Figure 23(e) [bmim][TFA]. A weaker current response to the presence of CO_2 is seen in Figure 23(d) [bmpz][TFA] and Figure 23(f) [bm3tri][TFA], whereas there does not appear to be a significant current response to the presence of CO_2 for Figure 23(c) [bmpy][TFA] or Figure 23(g) [bm4tri][TFA].

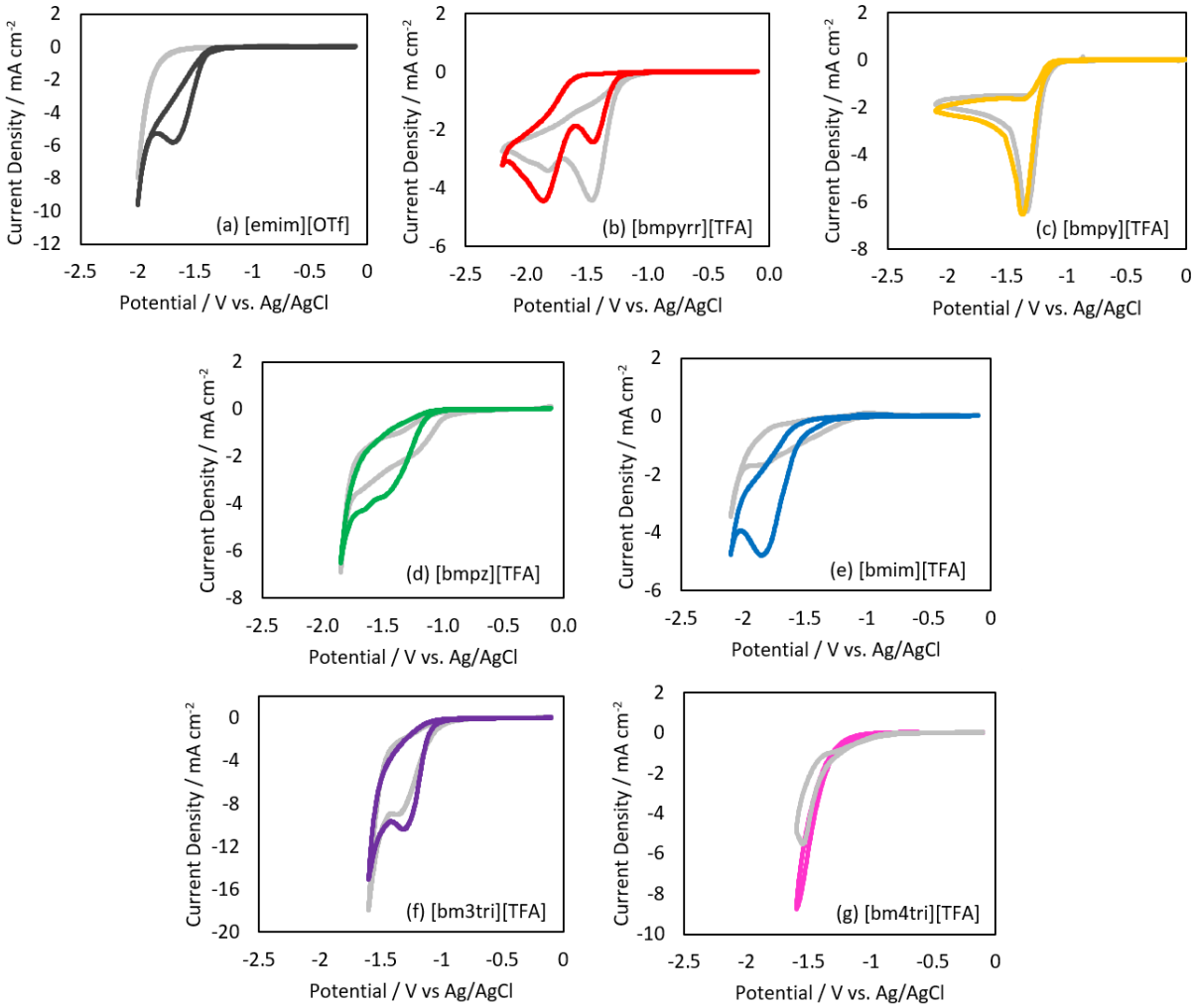

Figure 23. Cyclic voltammetry plots of each solution of 30mol% IL and water at a scan rate of 100 mV/s after the solution is sparged with Ar (grey lines) or CO_2 (colored lines); (a) black, [emim][OTf], (b) red, [bmpyrr][TFA], (c) yellow, [bmpy][TFA], (d) green, [bmpz][TFA], (e) blue, [bmim][TFA], (f) [bm3tri][TFA], (g) [bm4tri][TFA].

Constant potential electrolysis was conducted with the 30mol% aqueous solutions of [emim][OTf], [bmpyrr][TFA], [bmim][TFA], [bmpz][TFA], and [bm3tri][TFA] for 30 minutes at each potential that showed a current response to the presence CO_2 in the solution. The signal from the NDIR gas analyzer for CO production was multiplied with the steady state volumetric flow of total gas and integrated over total time analyzed, 20-30 minutes. The total charge passed during electrolysis was calculated by integrating the current over the duration of constant potential electrolysis. The resulting Faradaic efficiency for CO production was calculated by dividing the total number of moles CO measured by gas analysis by the total

charge passed during each constant potential electrolysis case, and the results are presented in Figure 24, except for those from [bm3tri][TFA], which, despite having a slightly increased current response under CO_2, did not exhibit any significant CO production. The results from CPE with [bm3tri][TFA] were therefore omitted from the following figures. The balance of Faradaic efficiency is assumed to be from the hydrogen evolution reaction, but because the maximum concentration of generated H_2 was below detection limits of the mass spectrometer, no significant data for H_2 production can be reported.

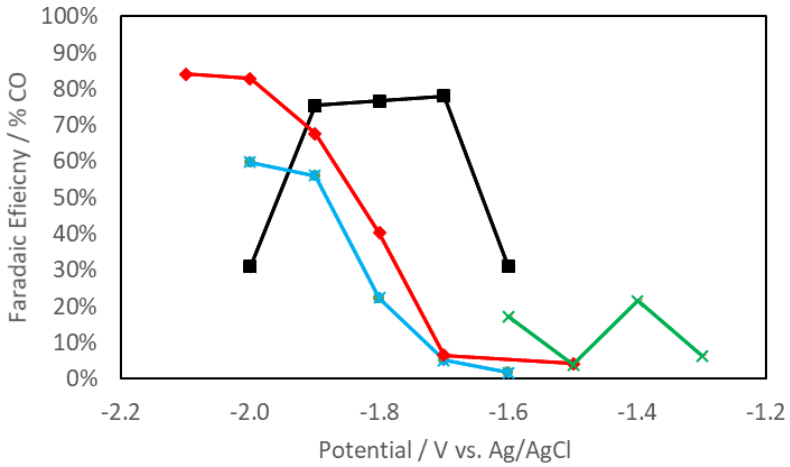

Figure 24. Faradaic efficiency for CO during CPE case of 30mol% IL in water, averaged over 30 minutes. Black squares: [emim][OTf], blue stars: [bmim][TFA], red diamonds: [bmpyrr][TFA], green X's: [bmpz][TFA].

The current from each CPE case was averaged over the 30-minute test and divided by the estimated geometric surface area of the bulk silver working electrode (1.1 cm^2) to determine the average current density of each case. The Faradaic current density for CO was calculated by multiplying this current density with the Faradaic efficiency for CO from that case, the result of which is presented in Figure 25. As mentioned in the Experimental Methods section of this chapter, these Faradaic efficiencies, and thus Faradaic current densities, are likely below the true values due to the NDIR analyzer underreporting the amount of CO actually generated due to the time delay for it to achieve a full-scale reading of the CO concentration.

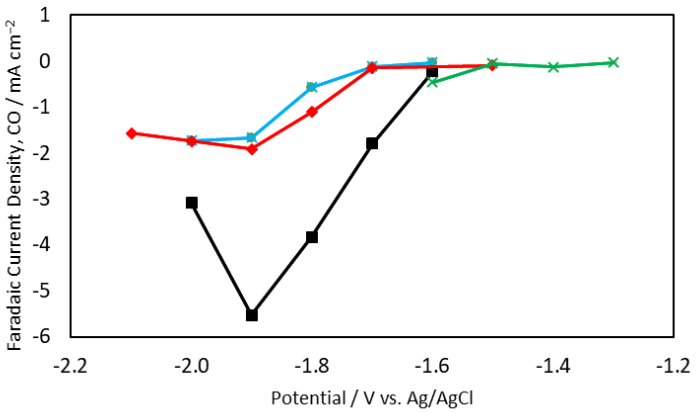

Figure 25. Faradaic current density for CO for the 30mol% aqueous solution of each IL from each CPE case. Black squares: [emim][OTf], blue stars: [bmim][TFA], red diamonds: [bmpyrr][TFA], green X's: [bmpz][TFA].

5.3.1 1-ethyl-3-methylimidazolium trifluoromethanesulfonate

From the cyclic voltammogram of the 30mol% solution of [emim][OTf] in water, Figure 23(a), no reaction occurs after a purge of argon (grey scan) until the onset of the hydrogen evolution reaction at -1.70 V vs. Ag/AgCl and the apparent onset of the cathodic potential limit of the electrolyte at c.a. −1.80 V vs. Ag/AgCl. After being purged with CO_2 for 10 minutes, the CV shows a clear reduction wave with an onset at -1.32 V vs. Ag/AgCl and a peak at -1.66 V vs. Ag/AgCl. While these potentials appear shifted positively compared with some literature results, the shape and current density are consistent (Neubauer, Krause, et al., 2016b). Comparing the blank scan with the CO_2-saturated scan, [emim][OTf] appears to strongly inhibit HER until significant overpotentials, unlike any of the other tested ILs. We speculate that this may be due to properties of the anion, discussed below.

By comparing Figure 23(a) with Figure 24, it can be seen that CO production reaches a peak Faradaic efficiency at the same potential as the peak current with significantly less CO produced at potentials ± 0.2 V. This behavior has also been seen literature with the same IL in an aqueous solution and with a silver working electrode, such as in the study by (Neubauer, Krause, Schmid, Guldi, & Schmid, 2016a)

5.3.2 *1-butyl-1-methylpyrrolidinium trifluoroacetate*

The CV of 30mol% [bmpyrr][TFA] in water, Figure 23(b), after argon purging shows a diffusion controlled current peak for HER at −1.46 V vs. Ag/AgCl, which in the presence of CO_2, decreases two-fold in amplitude, but remains a feature of the CV. The peak current of CO_2 reduction occurs at a more negative −1.85 V vs. Ag/AgCl. Interestingly, the presence of CO_2 appears to suppress HER even at potentials where CO_2 reduction is only barely occurring, despite the fact that CO_2 would lower the pH of the solution, increasing the hydrogen ion content, which would in turn be expected to boost HER rather than suppress it.

The IL [bmpyrr][TFA] also has a widest electrochemical window of those ILs in this study, and thus CO_2 reduction can be assessed at more negative potentials. Contrary to the behavior of the Faradaic efficiency for CO in [emim][OTf], the FE_{CO} from [bmpyrr][TFA] increases with increasing negative potential and approaches a maximum at the most negative working electrode potential tested. More negative potentials were not tested to keep from damaging the sample from electrochemical breakdown (onset c.a. 0.2 V more negative) that had been seen in other samples that were tested at more negative potentials. However, $j_{CO,bmpyrr}$ is 2-3 times lower in amplitude from that of $j_{CO,emim}$, showing that [bmpyrr][TFA] has less of a catalytic effect on CO_2 reduction than [emim][OTf]. This could be related to mass transport limitations of CO_2 in [bmpyrr][TFA], the diffusion coefficient of which appears to be at least one order of magnitude lower than compared with that of CO_2 in [emim][OTf]. Additionally, (Zhao et al., 2016) speculate that [bmpyrr] cations act to facilitate CO_2 reduction by a double layer effect, as opposed to a imidazolium cations co-catalyzing CO_2 reduction by a direct interaction with the CO_2 molecule itself.

5.3.3 *1-butyl-3-methylpyridinium trifluoroacetate*

The CV of 30mol% [bmpy][TFA] in water, Figure 23(c), appears unchanged from scans after argon sparging to scans following CO_2 sparging. No bubble evolution was observed on the silver cathode, leaving us to speculate that the reduction wave seen in both CVs is the reduction of the cation to its neutral form.

While it was originally expected that some reduced CO_2 product may be formed by electrolysis of CO_2 in [bmpy][TFA] due to reports from Bocarsly and co-workers detailing methanol production in aqueous pyridinium solutions at platinum electrode (Barton Cole et al., 2010), more recent studies have been published that were unable to replicate Bocarsly and coworker's results (Costentin, Canales, Haddou, & Saveant, 2013), (Lebegue, Agullo, & Belanger, 2018). Since then, methodological errors related to some experimental and computational studies of CO_2 electrolysis to methanol with pyridine and pyridine derivatives, including those by Bocarsly and co-workers, have been pointed out that highlight why CO_2 reduction products may not be expected and cannot be corroborated with experiments using more stringent and reported product analysis (Costentin, Saveant, & Tard, 2018). In the study by Lebegue et al., N-methylpyridinium iodide was studied in aqueous solution, with and without CO_2 present, with cyclic voltammetry and product analysis at Pt, Au, and glassy carbon electrode in an effort to discern the role of the electrode material. No CO_2 reduction products were observed in any of the cases. Due to the similarity of the cations between [bmpy][TFA] and N-methylpyridinium iodide, this result should also be expected in the case of using a silver electrode, which generally acts similarly to gold in catalyzing CO_2 to CO. Therefore, as is consistent with these more recent studies, no significant variation in current response was recorded in this study comparing the argon-purged [bmpy][TFA]-water system with the same CO_2-saturated system. Because of this, no further product analysis or scan rate dependence testing was performed with [bmpy][TFA].

5.3.4 1-butyl-2-methylpyrazolium trifluoroacetate

From the CV of 30mol% [bmpz][TFA] in water, a slightly more negative current can be observed in the presence of CO_2 with the solution purged by argon. However, there does not appear to be a similar peak for CO_2 reduction as seen in CV scans of [emim][OTf], [bmpyrr][TFA], or [bmim][TFA], nor a peak for HER, as appears in the scan for [bm3tri][TFA]. Because the CV scans with [bmpz][TFA] were inconclusive as to whether or not the IL was facilitating CO_2 reduction, CPE was conducted to more thoroughly investigate the system. With the CPE results, it is clear that a minor amount of CO is generated at fairly

positive potentials (c.a. −1.6 V vs. Ag/AgCl), but that the current density for the reaction is an order of magnitude lower than Faradaic current density for CO in the aqueous [emim][OTf] system.

5.3.5 1-butyl-3-methylimidazolium trifluoroacetate

The CV of 30mol% [bmim][TFA] in water appears similar to that of the CV with [emim][OTf], except that [bmim][TFA] does not entirely suppress HER at the potential of CO_2 reduction; however, it does appear to at least inhibit the more positive potential onset of HER. The peak ratio of CO produced by CO_2 reduction in [bmim][TFA] occurs at the most negative tested potential, but only reaches a maximum of c.a. 60% FE_{CO}. As with [bmpyrr][TFA], this sample was not tested at more negative potentials to protect it from electrochemical breakdown, onset of which appeared to occur in other samples at c.a. 0.2 V more negative. This result may allow comparison with other CO_2 electrolysis experiments in [bmim]-based ILs from literature to further discern anion influence on CO_2 reduction, although generally such studies have occurred in dry conditions. Regardless, ILs that can facilitate intermediate FE_{CO} values may prove useful in co-electrolysis systems to create syngas for such processes as Fischer-Tropsch synthesis or for carbon formation reactors useful to spacecraft environmental control and life support system loop closure.

5.3.6 1-butyl-3-methyl-1,2,3-triazolium trifluoroacetate

The aqueous solution of 30mol% [bm3tri][TFA] only appears to show a minor variation in CV scans with and without CO_2 present in solution, where a slightly more negative current is observed with CO_2 in solution. Gaseous product analysis during CV revealed that no detectable amounts of CO or CH_4 were generated at potentials along the reductive wave seen in the CV, and it is assumed that current either supported HER (though H_2 was below detection limits) or breakdown of the IL. Indeed, after CPE tests at the most negative potential (−1.6V vs. Ag/AgCl), the electrolyte darkened and produced a grey-white precipitate. It appears that, if [bm3tri][TFA] were capable of facilitating CO_2 reduction, such driving potentials necessary would be greater than the reductive breakdown limit of the IL.

5.3.7 *1-butyl-4-methyl-1,2,4-triazolium trifluoroacetate*

The CV of 30mol% [bm4tri][TFA] in water without CO_2 present does not appear to change upon introduction of CO_2. Similar to [bm3tri][TFA], it appears that the reductive limit of the IL is reached prior to the onset potential of any discernable CO_2 reduction. Constant potential electrolysis experiments were not carried out with [bm4tri][TFA] due to the lack of altered current response under CO_2-saturation and the obvious discoloration of the electrolyte after numerous CVs at the potentials shown in Figure 23(g).

5.3.8 *Scan Rate Dependence and CO_2 Solubility*

The solubility of CO_2 in a given solution can be accessed gravimetrically (i.e. by weighing a sample before and after saturation with CO_2) or electrochemically, by using the irreversible Randles-Sevcik equation (Equation 25), as demonstrated by (Reche et al., 2014; Tanner et al., 2016) when the diffusion coefficient is known and the plot of peak current to square root of the scan rate is linear (I_{pc} *vs.* $\sqrt{v}$). Alternatively, if the CO_2 solubility in a solution is already known, then the diffusion coefficient of CO_2 in the solution can be determined by using the same equation.

$$I_{pc} = 0.496nFSC^0\sqrt{\alpha}\sqrt{\frac{F}{RT}}\sqrt{v}\sqrt{D} \tag{25}$$

Where I_{pc} is the peak current, n is the number of electrons (in this case, a one electron reduction is the limiting step, so $n = 1$ is used, F is Faraday's constant ($F = 96{,}485\ C\ mol^{-1}$), S is the surface area of the electrode ($S = 1.1\ cm^2$), C^0 is the concentration of CO_2 in the bulk solution, α is the electron transfer coefficient (described in Equation 26), R is the ideal gas constant ($R = 8.314\ J\ mol^{-1}\ K^{-1}$), T is the temperature of the electrolyte, v is the scan rate in V s^{-1}, and D is the diffusion coefficient of CO_2.

$$\alpha = \frac{RT}{F}\left(\frac{1.85}{\Delta E_{pc}}\right) \tag{26}$$

Where ΔE_{pc} is the potential width of the peak current wave, determined as two times the difference between the potential at peak current and the potential at half of the peak current.

The saturated CO_2 solubility in 6 of the neat ILs was studied by directly bubbling pure CO_2 at 14.7 psia into a vial of each IL, fitted with a custom quick-disconnect apparatus with an outlet restriction, and weighing the sample at two-minute intervals until a steady-state mass of the vial was reached. Each neat IL sample was prepared via the two vacuum stages of drying water from the sample, as described in Chapter 4. The CO_2 solubility in each of the samples is summarized in various units in Table 12 and the mass of CO_2 in each sample (vial and bubbler mass subtracted) versus time is shown in Figure 26. Because the vial was sealed during the weighing of the sample while the headspace of the vial was filled with 100% CO_2, a buoyancy correction was made from a CO_2 atmosphere to an air atmosphere based on the headspace volume in the vial.

Table 12. Saturated CO_2 solubility at 14.7 psia and 20°C in 6 neat ILs

Units	[emim] [OTf]	[bmpyrr] [TFA]	[bmpy] [TFA]	[bmpz] [TFA]	[bmim] [TFA]	[bm3tri] [TFA]
g CO_2 / g IL	0.0032	0.0026	0.0032	0.0028	0.0033	0.0027
g CO_2 / mol IL	0.8269	0.6660	0.8468	0.7016	0.8253	0.6911
mol CO_2 / mol IL	0.0188	0.0151	0.0192	0.0159	0.0188	0.0157
x_{CO2}, mol CO_2 / (mol IL + mol CO_2)	0.0184	0.0149	0.0189	0.0157	0.0184	0.0155
Molar concentration CO_2 (M)	0.10	0.07	0.09	0.08	0.09	0.08
g CO_2 / mL IL	0.0044	0.0031	0.0039	0.0034	0.0040	0.0034

The same methods were used for each CO_2 solubility experiment, and the solubility of CO_2 in [emim][OTf] from this study (x_{CO2} = 0.0184) is similar to that presented by Reche et al. (x_{CO2} = 0.015(2)) at 25°C and 1 bar (14.7 psia). The value in the parentheses at the end of the molar fraction of CO_2 in solution from Reche et al. represents the standard deviation of the last digit. Morgan et al. report a solubility of CO_2 of 0.08 ± 0.01 M at 30°C and 101 kPa (14.7 psia), which is also below this study's estimate of 0.10 M at 20°C (Morgan, Ferguson, & Scovazzo, 2005). Because temperature affects gas solubility, these differences may simply be due to increased CO_2 solubility at the lower temperature in this study. As only one measurement of CO_2 in each neat IL was made for this study, a standard deviation cannot be provided.

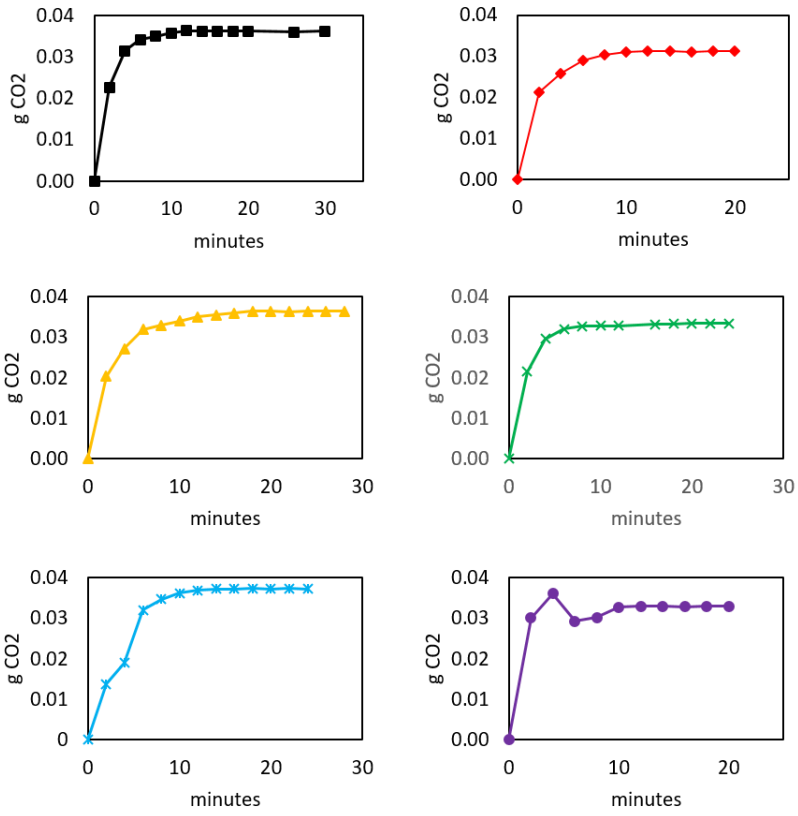

Figure 26. Mass of CO_2 measured in 6 neat ILs over time during 100% CO_2 sparging at 12.2 psia; (◆) [bmpyrr][TFA], (▲) [bmpy][TFA], (×) [bmpz][TFA], (✳) [bmim][TFA], (●) [bm3tri][TFA], and (■) [emim][OTf]

Cyclic voltammetry scans of CO_2-sparged 30 mol% [emim][OTf] in water at a silver electrode at scan rates of 0.01, 0.10, 0.25, 0.50, and 1.0 V s^{-1} are shown in Figure 27, with the lowest scan rates represented as the lightest color and the highest scan rate as the darkest color. The inset of Figure 27 is the Randles-Sevcik plot of I_{pc} vs. $v^{-0.5}$ without background subtraction. Background scans were not taken for all scan rates with this sample, but only for 0.1 V s^{-1}, where the blank background was 5.6% of the peak current with CO_2 at the same potential. In comparison, the blank backgrounds of the [bmpyrr][TFA] and [bmim][TFA] scans were c.a. 40-50% of the CO_2 peak current signal at the same potential. The slope of the linear fit of I_{pc} vs. $v^{-0.5}$ for CO_2 reduction in 30 mol% [emim][OTf] is 0.0108, as shown in the fitting equation in the inset of Figure 27. The transfer coefficient is determined to be $\alpha = 0.54$ for [emim][OTf].

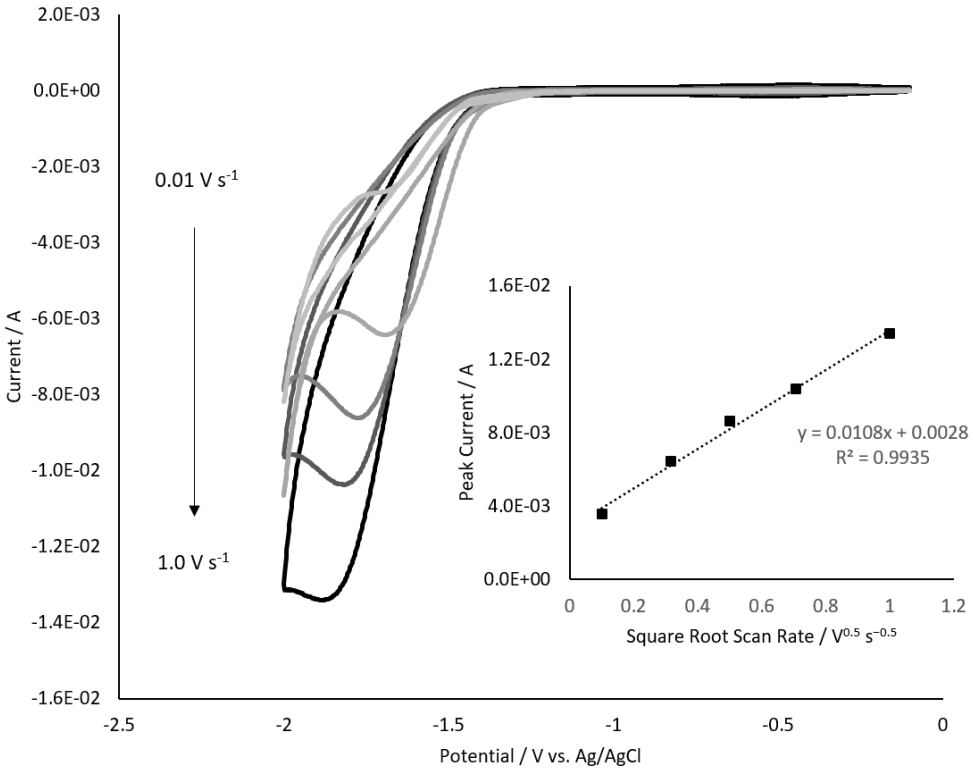

Figure 27. Scan rate dependence of CO_2 reduction in 30mol% [emim][OTf] and water. Inset is the plot of peak current versus square root of the scan rate.

Using the values listed above and Equation 25, and assuming the CO_2 solubility in [emim][OTf] is unchanged at 30 mol% [emim][OTf] in water compared with the neat IL, the diffusion coefficient of CO_2 is calculated to be $D_{CO2} = 1.7 \times 10^{-11}$ m^2 s^{-1}. This D_{CO2} is lower by 1 to 1.5 orders of magnitude compared with the values reported in literature: diffusion coefficients of CO_2 in the neat IL [emim][OTf] reported in literature range from 1.0×10^{-10} m^2 s^{-1} to 5.5×10^{-10} m^2 s^{-1} at 25 to 30°C, respectively (Reche et al., 2014; Morgan et al., 2005). Questioning the assumption of unchanged CO_2 solubility, a study by Zakrzewska et al. shows that a 10 wt% water addition to [emim][OTf] (this roughly matches to 70 mol% water, or 30 mol% [emim][OTf]) decreases the absolute mole fraction of CO_2 in the solution at 2 MPa and 313.15 K to half of that without water (i.e. neat) (Zakrzewska & Nunes Da Ponte, 2018). With a revised estimate of $x_{CO2,abs} = 0.0092$, the revised diffusion coefficient of CO_2 in this solution is estimated to be $D_{CO2} = 6.73 \times 10^{-11}$ m^2 s^{-1}, which remains a 0.5 to 1 order of magnitude lower than literature for the neat IL. While reduced viscosity of an IL with increased water content is expected to improve CO_2 transport in the solution, these

results indicate that CO_2 transport may be hindered in the IL with increased water content. More precise values for CO_2 solubility in aqueous solutions of ILs would be needed to further study this phenomenon before any conclusions can be made. However, this analysis was also carried out for the ILs [bmpyrr][TFA] and [bmim][TFA] to discern if these ILs exhibit different behavior from [emim][OTf] with respect to CO_2 mobility, although there are no reports in literature for these ILs to compare with.

Figure 28 shows the CV scans of CO_2 reduction in 30 mol% [bmpyrr][TFA] in water at a silver electrode and at scan rates of 0.01, 0.10, 0.25, 0.50, and 1.0 V s^{-1}, with an inset of the Randles-Sevcik plot of I_{pc} vs. $\nu^{-0.5}$. The CV curves are shaded from lightest to darkest as slowest to fastest scan rates.

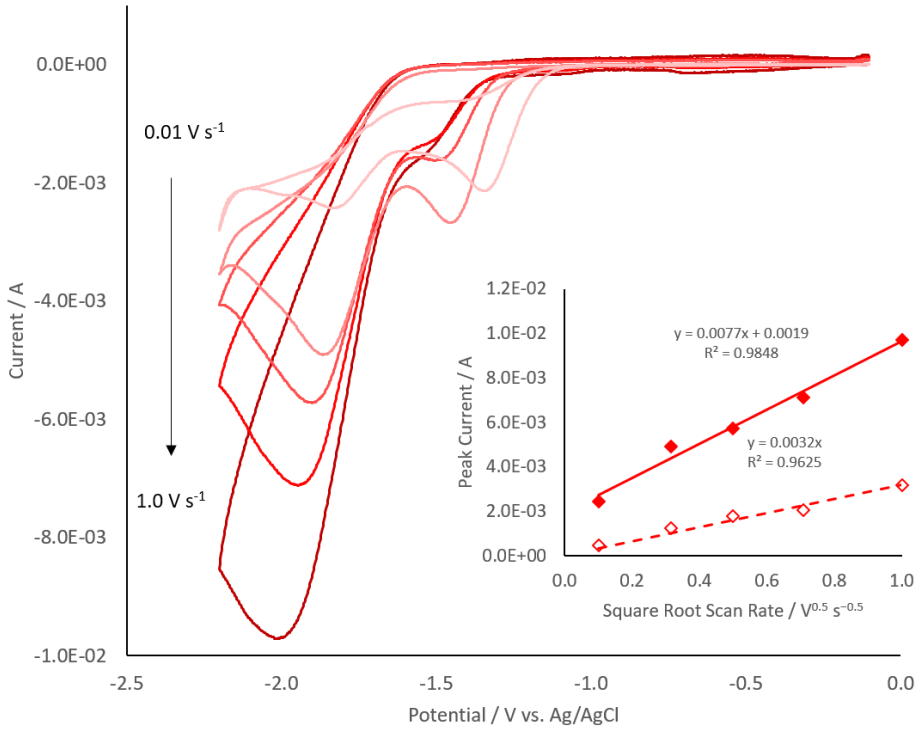

Figure 28. Scan rate dependence of CO_2 reduction in 30 mol% [bmpyrr][TFA] and water. Inset is the plot of peak current versus square root of the scan rate.

The solid data points with a solid line linear fit in the inset of Figure 28 are the peak current values without subtracting the background current present when only argon has been sparged through the electrolyte. Due to the concurrent occurrence of HER with CO_2 reduction in 30 mol% [bmpyrr][TFA] in water at the potentials scanned, as is clear from CV and CPE experiments above, background scans at each

scan rate with Ar purged through the electrolyte prior to CO_2 introduction were conducted (not shown). The current measured in the background CVs at the potential of peak current (E_{pc}) from the CO_2-saturated CVs was subtracted from the I_{pc} values shown in Figure 28. These background-subtracted peak currents are reported as the unfilled data points and dashed lines in the inset of Figure 28, and they are estimated to represent actual CO_2 reduction currents. The slope of the linear fit to the background subtracted plot of I_{pc} vs. $v^{-0.5}$ is 0.0032, and the transfer coefficient is calculated to be $\alpha = 0.4$. After halving the value for CO_2 solubility from the neat [bmpyrr][TFA] ($x_{CO2} = 0.0149$) to the 30 mol% [bmpyrr][TFA] in water ($x_{CO2,abs} = 0.00745$), the diffusion coefficient of CO_2 in this solution is determined as $D_{CO2} = 1.96 \times 10^{-11}$ m^2 s^{-1}.

Lastly, Figure 29 shows the CV scans of CO_2 reduction in 30 mol% [bmim][TFA] in water at a silver electrode and at scan rates of 0.01, 0.025, 0.05, 0.10, 0.25 and 0.50 V s^{-1}, with an inset of the Randles-Sevcik plot of I_{pc} vs. $v^{-0.5}$. The CV curves are shaded from lightest to darkest as slowest to fastest scan rates.

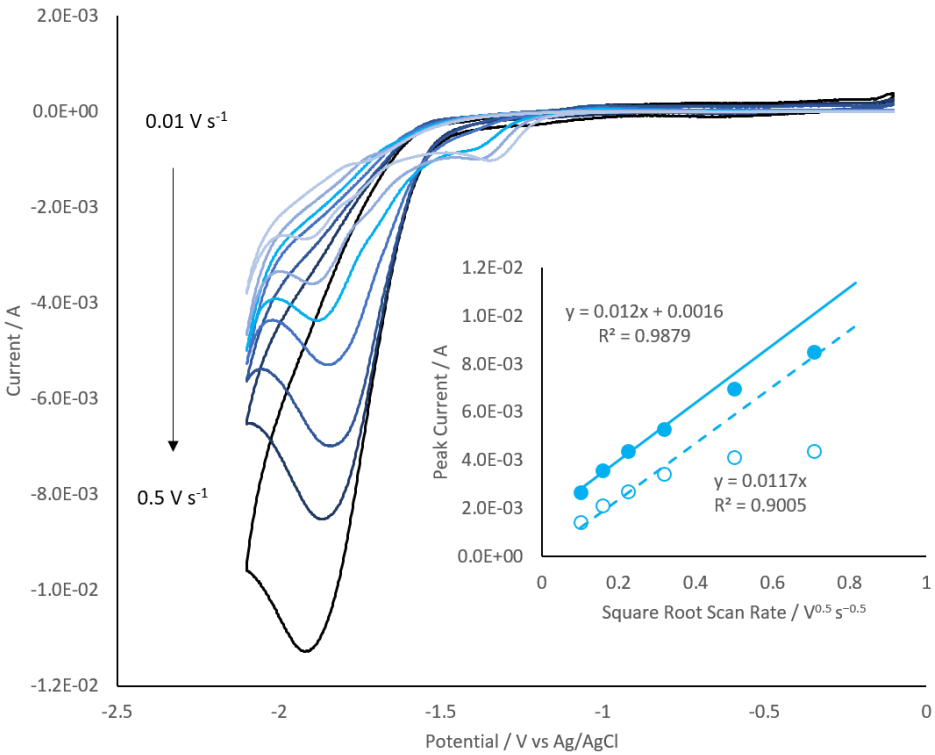

Figure 29. Scan rate dependence of CO_2 reduction in 30 mol% [bmim][TFA] and water. Inset is the plot of peak current versus square root of the scan rate.

Similar to the case for [bmpyrr][TFA], HER is observed in 30 mol% [bmim][TFA] in water without CO_2 present, and thus background CVs with only argon sparged through the solution were made at the same scan rates as those for the CO_2 CVs. The background current was similarly subtracted from the I_{pc} of each CO_2-saturated scan. In the inset of Figure 29, solid data points and the solid linear fit represent peak currents without background current subtraction, and the unfilled data points and dashed line linear fit are the background subtracted peak currents. It can be seen that in both cases, at high scan rates the peak current response becomes flat, indicating mass transport limitations at high scan rates (which is the cause of measurements being taken at lower scan rates for this aqueous IL solution).

The slope of the linear fit to the background subtracted plot of I_{pc} vs. $v^{-0.5}$ is 0.0117, and the transfer coefficient is calculated to be $\alpha = 0.38$. After halving the value for CO_2 solubility from the neat [bmim][TFA] ($x_{CO2} = 0.0184$) to the 30 mol% [bmim][TFA] in water ($x_{CO2,abs} = 0.0092$), the diffusion coefficient of CO_2 in this solution is determined as $D_{CO2} = 1.59 \times 10^{-10}$ m^2 s^{-1}.

5.4 Summary

The effects of seven different ILs on the performance of electrochemical reduction of CO_2 in 30mol% IL/water solutions at a silver macro electrode were investigated with blank and CO_2-saturated CV scans and constant potential electrolysis with gaseous product analysis. Six of these ILs were further studied to determine the CO_2 solubility in them without water present, and subsequently three of these ILs were investigated with Randles-Sevcik analysis to determine the diffusion coefficient of CO_2 in 30mol% solutions of the three different ILs in water. From these results, imidazolium and pyrrolidinium IL cations help facilitate CO_2 reduction to CO, as expected from literature, and that pyrazolium cations can facilitate some minor CO_2 reduction to CO at low potentials, below its breakdown potential. As this appears to be the first study to investigate electrochemical CO_2 reduction with trifluoroacetate anion-based ILs, a better understanding of how the anion of the IL affects CO_2 reduction can be gained when comparing these results with those of the same cation and different anions.

5.5 Related Presentations and Publications:

Holquist, J. B., Klaus, D. M., Nabity, J. A., and Abney, M. B. (2016). Ionic Liquid Selection and Initial Test Results for Electrochemical Carbon Dioxide Reduction (poster, 1st place), *46th International Conference on Environmental Systems*, Vienna, Austria.

Holquist, J. B., and Klaus, D.M. (20XX). Experimental Evaluation of Trifluoroacetate Ionic Liquids with 7 Varied N-Heterocycle Cations for Electrochemical Reduction of Carbon Dioxide in Aqueous Solutions at Silver Electrodes. [In prep – Working Title].

Chapter 6 – Prototype Flow Cell CO_2 Electrolyzer

6.1 Introduction

Flow cell electrolysis is a common way to facilitate a continuous electrochemical reaction while separating products and providing adequate fluid mixing and reactant distribution within the cell. It also enables a practical means of process monitoring and control, where external sensors and injectors can monitor and adjust solutions as reactants may deplete from one side of the electrochemical cell (e.g. water loss due to oxidation in the anode compartment of a CO_2 electrolysis cell). In such an electrolyzer, a reaction can proceed continuously, while maintaining constant conditions (with appropriate process control) and allows for the analysis of long term performance stability for the cell and cell materials.

In this chapter, the major design options for flow cell electrolyzers are presented with a brief discussion and recent performance metrics from relevant systems are reviewed. The considerations necessary for using standard configurations of flow cell CO_2 electrolysis in spaceflight applications are also discussed and reviewed, leading to the presentation of a design concept, vacuum-assisted product removal (VAPR) for flow cell electrolyzers. A prototype VAPR flow cell CO_2 electrolyzer was designed and fabricated in-house for proof-of-concept testing. A dedicated gas handling and analysis subsystem, a variable flow rate 2-liquid recirculation subsystem, and a command and data handling subsystem were all designed and developed in-house to serve as a test bed for controlling and analyzing the performance of the VAPR flow cell CO_2 electrolyzer prototype. It should be noted that the simplest and most robust way to investigate using ILs for CO_2 electrolysis in a flow cell electrolyzer is to procure a commercially available flow cell electrolyzer with enough modularity to alter the pertinent materials (e.g. cathode catalyst, membrane). This effectively eliminates the risk of fabrication errors, includes best industry design practices, and will ensure results that are based on the ionic liquids and catalyst, rather than artifacts of using non-standard equipment. However, other research groups have developed their own flow cell electrolyzers for studying CO_2 electrolysis to good effect (Delacourt, Ridgway, Kerr, & Newman, 2008; Whipple, Finke, & Kenis, 2010) when customizable aspects are desired.

6.2 Background and Motivation

There have been incremental advancements in the components comprising a low-temperature CO_2 electrolysis cell that have begun to make this process more viable for practical implementation. These advancements include the development of 1) gas diffusion electrodes (GDE), most notably used in fuel cells, 2) cation exchange membranes, e.g. Nafion®, 3) catalyst materials (new materials and new structuring of traditional materials), and 4) ionic liquid electrolytes. As pointed out by Weekes et al, the vast majority of publications related to CO_2 electrolysis in the last decade, shown in Figure 30, have been most focused on catalyst (Item 3), and electrolyte/solvent (Item 4) interactions in small, transport-limited H-type cells, such as seen in Chapter 5 (Weekes et al., 2018). Items 1 (GDEs) and 2 (CEPs) have both seen common use in other electrolyzers or fuel cells in both commercial applications and active research, while CEP research has also been present in H-type cell studies.

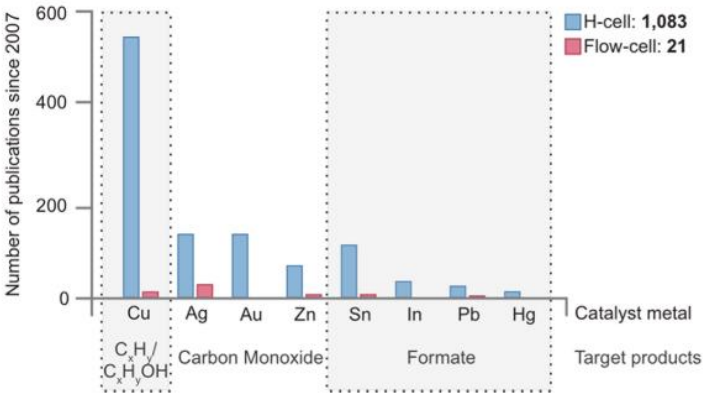

Figure 30. Number of publications on CO_2 electrolysis since 2007 based on H-cell vs. Flow-cell testing (Weekes et al., 2018)

Gas diffusion electrodes have been prevalent in fuel cell technology for decades. In fact, one of the first uses of fuel cells (employing GDEs, or at the time, "porous electrodes") was in the U.S. Apollo Space Program (M. L. Perry & Fuller, 2002). In efforts to improve solvated CO_2 electrolysis, studies have long recognized that high pressure, gas phase CO_2 introduced at the cathode can reduce transport issues of reducing CO_2 dissolved in the bulk electrolyte solution (Hara, Kudo, & Sakata, 1995; Yamamoto, Tryk, Fujishimal, & Ohata, 2002). More examples of CO_2 electrolysis employing GDEs are given below.

In addition to CEMs, even more recently, anion exchange membranes (AEMs) and bi-polar membranes (BPMs) have been the subject of research for CO_2 electrolysis. In an AEM-based cell, the actively transported ions are OH^- and any other anions in the electrolyte, e.g. HCO_3^- and CO_3^{2-}. For reasonable ion concentrations for ion conductance through the cell and AEM, the electrolyte used must be basic, which in turn helps with the suppression of the hydrogen evolution reaction, due to the low concentration of H^+ ions available for reduction. AEM-electrolyzers have typically suffered from sluggish ion conductance and stability of the membrane, in addition to build up of bicarbonate and carbonate in solution that both lower conductance and act to transport active CO_2 reactant from the cathode (Weekes et al., 2018). Because basic media readily reacts with CO_2 to produce bicarbonate and carbonate, excess CO_2 needs to be present at the cathode (GDEs are particularly useful here) to compete with conversion of CO_2 to other forms. An AEM was developed for the CO_2 electrolysis application specifically, and has demonstrated good performance (>90% FE_{CO} at −50 mA cm^{-2} and 3.0 V across the cell for >4500 h) (Kutz et al., 2016).

Bi-polar membranes, on the other hand, have been used in a few recent studies to allow for extreme pH conditions at the anode and cathode, in which CO_2 reduction can take place in mildly acidic conditions and water oxidation can occur in alkaline conditions, which facilitate improved kinetics for both reactions. Water is dissociated at the BPM to H^+ and OH^- to allow the appropriate ion to conduct to the corresponding electrolyte. Recent reports have shown that BMPs can help enable long-term electrolyzer stability in conditions where AEMs and CEMs would fail, however, efforts are needed to better understand conditions and improve reactor design that maintain product selectivity (Li et al., 2016; Vermaas & Smith, 2016) .

For spaceflight applications, precedent is set for using a flow cell electrolyzer by the Oxygen Generator Assembly (OGA) on board the International Space Station (ISS), which uses a CEM, flowing water electrolyzer to generate oxygen from water at sufficient rates to keep up with crew metabolic O_2 requirements. The OGA operates in cathode-feed mode with purified water provided to the cathode compartment for reduction. In the OGA, hydrogen is generated at the cathode and remains downstream in

the water until it is passed to a rotary-separator accumulator (RSA), a system for gas-liquid separation in a microgravity environment, which uses centripetal acceleration to push liquid to the walls of the separator with gas being removed from the center line of rotation. Due to its longer history of development and characterization, commercial availability, and precedent of being used in spaceflight applications, only CEM-based CO_2 electrolysis configurations were considered further in this research.

While a CO_2 electrolysis process in an IL will be a much more chemically complex system, the overall supporting system and implementation considerations will be similar, as discussed in Chapter 3. The main configurations of CO_2 electrolyzers that have been studied are based on fuel cell-type, fuel cell-type with buffer layer(s) (Whipple et al., 2010), and recirculating electrolyte (Delacourt et al., 2008). Simple schematics are outlined in Figure 31 below, where Figure 31 (right) and (center) correspond to the earlier presented generic cells in Figure 3 and Figure 4, respectively.

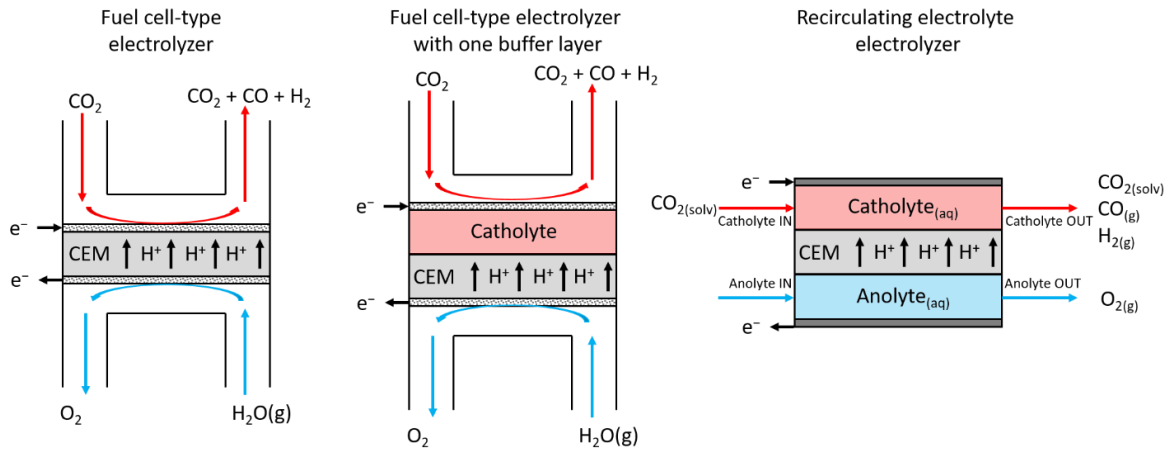

Figure 31. Simplified standard electrolyzer configurations

The purely fuel cell-type CO_2 electrolyzers, also called membrane reactors due to using membrane electrode assemblies (MEAs) (Figure 31, left) have not been successful due to poor (if any) conversion of CO_2. Only recently, a study by Wang et al. has shown that using an alkaline anion exchange membrane can convert CO_2 to CO in a fuel-cell type electrolyzer with humidified CO_2 gas fed directly to the cathode (no electrolyte), but further show that CEM-based gas-phase fuel-cell type electrolyzers are not viable (G. Wang, Pan, Ping, & Yang, 2018). One recent study purports to use only humidified gas-phase CO_2 for

cathode feed, but the electrode is impregnated with [bmim][OTf], which acts as a CO_2 solvent and co-catalyst in the designed system, fitting more appropriately in the next category (Li et al., 2016).

Fuel cell-type CO_2 electrolyzers with a buffer layer (Figure 31, middle) are much more favorable and have received the most attention recently (only a catholyte buffer layer is shown, but an anolyte buffer layer can also be included). These designs benefit from CO_2 contacting both the cathodic catalyst on a GDE and the buffer layer solution within the pores of the GDE. This allows for the highest possible concentration of CO_2 in solution at the catalyst surface, which helps to mitigate the transport limitations of using only solvated CO_2 as reactant. One issue that can be seen is that the pressurized CO_2 behind the GDE can force electrolyte out of and away from the pores of the GDE, causing decreased Faradaic efficiency of the electrolyzer for CO_2 reduction products over time. Gaseous product removal also presents an issue in this design. Bubbles can either remain in the solution to be separated down-stream or they can traverse back into the gaseous headspace behind the cathode where CO_2 is introduced. Either case can present additional complexities for space applications: in the former scenario, the bubbles must be separated from the electrolyte by a different system (a rotary separator in a microgravity environment). In the latter scenario, the electrolyzer must be operated with CO_2 introduced in a batch mode and the electrolyzer allowed to run until the gas is all converted to reduced products. Otherwise, if the electrolyzer is operated with continuously flowing CO_2, the reduced products will be present in dilute quantities in a bulk gas of CO_2 requiring additional separation or making the outlet gas difficult to use in a downstream system.

In a recirculating electrolyte electrolyzer, (Figure 31, right), CO_2 is only introduced to the cathode in solution. This configuration inherently limits the reaction rate based on the bulk solubility of CO_2 in the catholyte, governed by Equation 17 (repeated here for clarity), and is affected by mass transport limitations (Najafabadi, 2013).

$$i_L = nFK_mC_b \tag{17}$$

where, i_L is the limiting current density (mA/cm^2), n is the electron stoichiometry coefficient for the reaction (n=2 for CO_2→CO and 8 for CO_2→CH_4, see Equations 2 and 3), F is Faraday's constant = 96,485 C/mol, K_m is the mass transfer coefficient (K_m = 1x10^{-5} m/s for CO_2 in water), and C_b is the bulk concentration of the reactant species (C_b = 0.03 kmol/m^3 in water). For electrochemical CO_2 reduction in CO_2 saturated water, the limiting current density is thus calculated to be i_L = 6 mA/cm^2, where the area is the electrochemically active surface area. This transport limitation is governed by the diffusion layer thickness between the catalyst and the bulk solution and the diffusion rate of CO_2 in the solution, and it is the reason that research has been heavily invested in CO_2 introduction via a GDE or finding electrolytes with higher CO_2 solubility and mobility in solution, such as ionic liquids.

Lastly, it is important to keep in mind that these types of electrolyzers require a down-stream gas-liquid separation process, which can be non-trivial in a microgravity environment. In addition, if micro- or nano-structured cathode materials are used (which often exhibit the most favorable performance metrics, (M. Asadi et al., 2016)), reduced CO_2 products can remain trapped in the pores, inhibiting accessibility of reactants to the catalyst surface and degrading the performance of the electrolyzer over time. Because CO_2 electrolysis can be advantageous in microgravity environments, it is pertinent to consider issues that may be presented by two-phase flow caused by bubble generation in the electrolyzer: bubbles can cavitate pumps and limit contact of the electrode with the electrolyte solution, in turn limiting the conducting cross-sectional area and active catalyst in contact with the electrolyte. With these application-specific concerns in mind, a different style of CO_2 electrolyzer is envisioned that may alleviate some issues; the roots of which lie in devices for differential electrochemical mass spectroscopy (DEMS).

6.3 Vacuum-Assisted Product Removal (VAPR) CO_2 Electrolysis

An alternative configuration for a CO_2 electrolyzer is proposed with the objective of high per-pass CO_2 utilization efficiency, high purity gaseous product output, and little to no need for gas-liquid separation of products from the electrolyte. As can be seen in Figure 32, like the recirculating electrolyte configuration, CO_2 is introduced to the cell in solution flowing past the cathode.

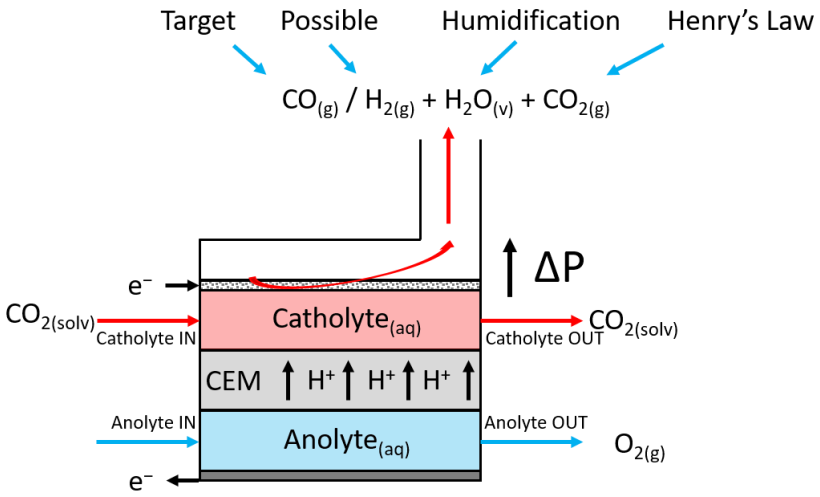

Figure 32. Vacuum-Assisted Product Removal (VAPR) CO_2 Electrolysis

Similar to the fuel cell-type configuration, a catalyst-coated gas diffusion electrode is used for the cathode, but instead of introducing any gas on the backside of the cathode, a vacuum is pulled through an outlet of the gas headspace. The intent of this vacuum is to separate gaseous products through the GDE as they are electrochemically generated in a process we are calling vacuum-assisted product removal (VAPR). Because the gaseous products (e.g. CO) are poorly soluble in the catholyte and will exist mostly as bubbles, they should be pulled through the GDE more readily than dissolved CO_2 and water in the catholyte. A hydrophobic, microporous GDE was selected to limit the crossover of catholyte into the gas headspace behind the GDE. Clearly, this process will require a careful balance of GDE porosity and hydrophobicity, vacuum pressure, electrolysis reaction rate, and catholyte flow rate to be feasible. The most similar style of electrolyzer to this configuration is used in differential electrochemical mass spectroscopy (DEMS), which is used for real-time analysis of liquid and gas-phase electrolysis products generated in small quantities (working electrodes ~1-2 cm). It has only recently been improved to the point of reliable product quantification, though still at relatively small scales (Clark, Singh, Kwon, & Bell, 2015).

The VAPR-process CO_2 electrolyzer's applicability is enhanced by the use of ILs as non-volatile solvents and electrolytes, with 1-ethyl-imidazolium trifluoromethanesulfonate [emim][OTf] selected for this study in particular. This IL was selected because of its common use in literature for this application, allowing for easily comparable performance results. The solubility of CO_2 in [emim][OTf] is ~0.08 kmol

CO_2/m^3 [emim][OTf], or 2.35 times that of water in the same units at 101 kPa of CO_2 and 298 K (Reche et al., 2014). Using Equation 17, this puts the limiting current density of CO_2 reduction in [emim][OTf] at 15.4 mA/cm^2 of electrochemically active surface area. Because the purpose of this prototype is to study the VAPR process in particular (at a larger scale than DEMS electrolyzers), the IL and other components of the CO_2 electrolyzer were not optimized for the best electrochemical performance of the cell. For future studies based on this design, it should be kept in mind that other ILs exist with more than an order of magnitude more solubility for CO_2, better performing cathodes and anodes exist, additional supporting electrolytes can be added, temperature can be raised, better seals can be included, and cell dimensions can be optimized for significantly reduced resistive losses.

6.4 The VAPR CO_2 Electrolyzer Test Bed

An electrolyzer was designed and fabricated in-house at CU Boulder to test the feasibility of a vacuum-assisted product removal process with low temperature, solvated, electrochemical CO_2 reduction. A schematic representation of the electrolyzer can be seen in Figure 33.

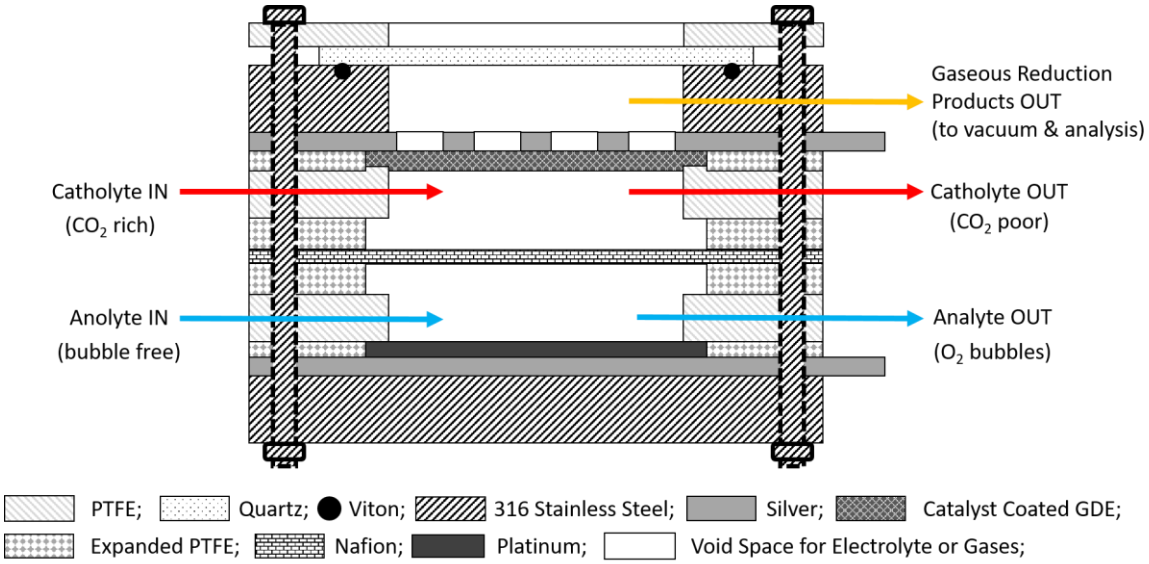

Figure 33. Notional cross-sectional view of electrolysis cell

The concept of operation for the electrolyzer as follows: Solvated CO_2 in an aqueous IL (1-ethyl-3-methylimidazolium trifluoromethanesulfonate, [emim][OTf]) is continuously circulated through the

cathode compartment, while an acidic electrolyte (0.1 M sulfuric acid; Sigma Aldrich) is circulated through the anode compartment. The compartments are separated by a cation exchange membrane (Nafion® 117, Fuel Cells Etc). When an electrical potential is applied across the working (cathode) and counter (anode) electrodes, CO_2 is reduced at the cathode and water is oxidized at the anode, with hydrated protons travelling across the Nafion® membrane to complete the circuit. In this set up, while water oxidation is the only reaction that can occur at the anode, the possible cathodic (half-cell) reactions are shown in Equations 2, 7, and 8, repeated here:

Hydrogen Evolution Reaction (HER)	$2H^+ + 2e^- \rightarrow H_2$	$E^0 = 0.00$ V vs SHE	(10)
Electrochemical CO_2 to CO	$CO_2 + 2H^+ + 2e^- \rightarrow CO + H_2O$	$E^0 = -0.11$ V vs SHE	(7)
Electrochemical CO_2 to CH_4	$2CO_2 + 8H^+ + 8e^- \rightarrow CH_4 + 2H_2O$	$E^0 = -0.24$ V vs SHE	(8)

Based on the catalyst used in this cell (silver) only Equations 2 and 7 are expected. During electrolysis, a regulated vacuum pressure (−1.5 to −6.0 psig, possible range) is applied to the backside of the GDE cathode such that the gaseous products generated at the cathode are removed for analysis, quantification, and (possible) down-stream use in another system. The performance of this vacuum-assisted product removal process will be dependent on the characteristics of the GDEs, the flow rate of the catholyte, rate of electrolytic product generation, and the applied vacuum pressure. As such, the intent of the experiments with this electrolyzer will not only be to evaluate the electrolysis process, but also the VAPR process, by parametric variation of the GDE, flow rates, electrolysis potential, and vacuum pressure.

The cathode is a gas diffusion electrode made of woven carbon cloth (ELAT 2400W, NuVant), coated with silver nanoparticles (20-40 um particle diameter, Sigma Aldrich) supported by a Nafion® binder (Nafion D-521 dispersion, 5 wt% in water, Alfa Aesar). The anode is an unmodified platinum foil (0.025 mm thick, 99.9%, Sigma Aldrich). The reference electrode is a leak-free Ag/AgCl electrode in a PEEK shell with a reported junction potential of 30 kΩ and a filling solution of 3.4 M KCl (LF-2, Innovative Instruments, Inc). The backings to the cathode and anode are silver foils (0.28 mm thick, 99.9%, Alfa Aesar)

that act as charge distributors to avoid issues of transverse electrical resistance across the GDE and to provide rigidity for compression. The silver sheet backing the cathode is perforated with large holes to allow gas transfer through the GDE and visual evaluation from a quartz window (Technical Glass Products) behind the cathode gas collection head space. This window was used during initial testing to evaluate if flooding of the gas collection head space is occurring at a given set of parameters. In later tests, a stainless steel 316 plate was used without the quartz window to improve compression of the gaskets and reduce leaks into the system. The electrolyzer with the quartz window can be seen in Figure 34 (left) and without the quartz window, installed in the test bed, in Figure 34 (right).

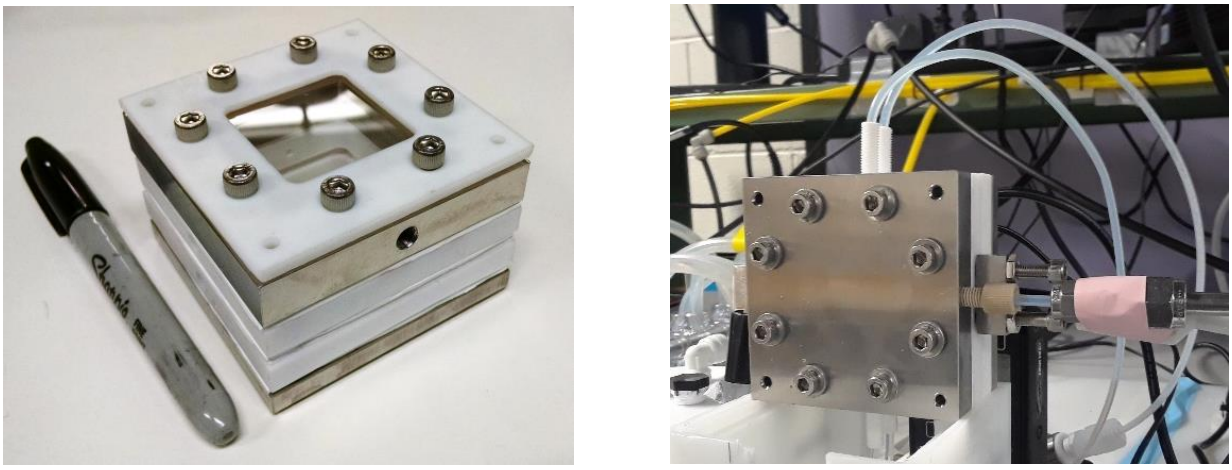

Figure 34. Picture of the VAPR process CO_2 electrolyzer

It is important to note that bulk silver acting as the cathode for CO_2 electrolysis preferentially produces CO, so in the case of catholyte contacting the electrified silver sheet backing, a desired product will still be produced with good selectivity (Hori, 2008). All gasket materials are made of expanded PTFE (Gore) and the O-ring used to seal the quartz window is made of Viton® (The O-Ring Store). The compression plates are made of stainless steel 316 and the cathode and anode compartments are made of virgin PTFE. The fittings are all gas tight, sealed with PTFE-coated O-rings. These materials were selected to provide the highest certainty that the [emim][OTf] does not chemically react with any electrolyzer parts, because complete materials compatibility tests still have not been done (Uerdingen, Treber, Balser, Schmitt, & Werner, 2005). The bolts compressing the electrolyzer are electrically isolated from the stainless steel and

the electrodes by way of insulative plastic sleeve inserts to prevent conduction across anything other than the electrolysis process.

6.4.1 Procedure for Gas Diffusion Electrode Preparation

The gas diffusion electrode was prepared from airbrushing a catalyst and binder mixture onto each side of the gas diffusion layer. Airbrushing as a catalyst layer deposition methodology onto a GDL has been demonstrated as a superior method to other simple forms of catalyst deposition (H. R. Q. Jhong, Brushett, & Kenis, 2013). A solution of Nafion® binder, water, and isopropyl alcohol was mixed with the appropriate mass of silver nanoparticles (AgNPs) to achieve the approximate desired (~1 mg/cm^2 per side) loading by mass on the GDL. The GDE was coated on both sides with catalyst in order to account for electrolyte that may pass through to the other side of the GDE due to low bubble point pressure (discussed below), in order to prevent the electrolyte from contacting non-catalyst material (e.g. carbon). The mixture was sonicated for 20 minutes, then loaded into the airbrush reservoir. The GDL was sprayed with an N_2 carrier gas at an even height (~5 cm) and rate of transverse movement in sweeps that extend past the edge of the GDL to ensure as uniform of loading as possible. Hazard note: the operator of the airbrush should wear a respirator and skin protection as silver nanoparticles can be hazardous to one's health. Afterwards the GDE was dried in a vacuum oven for 2 h (−30 inHg, 60^{o}C) and stored in air. Due to silver being oxidized during storage in air, a reducing current must be applied initially with the electrode in order to strip the oxide layer off the catalyst. The GDE was weighed to determine mass loading of the AgNPs (c.a. 1 mg/cm^2) on a geometric surface area of be 25 cm^2 (5 cm x 5 cm).

6.4.2 Operating Conditions

The VAPR process relies on the gas diffusion electrode and a gas permeable membrane behind the GDE to serve as gas-liquid separators as the product gas is generated at the GDE. Because the expected CO and H_2 gaseous products are poorly soluble in IL or water, they will mostly exist as bubbles. In a gravity environment, the orientation of the flow cell can be made so that buoyancy drives bubbles towards the reduced-pressure headspace, assisting with their separation from the liquid electrolyte. In a microgravity

environment, it is postulated that having the reduced-pressure headspace just on the backside of the GDE where the bubbles are generated, perhaps the bubbles can be drawn through the GDE and gas permeable membrane before they can be entrained by the flow. In either case, a careful balance of the differential pressure from the electrolyte to the gas handling system will need to be maintained. This can be affected by sweep gas flow, electrolyte flow rate, and the residence time of possibly bubble-containing electrolyte in contact with the GDE, which can all be tailored and monitored by including features such as a serpentine flow pattern for the electrolyte, thin electrolyte layers (to limit bubble diffusion away from the GDE), and sensors to track liquid and gas.

For this study, the main concerns were maximizing gas transport through the GDE and gas permeable membrane and to preventing liquid infiltration into the gas collection headspace. The GDL ELAT 2400W and Porex PM21M hydrophobic, gas permeable PTFE membrane (Fuel Cell Store) were selected and tested. The specifications for ELAT 2400W was determined to be likely the most resistant to liquid crossing through the GDE, due to its hydrophobic treatment, low porosity compared with other GDLs, and its 2 microporous layers. While only ELAT 2400W was tested, it is currently unknown which GDL will offer the best combination of properties for the VAPR process, the properties of other GDLs are presented in Table 13 as well for readers to see the range of specifications from a common array of GDLs.

Table 13. Properties of the gas diffusion layers (Fuel Cells Etc), MPL = Micro Porous Layer

Gas Diffusion Layer	Type	Thickness (µm)	Air Permeability	Porosity	PTFE Treated (hydrophobic)	MPL
ELAT LT 1400 W	Cloth	454	0.104 $L/(m^2*s*Pa)$	63%	Yes	1
ELAT LT 2400 W	Cloth	490	10 $cm^3/(cm^2*s)$	31%	Yes	2
Sigracet 29 BC	Paper	235	1 $cm^3/(cm^2*s)$	80%	Yes	1
GDL-CT	Cloth	410	<8 (s)	-	Yes	1
AvCarb GDS2120	Paper	248	-	-	Yes	1
Torray Paper TGP H 120	Paper	370	-	78%	No	0

Because liquid infiltration through the GDE and gas permeable membrane would represent a catastrophic failure for a VAPR electrolyzer (though it was protected against in the gas handling system,

described below), the maximum operating differential pressures was calculated analytically from the bubble point equation (Equation 27) and investigated experimentally.

Bubble Point Equation $$P_B = \frac{4k\sigma \cos\theta}{d} \quad (27)$$

where, P_B is the bubble point pressure, or the minimum pressure differential required to force liquid out of the pores, k is a shape factor (depends on pore shape and path tortuosity), σ is the liquid surface tension, θ is the solid-liquid contact angle, and d is the pore diameter.

The GDL ELAT 2400W has the specification of d = 31 µm pore diameter (FuelCellsEtc, 2018). From a study by Sung et al., when aqueous-IL solutions have bulk mole fractions greater than 20mol%, the surface tension of the solution can be approximated by the surface tension of the IL (Sung, Jeon, Kim, Iwahashi, & Iimori, 2005). With this, the surface tension of [emim][OTf] can be estimated as σ_{IL} = 40.52 mN m^{-1} at 293K (Součková, Klomfar, & Pátek, 2011). A study by Dubois et al. investigates the contact angles of various ILs on electrodes of gold structured on silicon with a PTFE hydrophobic coating, with the range of IL contact angles being θ = 70–95°, depending on the IL used. While not the exact same materials and conditions as used here, the solid-liquid contact angle is estimated as θ = 95°, from the contact angle of [bmim][PF_6], which has a similar surface tension to [emim][OTf] (P. Dubois et al., 2006). The shape factor, k, is estimated as k = 0.33, based on an irregular (non-circular) pore structure (Eisenmann, 2008). With these factors, the bubble point pressure for ELAT 2400W is estimated as P_B = 0.3 psid without any catalyst coating. It is expected that the catalyst coating (silver nanoparticles with Nafion® binder) will increase P_B, but to what extent is unknown, therefore necessitating a backing gas permeable membrane to compensate for the low P_B of the GDL to prevent infiltration of liquid into the gas collection headspace.

From the Porex PM21M specifications sheet, the differential pressure required for specified airflow (1500 mL min^{-1} cm^{-2}) is 350 mbar or 5.076 psid, and it is taken as the bubble point pressure when water is the working fluid. This pressure was corrected for the different surface tension of IL compared with water by using Equation 28.

$$P_{B,IL} = \frac{P_{B,H2O}}{\sigma_{H2O}} \sigma_{IL} \quad (28)$$

Therefore, with values of $P_{B,H2O}$ = 5.076 psid, σ_{H2O} = 76 mN m^{-1}, and σ_{IL} = 40.52 mN m^{-1}, it can be calculated that $P_{B,IL}$ = 2.82 psid. For a conservative estimate, the maximum operating pressure difference for operation of the VAPR electrolyzer with the selected materials was taken as 80% of $P_{B,IL}$, or 2.25 psid.

The peristaltic pump head was connected downstream of the electrolyzer and upstream of the mixing tank, thereby applying a negative pressure at the outlet of the electrolyzer to force electrolyte circulation. This configuration has been observed to reduce flow eddies and stagnation within the electrolyte (Clark et al., 2015). Because of this, the differential pressure across the GDE and gas permeable membrane will depend on the flow rate of the electrolyte, where higher flow rates induce lower absolute pressures of the electrolyte and allow for lower applied absolute pressures in the gas handling system. The pressure differential, P_{diff}, can be accessed in the current apparatus by isolating the electrolyzer from the gas handling system with electrolyte flowing and monitoring the pressure of the headspace. The electrolyte recirculation-only operational pressure can be used as the baseline, and the differential pressure across the GDE and membrane will be the baseline minus the applied vacuum pressure with the gas handling system open to the electrolyzer. This functionality was designed into the experimental apparatus, described below.

6.5 Experimental Setup and Procedures

A supporting test bed was designed and assembled in-house. The apparatus, schematic shown in Figure 35, comprises the electrical, liquid, and gas handling systems to provide for complete operation of the electrolyzer and analysis of its performance. Potential and current controls and measurements are performed by an EZStat-Pro potentiostat (±1.0 A, NuVant). Vacuum is maintained by a N85.3KNDCB diaphragm pump with speed control (25 mTorr, KNF Pumps), and the gas collection headspace pressure is regulated by a back-pressure regulator (BPR) (Equilibar) with electronic control. Gas analysis measurements are made by a quadrupole mass spectrometer (MKS Cirrus) through a capillary tube sampling from a 250-mL gas sample flask. The mass spectrometer has a 3-point calibration for expected ranges of H_2 and CO

quantification in a background of Argon, but cannot adequately discern between CO and CO_2 at low partial pressures of CO. As such, a non-dispersive infrared (NDIR) gas analyzer tuned to CO and CH_4 was included with a drying column in-line for tests where gaseous product quantification of CO was necessary, such as the cyclic voltammetry and constant potential electrolysis tests from the previous chapter, and the continuous flow reactor tests described here.

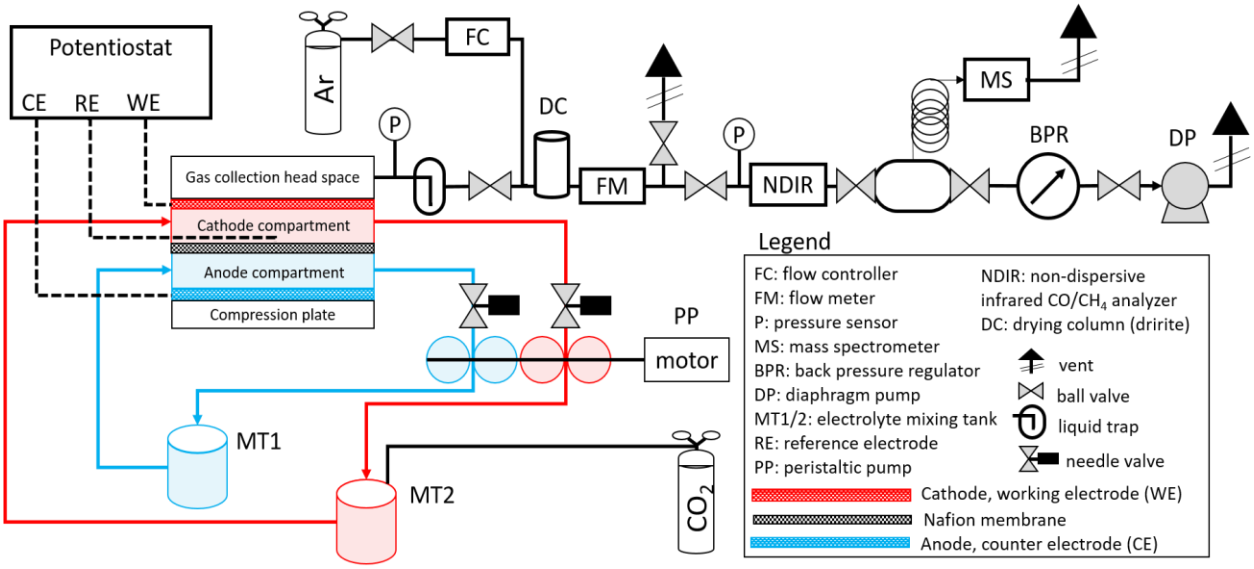

Figure 35. Schematic of electrolyzer support systems: electrolyte circulation & gas-liquid mixing tanks, gaseous product extraction & analysis, and electrical power & connections

Pressure is measured both directly upstream of the mass spectrometer sample port and directly downstream of the gas collection head space of the electrolyzer by 0-15 psia pressure sensors (PX309, ±0.25% accuracy, Omega). Flow rate is measured by a Whisper series mass flow meter (0-150 sccm, ± (0.8% of reading + 0.2% of full scale) accuracy, Alicat). Diluent gas (Ar, 99.999%, Airgas) flow control is provided by a mass flow controller (0-75 sccm, ± (0.8% of reading + 0.2% of full scale) accuracy, Alicat). Liquid electrolyte is recirculated with a quad-head Masterflex peristaltic pump equipped with platinum-cured silicone tubing (0-1100 sccm, Cole-Parmer). Custom, gas-tight mixing tanks were designed and machined in-house out of virgin PTFE and are equipped with 5 psig cracking pressure relief valves.

All electrolyte tubing and connectors, other than the peristaltic tubing, are made of PTFE or PEEK in order to prevent any possible chemical interactions. To test its viability, platinum cured silicone tubing was

submerged in 5 mol% and 75 mol% solution of the ionic liquid in ultrapure water (Milipore, 18.2 MΩ-cm) for 2 weeks to determine if any qualitative changes in either the tubing or the ionic liquid solutions occurred. After the 2-week submersion and a rinse with ultrapure water, no mass change was measured in the tubing between before and after submersion. No cracking, swelling, or discoloration of the tubing was apparent. No color change was observed in the ionic liquid (color change is usually an indicator of contaminants or chemical changes in some amount of the IL).

In a typical experiment, the headspace of mixing tank 2 is flushed with CO_2 (99.999%, Airgas) and held at 14.7 psia (2.5 psig at Boulder, CO, USA ambient pressure). The liquid electrolytes are continuously recirculated after ensuring no leaks are present and that the electrolyzer fluid channels are completely filled. By having the electrolyte flow down into the mixing tank, it is poured through the CO_2 headspace of the tank, assisting with gas uptake. Because the CO_2 gas is not flowing during the experiment, but only maintaining a slight positive pressure, the only CO_2 lost during the experiment is either due to electrolysis (conversion to other products) or dissolution from the electrolyte in the cathode compartment of the electrolyzer. Otherwise the liquid electrolyte recirculation through the CO_2 headspace maintains CO_2 concentration in the electrolyte at saturation for the pressure and temperature (14.7 psia, 23°C), passively replacing the converted or lost CO_2. A picture of the experimental apparatus with the electrolyzer included is shown in Figure 36.

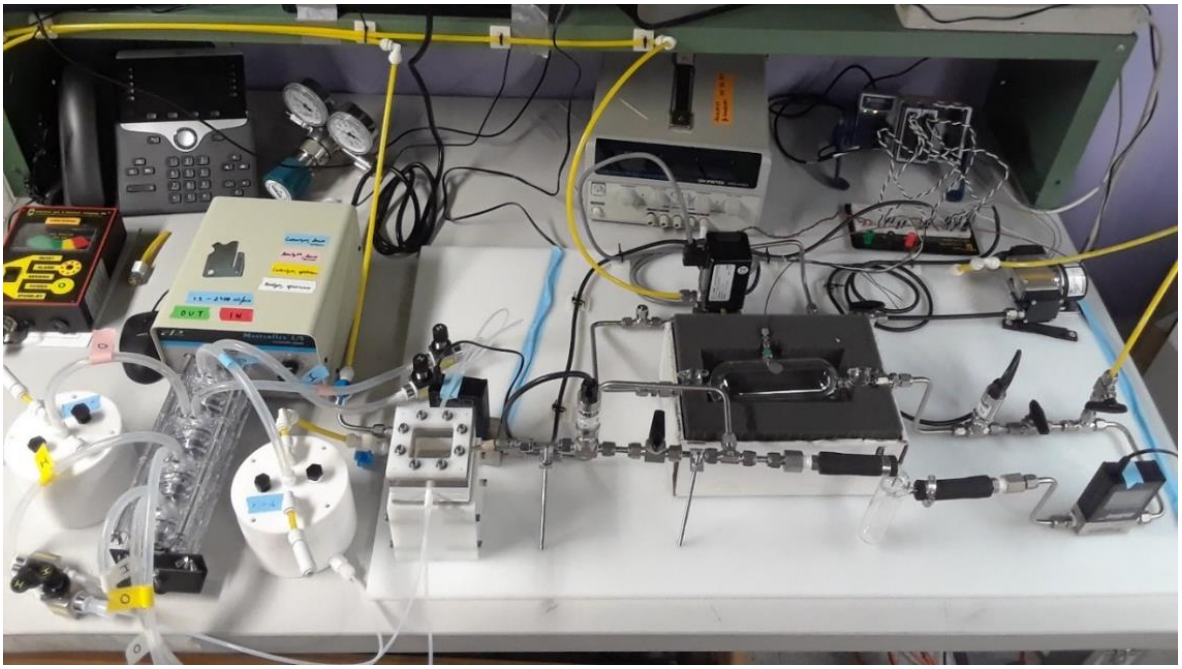

Figure 36. Picture of the experimental apparatus

After the electrolyte is flowing, the gas handling apparatus is turned on and prepared with the electrolyzer isolated by a ball valve in order to set the desired vacuum pressure at the electrolyzer and flow rate of the diluent gas. Prior to beginning electrolysis, the electrolyzer gas collection head space is exposed to vacuum and inspected visually to see if electrolyte is being pulled through the GDE. If not, the potentiostat is powered on and electrolysis is started at the desired potential or current, beginning an experiment.

6.6 Results

Two major results for VAPR flow cell CO_2 electrolyzer testing are presented: pressure testing and product analysis testing. The purpose of pressure testing was to observe the pressure at which liquid infiltration of the gas collection headspace would occur in order to determine maximum operating differential pressures, $P_{diff,max}$, where the differential is defined as the absolute pressure when only liquid electrolyte was recirculating and the gas handling system was closed off from the electrolyzer, and the absolute pressure of the gas collection headspace when the liquid electrolyte was recirculating and the gas

collection headspace was open to the electrolyzer. The product analysis testing was conducted to determine how much gaseous product was produced from constant current electrolysis and concurrently drawn through the GDE and gas permeable membrane to be detected by the NDIR CO analyzer. The summary of the below results are that bubble point pressure can be a close, but slightly liberal estimate of liquid infiltration (or breakthrough) of the gas collection head space; and that a VAPR process CO_2 electrolyzer can reduce CO_2 and remove gaseous products from the liquid electrolyte at the GDE interface. The results together indicate proof of concept of a VAPR CO_2 electrolyzer, and together with an analysis of the design, areas for significant improvement in both electrolyzer and VAPR process improvement from the prototype presented here.

6.6.1 Pressure Testing

The performance of the electrolyzer with respect to pressure testing during three different tests is presented in Figure 37, Figure 38, and Figure 39. Throughout the duration of each test, various parameters are changed (electrolyte flow rate, back pressure control, and gas flow rate), and each test has a few configuration differences between one another. Each event is described in a table corresponding to each figure, and each configuration is described for the respective test in Table 14. During flow cell test (FCT) 3.0 and 4.0, electrolyte infiltration was forced by increasing P_{diff} until breakthrough was observed. During FCT 5.0, this condition was not forced, but rather P_{diff} was maintained within a range that would prevent electrolyte infiltration of the gas collection headspace. This was due to performing gaseous product analysis testing during electrochemical operation of the electrolyzer between c.a. 3200–5000 seconds.

Table 14. VAPR Electrolyzer Test Case Configurations

Test Case	Orientation	Sweep Gas Flow Rate (sccm)	AgNP Coating	Peristaltic Pump Setting	Electrolyte Infiltration?
FCT 3.0	Vertical	25	1 side	1–2	Yes
FCT 4.0	Vertical	15	2 sides	1–1.5	Yes
FCT 5.0	Horizontal	15-65	2 sides	1.2	No

6.6.1.1 Flow Cell Test 3.0

The pressure testing results of FCT 3.0 are presented in Figure 37, and the events numbered therein are described in Table 15. Electrolyte infiltration of the gas collection headspace was observed at $P_{diff,max}$ = 2.06 psid and was not subsequently observed after corrective actions.

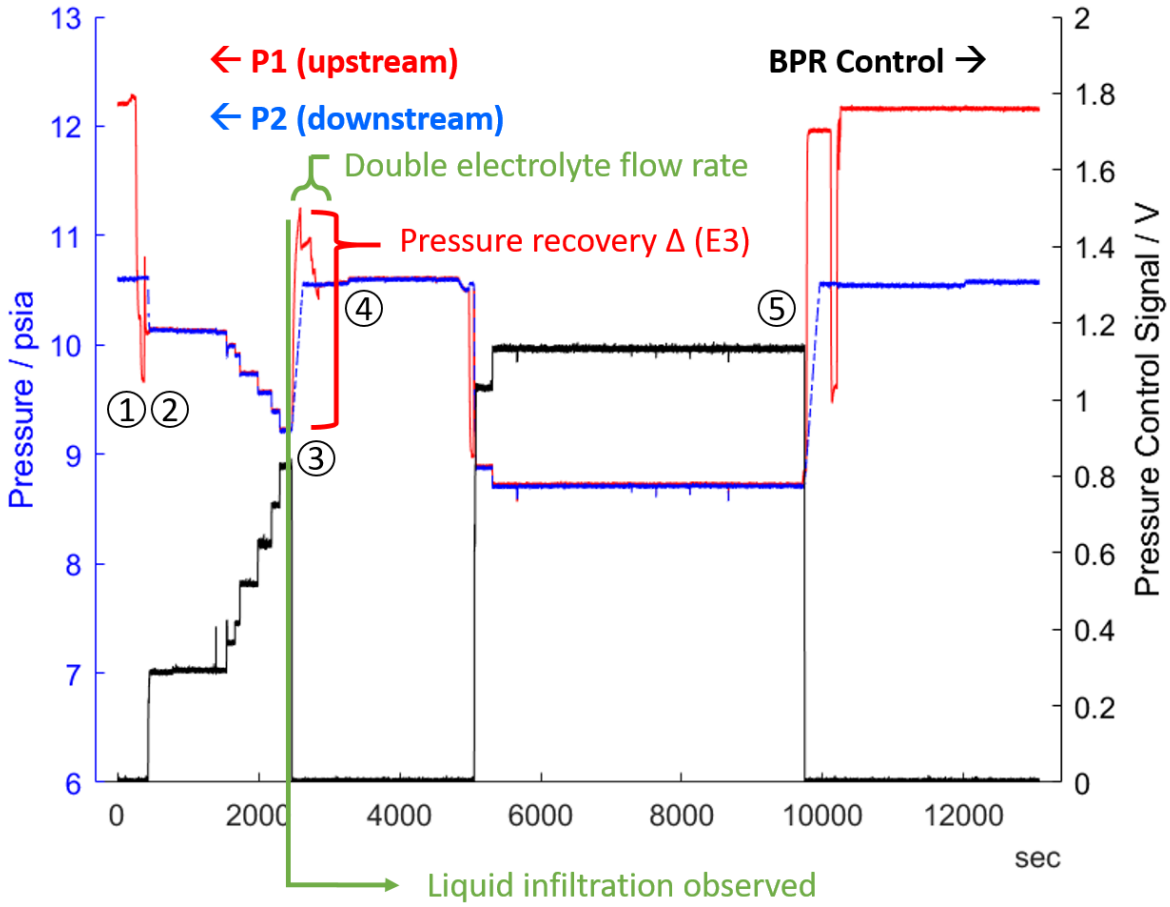

Figure 37. Plot of backpressure control and upstream (at the electrolyzer) and downstream (at the MS) pressure sensors in the gas handling subsystem (Test ID: FCT 3.0)

Table 15. Event Descriptions for FCT 3.0

Event #	Description
1	Electrolyte recirculation begins (PP=1), initial pressure = 9.6 psia
2	BPR control set to match P2 to P1, then valve to gas handling is immediately opened
3	Electrolyte infiltration observed, valve to gas handling immediately closed
4	Electrolyte recirculation rate is doubled (PP=2), gas valve is opened shortly after
5	End of test: (BPR is turned off, valve is closed, electrolyte recirculation is turned off)

6.6.1.2 Flow Cell Test 4.0

The pressure testing results of FCT 4.0 are presented in Figure 38, and the events numbered therein are described in Table 16. Electrolyte infiltration of the gas collection headspace was observed at $P_{diff,max}$ = 2.01 psid and after checking that corrective actions stopped the continued breakthrough, the test was ended.

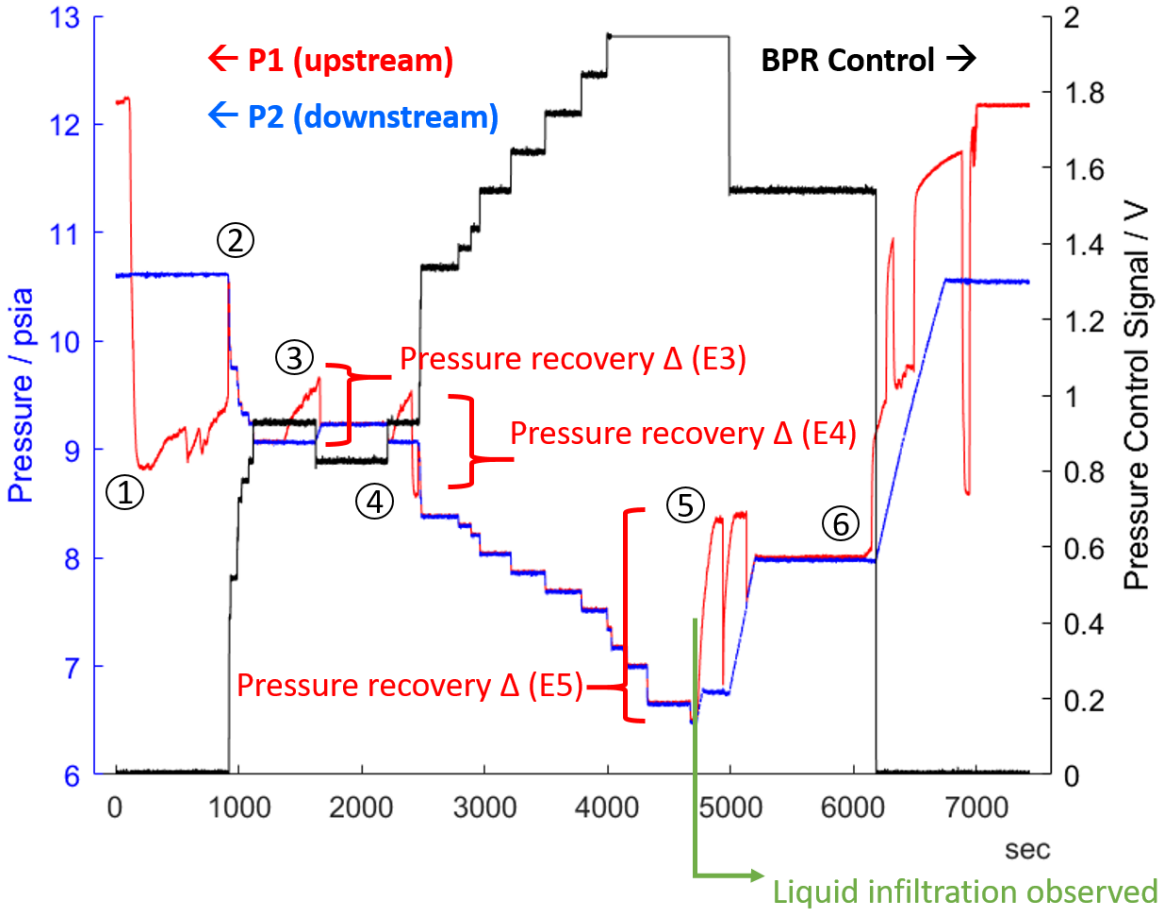

Figure 38. Plot of backpressure control and upstream (at the electrolyzer) and downstream (at the MS) pressure sensors in the gas handling subsystem (Test ID: FCT 4.0)

Table 16. Event Descriptions for FCT 4.0

Event #	Description
1	Electrolyte recirculation begins (PP=1.5) and then flow rate is reduced over time to (PP=1)
2	BPR control is set and valve to gas handling is opened
3	Valve to gas handling is closed to check recirculation-only pressure, then re-opened
4	Valve to gas handling is closed to check recirculation-only pressure, then re-opened
5	Electrolyte infiltration is observed, valve to gas handling is immediately closed
6	After steady state operation with no more infiltration is observed: End of test

6.6.1.3 Flow Cell Test 5.0

The pressure testing results of FCT 5.0 are presented in Figure 39, and the events numbered therein are described in Table 17. Electrolyte infiltration of the gas collection headspace was not induced nor observed. The test was conducted with the drying column and NDIR analyzer in-line, creating a greater line-loss pressure difference from P1 to P2.

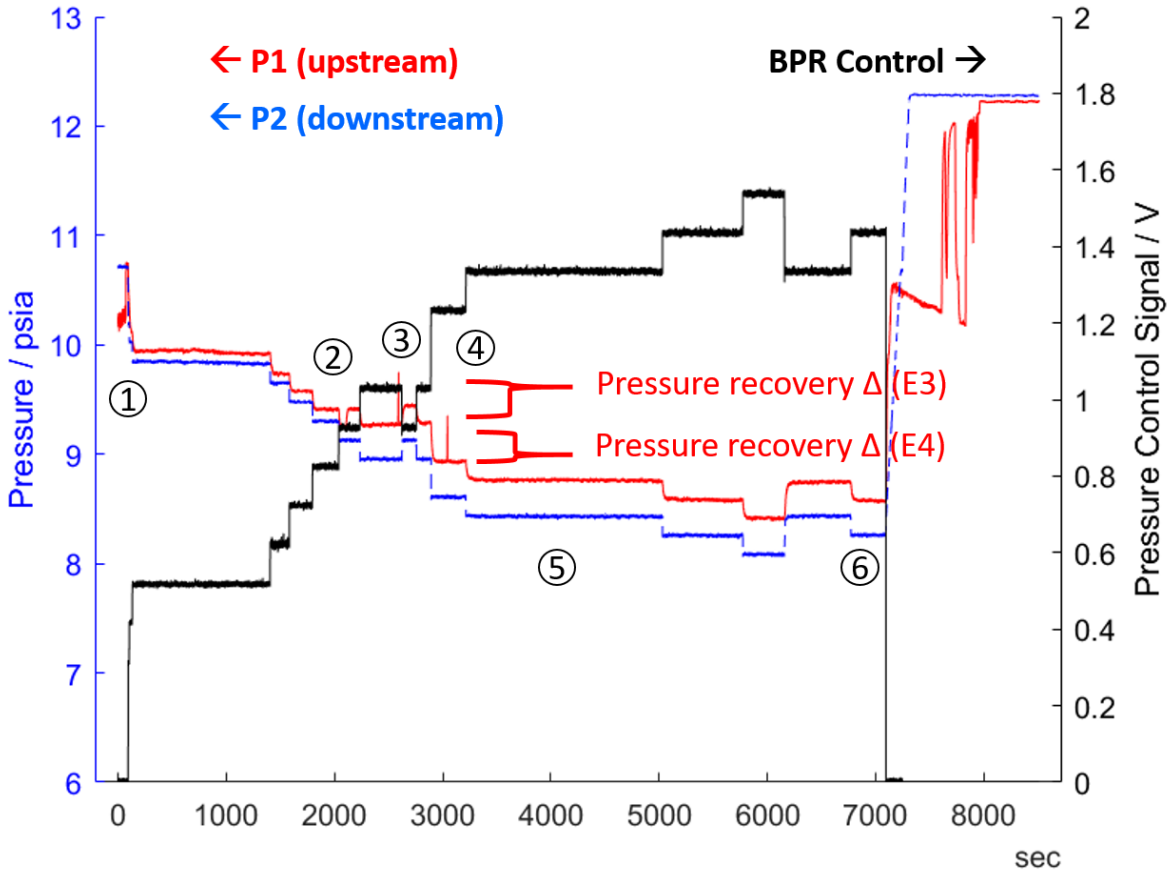

Figure 39. Plot of backpressure control and upstream (at the electrolyzer) and downstream (at the NDIR gas analyzer) pressure sensors in the gas handling subsystem (Test ID: FCT 5.0)

Table 17. Event Descriptions for FCT 5.0

Event #	Description
1	Electrolyte recirculation begins (PP=1.2), BPR is set, gas valve is opened (15 sccm Ar flow)
2	Sweep Ar flow is increased to 65 sccm (increased pressure difference P1 to P2 line-loss)
3	Valve to gas handling is closed to check recirculation-only pressure, then re-opened
4	Valve to gas handling is closed to check recirculation-only pressure, then re-opened
5	During this steady-state region, results from gas production analysis produced (Figure 40)
6	End of test: (BPR is turned off, valve is closed, electrolyte recirculation is turned off)

6.6.2 *Gaseous Product Analysis: Constant Current Electrolysis with VAPR*

Prior to FCT 5.0, an NDIR analyzer for CO and CH_4 was made available to enable analysis of CO produced at concentrations lower than the detection limit of the mass spectrometer and despite the presence of CO_2 that has mass spectra peaks at mass to charge (*m/z*) ratios of 12 and 28 which match the major mass spectra peaks of CO. The results presented in Figure 40 show the potential control of the working electrode and the measured CO versus time for a 10-minute (600 second) constant current electrolysis experiment (i = 400 mA, j_T = 16 mA cm^{-2}) conducted between approximately 3000−4000 seconds (1000 second duration in Figure 40) with respect to Figure 39.

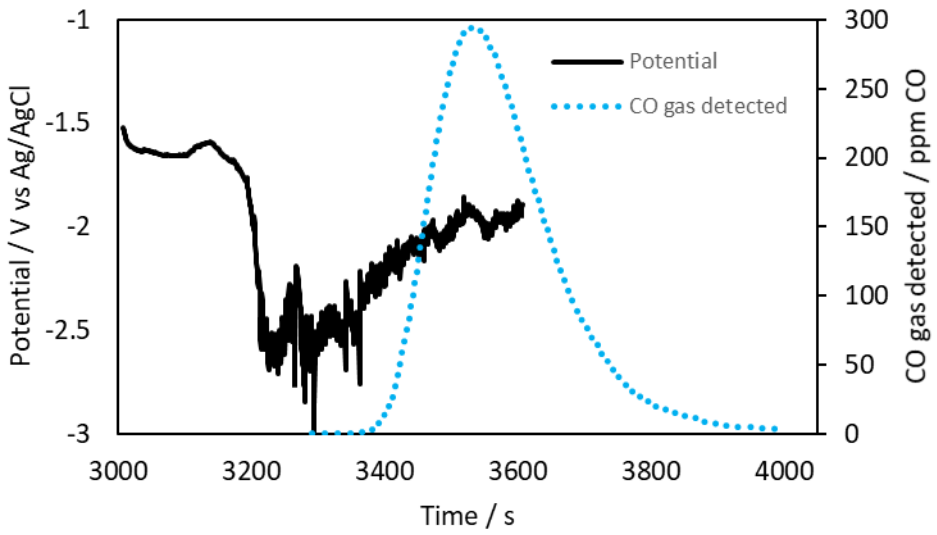

Figure 40. Potential of the working electrode during constant current control of the VAPR CO_2 electrolyzer and NDIR-measured CO concentration response

The potential reported in Figure 40 as measured with respect to the 3.4M KCl Ag/AgCl leak-free reference electrode, without compensating for *iR* drop or the junction potential of the reference electrode, which would be expected to shift the actual working electrode potential more positive after compensation. After multiplying the CO concentration with the time-averaged standard volumetric flow rate (86.6 sccm with σ = 0.35 sccm) and integrating the measured CO flow rate, it was determined that a total of 0.09 standard mL of CO was detected at the NDIR analyzer. The same was done for the *m/z = 2* signal for H_2,

which amounts to 0.34 standard mL of H_2 detected at the mass spectrometer. Comparing these detected amounts, the relative molar ratio of products for each can be calculated as 21% CO and 79% H_2.

To calculate actual faradaic efficiency for each, the current was integrated over time from the onset of a reducing potential for CO, c.a. 180 seconds, to the end of electrolysis at 600 seconds, totaling 167 C of charge passed during the 420 seconds of CO_2-reducing potential. This can be converted to total volume of 2-electron reduced product by combination of Faraday's law of electrolysis (Equation 18) and the ideal gas law, using Equation 29; which is then converted to standard volume using Equation 30.

$$V = \frac{\left(\int_{180}^{600} i\, dt\right)}{F*z}\frac{RT}{P_1} \tag{29}$$

$$V_{STP} = V\frac{T_{STP}}{T}\frac{P}{P_{STP}} \tag{30}$$

Where, V is the total volume of gas generated in m^3, $R = 8.314\ J\ mol^{-1}\ K^{-1}$ (ideal gas constant), $T = 301.15\ K$ (average temperature of gas at the analyzer), $P_1 = 60{,}535\ Pa$ (average pressure at the analyzer), $F = 96{,}485\ C\ mol^{-1}$, $z = 2$, $T_{STP} = 273.15\ K$, and $P_{STP} = 101{,}325\ Pa$.

These results show that the total 2-electron reduced product generated at the cathode, assuming all current was Faradaic and all products were gaseous, was 19.4 standard mL. Therefore, the **observed** Faradaic efficiencies of removed **and** analyzed gasses (i.e. not necessarily true Faradaic efficiencies due to VAPR process) are $FE_{obs,CO}$ = 0.5% and $FE_{obs,H2}$ = 1.75%. Other products (i.e. liquid or gas other than CH_4) or constituents in the gas stream (CO_2 coming out of solution or water vapor) were not analyzed. Caution should be taken in interpreting these results as quantitative truth due to the slow NDIR analyzer response rate at low flow rates described in the Experimental Methods section of Chapter 5 (Figure 22). As mentioned there and repeated here again, there was a 787 s delay between introduction of a calibration gas and the NDIR analyzer achieving 90% of its full-scale response. Given that the CO_2 reducing potential of Figure 40 occurs over 400 s, it is likely that a full-scale CO concentration was never measured, and that the amount of CO measured could be undermeasured by anywhere from 5−10 times its actual concentration.

6.7 Discussion

6.7.1 Pressure Testing

Pressure testing of the flow cell electrolyzer shows the fast response and controllability of the electrolyzer gas collection headspace to changes from the gas handling system, namely the backpressure regulator. Through the progressive series of tests, FCT 3.0 to 5.0, flow rates, backpressure, and orientation were varied to determine operating regimes that would maximize gas transport through the GDE and gas permeable membrane without exhibiting electrolyte infiltration of the gas collection headspace. In both vertical orientation test cases (FCT 3.0 and FCT 4.0), it appears that infiltration would occur at differential pressures of approximately 2 psid as measured by the difference between P1 pressure at breakthrough and P1 pressure after recovery with the gas handling system closed. It should be noted that the hydrostatic pressure at the bottom of the cathode compartment (5 cm height in vertical orientation) is estimated to be 0.1 psi, which could contribute to earlier onset of breakthrough than expected. Additionally, the application of a catalyst coating to the back side of the GDE did not appear to alter the maximum differential pressure before electrolyte breakthrough, comparing results from FCT 3.0 to FCT 4.0. While the additional coating (and therefore likely pore blocking of the GDE) may affect how much electrolyte can infiltrate behind the GDE and/or how freely it flows back and forth between the front and backside of the GDE, it is ultimately the gas permeable membrane that prevents electrolyte breakthrough into the gas collection headspace.

These results indicate that the bubble point pressure should be considered a liberal estimate of breakthrough pressure in this kind of electrolyzer, and a factor of 70% of $P_{B,IL}$ should be used, especially when there are uncertainties in the calculations from values, such as the shape factor and solid-liquid contact angle, which were estimated from similar ILs and materials. Such measurements should be considered in future work when designing an electrolyzer with a known IL, water concentration, and electrode, to better predict performance of the VAPR process.

During FCT 5.0, the P_{diff} never exceeded 1 psid, as checked by allowing pressure recovery of the gas collection headspace with the gas handling system closed off and only electrolyte recirculation acting to

affect the headspace pressure. A higher sweep gas flow rate was used to improve response time of the NDIR to a positive signal of CO during electrolysis tests. Because FCT 5.0 was conducted with the electrolyzer in a horizontal configuration, i.e. electrolyte flow through the cell is perpendicular to gravity, there is no hydrostatic pressure of the electrolyte acting on the GDE to help facilitate electrolyte breakthrough, as in the vertical configuration. Because breakthrough was not induced during FCT 5.0, it remains unclear if the breakthrough differential pressure would be the same from vertical to horizontal configurations.

6.7.2 Gaseous Product Analysis: Constant Current Electrolysis with VAPR

As seen in Figure 40, at potentials more positive than −1.5 V vs. Ag/AgCl, no CO production was observed from the VAPR process sampling of the CO_2 electrolyzer; this is expected based on CPE test results from Figure 24. The onset of CO production over the course of the flow cell experiment appears at c.a. −2.5 V vs. Ag/AgCl, well past the expected potential range of CO production in [emim][OTf] (−1.9 V to −1.7) from Figure 24, but the solution *iR* drop and the junction potential of the reference electrode were left uncompensated, making the required driven potential more negative in order to induce CO production. Shortly after the more negative potential is driven in the constant current electrolysis experiment shown in Figure 40, a positive signal for CO production and analysis at the NDIR analyzer is seen, which tapers off as the potential becomes more positive again. The cause of the delayed onset of the lower, CO_2-reducing potential is likely due to the need for pre-conditioning the silver nanoparticles on the gas diffusion electrode, i.e. reducing the silver oxides that formed after the electrode had been exposed to air. The gradual decrease in the magnitude of the reducing potential after onset of CO production is speculated to be due to either mass transport issues of CO_2 to the GDE surface, or possibly due to degradation of the near-GDE-surface IL electrolyte due to high current and insufficient more favorable reactant present at the electrode surface.

Quantifying the CO and H_2 production from this experiment leaves one to observe that either only a small amount of CO and H_2 were made (poor electrochemical performance) or only small amounts of CO and H_2 were removed and analyzed by the VAPR process and gas handling system. As mentioned previously, the concentration of CO measured is likely significantly underreported, so these results should

not be taken as quantitative truth. However, as a proof of concept, this experiment shows that the electrolyzer could reduce CO_2 and extract the reduced CO (as well as H_2 from HER) through the VAPR process for measurement or downstream use.

6.8 Summary of VAPR Process Experiments

After a review of the state of the art for CO_2 flow cell electrolysis and design options therein, an alternative concept to conventional CO_2 flow cell electrolyzer designs was formulated to address some concerns associated with operating a flow cell electrolyzer in spacecraft and habitat environments with associated requirements. A prototype of a vacuum-assisted product removal (VAPR) flow cell electrolyzer prototype and test bed were designed, fabricated, and tested in order to probe the feasibility of the design concept. By varying a small set of parameters (flow rates, backpressure, orientation, GDE catalyst coatings on one or both sides) with otherwise the same materials, the operational envelope of the electrolyzer was investigated. In a final test in the most likely favorable operational configuration for gaseous product analysis, constant current electrolysis was conducted to study the product generation and removal efficiency. While the test results do not appear to match expected results based on other studies in the literature and the H-cell measurements from Chapter 5, it is suspected that these asynchronous results may be due to sub-optimal design of the electrolyzer (large gaps between electrodes, no added supporting electrolyte, not leak tight due to insufficient compression) and issues with supporting equipment being used for out of specification operations (no *iR* compensation from potentiostat, gas flow rate to NDIR analyzer too slow for adequate full-scale response rate). Despite this, the VAPR process used in conjunction with CO_2 electrolysis was demonstrated to be capable of generating, removing, and analyzing gaseous products from CO_2 reduction. With this proof of concept, recommendations can be made for improving the process in future efforts.

6.8.1 Recommendations

Proving the stable, robust, reliable, and safe operation of a flow cell electrolyzer over a long period of time (i.e. operational life times on the order of years) is the goal of any continuous electrolysis process

reactor, but it is especially true when human life depends on it, as it would in the case of a CO_2 electrolyzer in spacecraft ECLSS architectures. While efforts overall in CO_2 flow electrolysis focus on that goal, there are more incremental improvements that need to be made to prototypes studying a VAPR process with CO_2 electrolysis in a flow cell. The following possible improvements and research avenues should be considered in any future work related to such electrolyzers.

Patterning of the flow field of the recirculating electrolyte can increase residence time of the electrolyte in the electrolyzer without reducing flow rate. This also increases the residence time of any entrained gaseous products to be in contact with the VAPR interface for longer, possibly improving product removal efficiency. By making the electrolyte chambers thinner (i.e. on the order of less than 1 mm thickness), the resistive losses through the cell will be significantly reduced to improve overall electrochemical performance. Thinner electrolyte layers will also aid with surface wetting of the electrolyte to the ion exchange membrane and the electrode material in a microgravity environment where capillary forces dominate, but if bubbles are introduced into the flow they may more easily become stagnated or stuck elsewhere in the system. Alternative GDLs, GDEs, and gas permeable membranes should be considered to determine if more optimal conditions for product removal rates, while avoiding electrolyte infiltration, can be achieved. GDEs such as porous, monolithic GDEs (such as nanoporous silver from Rosen, J. et al.) could improve cathode robustness by functioning as the catalyst and GDL without any carbon cloth support structure. With any GDL, GDE, and gas permeable membrane, long term testing should be conducted to observe if any fluid build-up between the cathode and gas permeable membrane occurs, and if so, if pulsing either the electrolyte recirculation rate higher or the vacuum pressure to create a pressure differential back into the electrolyte stream can back-infiltrate the electrolyte into the recirculation path.

In terms of general prototype improvements, professional fabrication of the electrolyzer should be sought out to reduce the possibility of leaks and maintain high precision at smaller scales (i.e. with thinner electrolyte chambers). External compression, similar to that seen in commercial fuel cell stacks, would provide an electrolyzer with better sealing, in addition to more compressible gaskets than expanded PTFE

gaskets. If silicone gaskets are used, they should be tested for compatibility with the specified IL to ensure no cracking, swelling, or other degradation of the material occurs after the material is exposed to IL solutions over long periods of time. Lastly, anion exchange and bi-polar membranes may prove to further enable a VAPR-style CO_2 electrolyzer design by allowing catholyte pH conditions that maintain higher concentration of CO_2 in the electrolyte while providing conditions conducive to CO_2 reduction; in addition to improving the oxygen evolution reaction at the anode, and thus the overall electrochemical performance.

6.9 Related Presentations and Publications:

Holquist, J. B., Klaus, D. M., Nabity, J. A., and Abney, M. B. (2016). Design of a Vacuum-Assisted Product Removal, Ionic Liquid-based, Carbon Dioxide Electrolyzer, ICES-2018-32, pp. 1–9.

Design of a Vacuum-Assisted Product Removal, Ionic Liquid-based, Carbon Dioxide Electrolyzer. *48th International Conference on Environmental Systems*, Albuquerque, NM, July 2018 (presentation).

Chapter 7 – Conclusions

7.1 Research Objectives

The research presented in this dissertation was focused on the following research objectives, which were presented in Chapter 1.

1. Analyze the performance requirements for an electrochemical CO_2 reduction system for various crewed space exploration mission scenarios and provide a first order estimate of the system sizing, power requirements, and the theoretical O_2 recovery efficiency of the different architectures
2. Identify, select, and synthesize or procure ionic liquids that may be conducive to supporting CO_2 electrolysis, and measure their relevant thermophysical properties in aqueous solutions
3. Parametrically characterize the influence of various ILs in aqueous solutions on the performance of solvated CO_2 electrolysis

4. Design and develop a prototype electrochemical reactor capable of operating in conditions relevant to supporting air revitalization needs of a crew in a space habitat
5. Analytically assess the challenges and opportunities of implementing an ECRS in various missions with relevant upstream and downstream processes and systems, with considerations for microgravity and low-gravity environments

7.2 Summary of Chapters

Chapter 1 served as an introduction to this dissertation, outlining the basic justification for the work, defining the research objectives that were addressed, providing an overview of the content of the chapters. Improvements in the recovery percentage of O_2 from metabolically generated CO_2 in spacecraft can reduce the cost and improve the sustainability of crewed space exploration missions. While other CO_2 reduction technologies are being investigated, solvated CO_2 electrolysis has been making gains in performance that warrant attention and investigation into applicability for spacecraft ECLSS.

Chapter 2 presented that background and state-of-the-art for CO_2 reduction considered for spacecraft ECLSS. In addition, the fundamentals of electrochemistry and a background on CO_2 electrolysis was provided with descriptions of the recent progress and state-of-the-art with solvated CO_2 electrolysis. The concept of using ILs to enable solvated CO_2 electrolysis was introduced with details on their effects and benefits in improving CO_2 reduction performance.

Chapter 3 focused on research objectives 1 and 5 by considering full-scale electrolyzer O_2 production performance requirements from the standpoint of meeting human metabolic needs. Generic electrolyzer configurations were presented to orient the reader, and then various application settings, such as in microgravity transit or on the surface of Mars were discussed. Numerous architecture configurations were detailed based on the desired CO_2 electrolysis process, the setting and environment of the architecture, as well as the purpose of the conceptual mission. These architectures included considerations of upstream and downstream systems to an electrochemical CO_2 reduction system in order to support the process, as well as

possible benefits and challenges to implementing the architectures. From these, the state-of-the-art performance data from CO_2 electrolyzers, and information about current ISS systems, reactor processing rates, system size, mass, and energy efficiency were estimated to a first degree in order to provide future system designers or technology developers some estimates with which to understand what an ECRS could look and perform like.

Chapter 4 addressed research objective 2 directly by presenting an in-depth discussion about the IL's role in CO_2 electrolysis, with conclusions that the cation of the IL is thought to affect CO_2 electrolysis, though through a few possible different reaction mechanisms. Given that product selective production rates for CO need to be improved to meet reasonable spacecraft application system sizes, the ILs selected for this study had variations in the base cation structure. These ILs were hypothesized to have a varied role in CO_2 electrolysis, whereby the cation influence could be further studied, helping to better understand design of ILs for supporting CO_2 electrolysis. Seven ILs were synthesized or procured and, as some had never been seen in literature before, fundamental thermophysical properties such as density, viscosity, and conductivity were experimentally characterized for the neat ILs and their binary solutions with water over the entire composition range.

Chapter 5 addresses research objective 3 through experimentally assessing CO_2 electrolysis at a silver electrode submerged in binary aqueous solutions of each IL and water. The performance of each IL for CO_2 reduction is investigated by cyclic voltammetry with the cell sparged with either argon (blank scan) or CO_2 to compare the current response of the system to CO_2-saturation. The IL-water solutions that showed evidence of promoting CO_2 reduction were further examined with constant potential electrolysis and gaseous product analysis to determine the reduced species produced at various potentials along the current wave for CO_2 reduction in the CVs. From these, it was apparent that imidazolium and pyrrolidinium cation-based ILs promoted CO_2 reduction at high faradaic yields for CO, and that pyrazolium can also promote a modest amount of CO production at low potentials. The dependence of the peak current of the reductive wave in aqueous [emim][OTf], [bmim][TFA], and [bmpyrr][TFA] solutions versus potential scan rate was

investigated in Randles-Sevcik analysis. The solubility of CO_2 in six neat ILs was measured and used to estimate the diffusion coefficient of CO_2 in the solutions with the Randles-Sevcik analysis.

Finally, Chapter 6 addressed research objectives 4 and 5, first with a discussion of the advantages and disadvantages of the most popular flow cell electrolysis configurations with respect to spaceflight applications. With an interest in addressing some of the challenges that would be posed by such configurations, an alternative concept is presented, vacuum-assisted product removal (VAPR) whereby CO_2 is introduced to the electrolyzer in solvated form and the gaseous reduction products are drawn through a gas diffusion electrode and gas permeable membrane to a downstream system. This process would have slower production rates per unit area of O_2 than electrolyzers that introduce high pressure CO_2 at the gas diffusion electrode, but it would benefit from high product purity of gaseous products, mitigation of bubble entrainment into the electrolyte flow (deterring two-phase fluid issues in microgravity environments), and in-situ gas-liquid separation. A prototype VAPR process CO_2 electrolyzer was designed along with a test bed to experimentally assess the concept. Through various tests presented in Chapter 5, it was proven that the VAPR process CO_2 electrolyzer concept works to some extent. Results indicate that optimization of a variety of parameters, including materials, flow rates, pressures, and electrolyzer design will be required to advance such a process towards feasible implementation.

7.3 Future Work

The area of research pertaining to electrochemical CO_2 reduction is an active area of research across the world, due to its potential for reducing CO_2 to products such as CO, CH_4, and liquid hydrocarbon fuels, especially with variable supply power sources like solar and wind renewable energies. As such, new catalysts, membrane formulations, solvents, electrolytes, and even electrolyzer designs are constantly being added to the literature on the subject. In general, the goals of these studies are to improve the current density, energy efficiency, and product selectivity of the electrochemical CO_2 reduction reaction with long term performance stability, which certainly also apply to spaceflight applications. The spaceflight community

should take note that even if CO_2 electrolysis is not yet commercially viable, i.e. capable of producing a commodity at a profit, they may still be viable for space applications.

Future work to enable the use of CO_2 electrolysis technology for space applications should consider optimized electrolyzer design based on best practices from commercial fuel cells and the long-term performance stability thereof. In many such devices, materials such as electrolyte, electrode, and membrane can be swapped out to study various reactor configurations and conditions. It should be noted that any spaceflight application CO_2 electrolyzer will likely need to utilize ionic liquids as, if nothing else, non-volatile CO_2 solvents that can be operated safely within a cabin atmosphere. Therefore, special consideration should be given to results in literature that show ILs with high CO_2 capacity and diffusivity that do not irreversibly capture CO_2, as they may further improve performance of CO_2 electrolysis if they have a wide enough potential window of electrochemical stability.

In addition to electrolyzer design advancements, the performance of CO_2 electrolyzers are approaching the point where consideration should start to be given to supporting systems that would work in conjunction with a CO_2 electrolyzer in a spacecraft ECLSS or ISRU architecture. Some of these considerations are presented in this dissertation, but future work could benefit from integration testing of electrolyzers with such supporting systems or modeling efforts to predict performance of various architectures enabled by an electrochemical CO_2 reduction system.

REFERENCES

Abney, M. B., Greenwood, Z. W., Miller, L. A., Alvarez, G., Iannantuono, M., & Jones, K. (2013). Methane Post-Processor Development to Increase Oxygen Recovery beyond State-of-the-Art Carbon Dioxide Reduction Technology. *43rd International Conference on Environmental Systems*, (AIAA 2013-3513), 1–11. https://doi.org/10.2514/6.2013-3513

Abney, M. B., & Mansell, J. M. (2010). The Bosch Process - Performance of a Developmental Reactor and Experimental Evaluation of Alternative Catalysts. *40th International Conference on Environmental Systems*, (AIAA 2010-6272), 1–21. https://doi.org/10.2514/6.2010-6272

Abney, M. B., & Mansell, J. M. (2011). Evaluation of Bosch-Based Systems Using Non-Traditional Catalysts at Reduced Temperatures. *41st International Conference on Environmental Systems*, (AIAA 2011-5059), 1–14. https://doi.org/doi:10.2514/6.2011-5059

Abney, M. B., Mansell, J. M., Atkins, B., Evans, C., & Nur, M. (2015). Advanced Oxygen Recovery via Series-Bosch Technology. *45th International Conference on Environmental Systems*, (ICES-2015-82), 1–16.

Abney, M. B., Mansell, J. M., Rabenberg, E., Marshall, N., Flight, S., Stanley, C. M., … Technology, J. (2014). Series-Bosch Technology For Oxygen Recovery During Lunar or Martian Surface Missions. *44th International Conference on Environmental Systems*, (ICES-2014-160), 1–14.

Abney, M. B., Mansell, M., DuMez, S., Thomas, J., Cooper, C., & Long, D. (2013). Ongoing Development of a Series Bosch Reactor System. *43rd International Conference on Environmental Systems*, (AIAA 2013-3512), 1–8. https://doi.org/10.2514/6.2013-3512

Abney, M. B., Miller, L. A., & Williams, T. (2010). Sabatier Reactor System Integration with Microwave Plasma Methane Pyrolysis Post-Processor for Closed-Loop Hydrogen Recovery. *40th International Conference on Environmental Systems*, (AIAA 2010-6274), 1–12. https://doi.org/10.2514/6.2010-6274

Alvarez-Guerra, M., Albo, J., Alvarez-Guerra, E., & Irabien, A. (2015). Ionic liquids in the electrochemical valorisation of CO2. *Energy Environ. Sci.*, *8*(9), 2574–2599. https://doi.org/10.1039/C5EE01486G

Anderson, J. L., Dixon, J. K., & Brennecke, J. F. (2007). Solubility of CO2, CH4, C2H6, C2H4, O2, and N2 in 1-hexyl-3-methylpyridinium bis(trifluoromethylsulfonyl)imide: Comparison to other ionic liquids. *Accounts of Chemical Research*, *40*(11), 1208–1216. https://doi.org/10.1021/ar7001649

Anderson, M. S., Ewert, M. K., Keener, J. F., & Wagner, S. A. (2015). *Advanced life support baseline values and assumptions document*. *NASA/TP-2015-218570*. https://doi.org/CTSD-ADV-484 A

Angell, C. A., Ansari, Y., & Zhao, Z. (2012). Ionic Liquids: Past, present and future. *Faraday Discuss.*, *154*(1), 9–27. https://doi.org/10.1039/C1FD00112D

Anthony, J. L., Anderson, J. L., Maginn, E. J., & Brennecke, J. F. (2005). Anion effects on gas solubility in ionic liquids. *J. Phys. Chem. B*, *109*(13), 6366–6374. https://doi.org/10.1021/jp046404l

Armand, M., Endres, F., MacFarlane, D. R., Ohno, H., & Scrosati, B. (2009). Ionic-Liquid Materials for the Electrochemical Challenges of the Future. *Nature Materials*, *8*(8), 621–629. https://doi.org/10.1038/nmat2448

Arquilla, K. S., Rundle, T., Shaffer, B., Phillips, D. D., Lampe, A., Denton, J., … Nabity, J. A. (2017). Characterization of Carbon Dioxide Removal using Ionic Liquids in Novel Geometries. *47th International Conference on Environmental Systems*, (ICES-2017-234), 1–14.

Asadi, M., Kim, K., Liu, C., Addepalli, A. V., Abbasi, P., Yasaei, P., … Salehi-Khojin, A. (2016). Nanostructured transition metal dichalcogenide electrocatalysts for CO2 reduction in ionic liquid. *Science*, *353*(6298), 467–470. https://doi.org/10.1126/science.aaf4767

Asadi, M., Kumar, B., Behranginia, A., Rosen, B. a, Baskin, A., Repnin, N., … Salehi-Khojin, A. (2014). Robust carbon dioxide reduction on molybdenum disulphide edges. *Nat. Com.*, *5*, 4470. https://doi.org/10.1038/ncomms5470

Barrosse-Antle, L. E., Bond, A. M., Compton, R. G., O'Mahony, A. M., Rogers, E. I., & Silvester, D. S. (2010). Voltammetry in room temperature ionic liquids: Comparisons and contrasts with conventional

electrochemical solvents. *Chemistry - An Asian Journal*, *5*(2), 202–230. https://doi.org/10.1002/asia.200900191

Barrosse-Antle, L. E., & Compton, R. G. (2009). Reduction of carbon dioxide in 1-butyl-3-methylimidazolium acetate. *Chemical Communications*, (25), 3744–3746. https://doi.org/10.1039/b906320j

Barton Cole, E., Lakkaraju, P. S., Rampulla, D. M., Morris, A. J., Abelev, E., & Bocarsly, A. B. (2010). Using a one-electron shuttle for the multielectron reduction of CO 2 to methanol: Kinetic, mechanistic, and structural insights. *Journal of the American Chemical Society*, *132*(33), 11539–11551. https://doi.org/10.1021/ja1023496

Berthod, A., Ruiz-Ángel, M. J., & Carda-Broch, S. (2008). Ionic liquids in separation techniques. *Journal of Chromatography A*, *1184*(1–2), 6–18. https://doi.org/10.1016/j.chroma.2007.11.109

Cao, Q., Lu, X., Wu, X., Guo, Y., Xu, L., & Fang, W. (2015). Density, viscosity, and conductivity of binary mixtures of the ionic liquid N -(2-hydroxyethyl)piperazinium propionate with water, methanol, or ethanol. *Journal of Chemical and Engineering Data*, *60*(3), 455–463. https://doi.org/10.1021/je500380x

Carroll, J., Slupsky, J., & Mather, A. (1991). The solubility of carbon dioxide in water at low pressure. *J. Phys. Chem. Ref. Data*. https://doi.org/10.1063/1.555900

Clare, B., Sirwardana, A., & MacFarlane, D. R. (2009). Synthesis, Purification, and Characterization of Ionic Liquids. In *Topics in Current Chemistry-Ionic Liquids* (pp. 1–40). https://doi.org/10.1007/128_2008_31

Clark, E. L., Singh, M. R., Kwon, Y., & Bell, A. T. (2015). Differential Electrochemical Mass Spectrometer Cell Design for Online Quantification of Products Produced during Electrochemical Reduction of CO2. *Analytical Chemistry*, *87*(15), 8013–8020. https://doi.org/10.1021/acs.analchem.5b02080

Cloud, D., Devin, M., Schneider, S., Roy, R., Bagdigian, R., & Erickson, R. (1999). ISS Oxygen Generation Design Status. *29th International Conference on Environmental Systems*, (SAE Technical Paper 1999-01-2116). https://doi.org/10.4271/1999-01-2116

Costentin, C., Canales, J. C., Haddou, B., & Saveant, J.-M. (2013). Electrochemistry of Acids on Platinum. Application to the Reduction of Carbon Dioxide in the Presence of Pyridinium Ion in Water. *Journal of the American Chemical Society*, *135*, 17671–17674. https://doi.org/10.1021/ja407988w

Costentin, C., Drouet, S., Robert, M., & Savéant, J. M. (2012). Turnover numbers, turnover frequencies, and overpotential in molecular catalysis of electrochemical reactions. Cyclic voltammetry and preparative-scale electrolysis. *Journal of the American Chemical Society*, *134*(27), 11235–11242. https://doi.org/10.1021/ja303560c

Costentin, C., Robert, M., & Savéant, J.-M. (2013). Catalysis of the electrochemical reduction of carbon dioxide. *Chemical Society Reviews*, *42*(6), 2423–2436. https://doi.org/10.1039/c2cs35360a

Costentin, C., Saveant, J.-M., & Tard, C. (2018). Catalysis of CO 2 Electrochemical Reduction by Protonated Pyridine and Similar Molecules. Useful Lessons from a Methodological Misadventure. *ACS Energy Letters*, *3*, 695–703. https://doi.org/10.1021/acsenergylett.8b00008

Daily, J. W. (2008). Molecular Dynamics Simulation of Ion Emission from Nanodroplets of Ionic Liquids. *Journal of Propulsion and Power*, *24*(5), 981–986. https://doi.org/Doi 10.2514/1.28762

Delacourt, C., Ridgway, P. L., Kerr, J. B., & Newman, J. (2008). Design of an Electrochemical Cell Making Syngas (CO + H2) from CO2 and H2O Reduction at Room Temperature. *Journal of The Electrochemical Society*, *155*(1), B42–B49. https://doi.org/10.1149/1.2801871

DiMeglio, J. L., & Rosenthal, J. (2013). Selective Conversion of CO_2 to CO with High Efficiency Using an Inexpensive Bismuth-Based Electrocatalyst. *Journal of the American Chemical Society*, *135*(24), 8798–8801. https://doi.org/10.1021/ja4033549

Drake, B. G., Hoffman, S. J., & Watts, K. D. (2013). *Human Exploration of Mars Design Reference Architecture 5.0*. *NASA/SP-2009-566-ADD*. https://doi.org/10.1109/AERO.2010.5446736

Dubois, M. R., & Dubois, D. L. (2009). Development of Molecular Electrocatalysts for CO2 Reduction and H2 Production/Oxidation. *Accounts of Chemical Research*, *42*(12), 1974–1982. https://doi.org/10.1021/ar900110c

Dubois, P., Marchand, G., Fouillet, Y., Berthier, J., Douki, T., Hassine, F., … Vaultier, M. (2006). Ionic liquid droplet as e-microreactor. *Analytical Chemistry*, *78*(14), 4909–4917. https://doi.org/10.1021/ac060481q

Ebbesen, S. D., Knibbe, R., & Mogensen, M. (2012). Co-Electrolysis of Steam and Carbon Dioxide in Solid Oxide Cells. *Journal of the Electrochemical Society*, *159*(8), F482–F489. https://doi.org/10.1149/2.076208jes

Eckart, P. (1996). *Spaceflight Life Support and Biospherics*. Springer.

Eisenmann, C. (2008). Bubble Point Testing and Micron Grade. Retrieved from http://www.chandeisenmann.com/tech_info/bubble_point.asp

FuelCellsEtc. (2018). FuelCellsEtc ELAT ® Gas Diffusion Layers. Retrieved from http://www.fuelcellsetc.com/store/DS/ELAT-Property-Sheet.pdf

Gatens, R. L., Anderson, M. S., Broyan, J. L., Macatangay, A. V, & Shull, S. A. (2015). National Aeronautics and Space Administration Environmental Control and Life Support Technology Development and Maturation for Exploration : 2014 to 2015 Overview. *45th International Conference on Environmental Systems*, (ICES-2015-111), 1–23.

Gentry, G. J., & Cover, J. (2015). International Space Station (ISS) Environmental Control and Life Support (ECLS) System Overview of Events: 2010 - 2014. *45th International Conference on Environmental Systems*, (ICES-2015-155), 1–12.

Graves, C. R. (2010a). Recycling CO2 into Sustainable Hydrocarbon Fuels : Electrolysis of CO2 and H2O, 245. https://doi.org/10.2475/ajs.281.3.299

Graves, C. R. (2010b). *Recycling CO2 into Sustainable Hydrocarbon Fuels: Electrolysis of CO2 and H2O*. Columbia University. https://doi.org/10.2475/ajs.281.3.299

Greenwood, Z. W., Abney, M. B., Perry, J. L., Miller, L. A., Dahl, R. W., Hadley, N. M., … Wheeler, R. R. (2015). Plasma Pyrolysis Technology and Metal Hydride Separation. *45th International Conference on Environmental Systems*, (ICES-2015-120), 1–13.

Grills, D. C., Matsubara, Y., Kuwahara, Y., Golisz, S. R., Kurtz, D. A., & Mello, B. A. (2014). Electrocatalytic CO2 Reduction with a Homogeneous Catalyst in Ionic Liquid: High Catalytic Activity at Low Overpotential. *The Journal of Physical Chemistry Letters*, *5*(11), 2033–2038. https://doi.org/10.1021/jz500759x

Habazaki, H., Yamasaki, M., Zhang, B.-P., Kawashima, A., Kohno, S., Takai, T., & Hashimoto, K. (1998). Co-methanation of carbon monoxide and carbon dioxide on supported nickel and cobalt catalysts prepared from amorphous alloys. *Applied Catalysis A: General*, *172*(1), 131–140. https://doi.org/10.1016/S0926-860X(98)00121-5

Hanioka, S., Maruyama, T., Sotani, T., Teramoto, M., Matsuyama, H., Nakashima, K., … Goto, M. (2008). CO2 separation facilitated by task-specific ionic liquids using a supported liquid membrane. *Journal of Membrane Science*, *314*(1–2), 1–4. https://doi.org/10.1016/j.memsci.2008.01.029

Hara, K., Kudo, A., & Sakata, T. (1995). Electrochemical reduction of carbon dioxide under high pressure on various electrodes in an aqueous electrolyte. *Journal of Electroanalytical Chemistry*, *391*(1–2), 141–147. https://doi.org/10.1016/0022-0728(95)03935-A

Haynes, W. M. (Ed.). (2014). *CRC Handbook of Chemistry and Physics* (95th ed.). CRC.

Hodgson, E., Guirgis, P., & Converse, D. (2013). Flexible Path Environmental Control and Life Support Technology – An Updated Look at Next Steps. *43rd International Conference on Environmental Systems*, (AIAA 2013-3409), 1–16.

Holbrey, J. D., & Seddon, K. R. (1999). Ionic Liquids. *Clean Technologies and Environmental Policy*, *1*(4), 223–236. https://doi.org/10.1007/s100980050036

Hori, Y. (2008). Electrochemical CO2 Reduction on Metal Electrodes. *Modern Aspects of Electrochemistry*, (42), 89–189. https://doi.org/10.1007/978-0-387-49489-0_3

Hori, Y., Kikuchi, K., & Suzuki, S. (1985). Production of CO and CH4 in electrochemical reduction of CO2 at metal electrodes in aqueous hydrogencarbonate solution. *Chemistry Letters*, (11), 1695–1698. https://doi.org/10.1246/cl.1985.1695

Hori, Y., Wakebe, H., Tsukamoto, T., & Koga, O. (1994). Electrocatalytic process of CO selectivity in

electrochemical reduction of CO2 at metal electrodes in aqueous media. *Electrochimica Acta*, *39*(11–12), 1833–1839. https://doi.org/10.1016/0013-4686(94)85172-7

Iacomini, C. S. (2011). Demonstration of a Stand-alone Solid Oxide Electrolysis Stack with Embedded Sabatier Reactors for 100% Oxygen Regeneration. *41st International Conference on Environmental Systems*, (AIAA 2011-5016), 1–13. https://doi.org/doi:10.2514/6.2011-5016

Iacomini, C. S., Benjamin, P., & Milobar, D. G. (2015). Feasibility Tests of Oxygen Recovery Technology as an Internally Reforming Regenerative Fuel Cell. *45th International Conference on Environmental Systems*, (ICES-2015-152), 1–14.

Iacomini, C. S., & Sridhar, K. R. (2005). Electrolyzer Power Requirements for Oxidizer Production on Mars. *Journal of Propulsion and Power*, *21*(6), 1062–1068. https://doi.org/10.2514/1.11029

Isenberg, A. (1989). Three-man Solid Electrolyte Carbon Dioxide Electrolysis Breadboard. *Report for NASA Research Center*.

Jhong, H. R. M., Ma, S., & Kenis, P. J. (2013). Electrochemical conversion of CO2 to useful chemicals: Current status, remaining challenges, and future opportunities. *Current Opinion in Chemical Engineering*, *2*(2), 191–199. https://doi.org/10.1016/j.coche.2013.03.005

Jhong, H. R. Q., Brushett, F. R., & Kenis, P. J. A. (2013). The effects of catalyst layer deposition methodology on electrode performance. *Advanced Energy Materials*, *3*(5), 589–599. https://doi.org/10.1002/aenm.201200759

Jones, H. W. (2011). Carbon Dioxide Reduction System Trade Studies. *41st International Conference on Environmental Systems*, (AISS 2011-5099), 1–12. https://doi.org/doi:10.2514/6.2011-5099

Jones, J. P., Prakash, G. K. S., & Olah, G. A. (2014). Electrochemical CO2 reduction: Recent advances and current trends. *Israel Journal of Chemistry*, *54*(10), 1451–1466. https://doi.org/10.1002/ijch.201400081

Jutz, F., Andanson, J. M., & Baiker, A. (2011). Ionic liquids and dense carbon dioxide: A beneficial biphasic system for catalysis. *Chemical Reviews*, *111*(2), 322–353. https://doi.org/10.1021/cr100194q

Kang, X., Zhu, Q., Sun, X., Hu, J., Zhang, J., Liu, Z., & Han, B. (2015). Highly efficient electrochemical reduction of CO2 to CH4 in an ionic liquid using a metal–organic framework cathode. *Chem. Sci.*, *00*, 1–8. https://doi.org/10.1039/C5SC03291A

Knox, J. C. (2000). International Space Station Carbon Removal Assembly Dioxide Testing. *30th International Conference on Environmental Systems*, (SAE Technical Paper 00ICES-234), 1–13.

Kondratenko, E. V., Mul, G., Baltrusaitis, J., Larrazabal, G. O., Perez-Ramirez, J., Larrazábal, G. O., & Pérez-Ramírez, J. (2013). Status and perspectives of CO2 conversion into fuels and chemicals by catalytic, photocatalytic and electrocatalytic processes. *Energy Environ. Sci.*, *6*(11), 3112. https://doi.org/10.1039/c3ee41272e

Korson, L., Drost-Hansen, W., & Millero, F. J. (1968). Viscosity of Water Various Temperatures. *The Journal of Physical Chemistry*, 34–39. https://doi.org/10.1021/j100721a006

Krossing, I., Slattery, J. M., Daguenet, C., Dyson, P. J., Oleinikova, A., & Weingärtner, H. (2006). Why are ionic liquids liquid? A simple explanation based on lattice and solvation energies. *Journal of the American Chemical Society*, *128*(41), 13427–13434. https://doi.org/10.1021/ja0619612

Kuhl, K. P., Hatsukade, T., Cave, E. R., Abram, D. N., Kibsgaard, J., & Jaramillo, T. F. (2014). Electrocatalytic Conversion of Carbon Dioxide to Methane and Methanol on Transition Metal Surfaces. *J. Am. Chem. Soc.*, *136*(40), 14107–14113. https://doi.org/10.1021/ja505791r

Kumar, B., Asadi, M., Pisasale, D., Sinha-Ray, S., Rosen, B. a, Haasch, R., … Salehi-Khojin, A. (2013). Renewable and metal-free carbon nanofibre catalysts for carbon dioxide reduction. *Nature Communications*, *4*, 2819. https://doi.org/10.1038/ncomms3819

Kumar, B., Brian, J. P., Atla, V., Kumari, S., Bertram, K. A., White, R. T., & Spurgeon, J. M. (2016). New trends in the development of heterogeneous catalysts for electrochemical CO2 reduction. *Catalysis Today*. https://doi.org/10.1016/j.cattod.2016.02.006

Kutz, R. B., Chen, Q., Yang, H., Sajjad, S. D., Liu, Z., & Masel, R. (2016). Sustainion™ Imidazolium Functionalized Polymers for CO2 Electrolysis. *Energy Technology*. https://doi.org/10.1002/ente.201600636

Lange, K. E., French, M. M., Abney, M. B., & Barta, D. J. (2018). Trading Advanced Oxygen Recovery Architectures and Technologies. *48th International Conference on Environmental Systems*, (July), 1–14.

Larson, W. J., & Pranke, L. K. (1999). *Human Spaceflight: Mission Analysis and Design*. (W. Larson & L. Pranke, Eds.) (1st ed.). McGraw-Hill Companies.

Lau, G. P. S., Schreier, M. R., Vasilyev, D., Scopelliti, R., Grätzel, M., & Dyson, P. J. (2016a). New Insights Into the Role of Imidazolium-based Promoters for the Electroreduction of CO2 on a Silver Electrode. *Journal of the American Chemical Society*, jacs.6b03366. https://doi.org/10.1021/jacs.6b03366

Lau, G. P. S., Schreier, M. R., Vasilyev, D., Scopelliti, R., Grätzel, M., & Dyson, P. J. (2016b). New Insights Into the Role of Imidazolium-based Promoters for the Electroreduction of CO2 on a Silver Electrode. *Journal of the American Chemical Society*, jacs.6b03366. https://doi.org/10.1021/jacs.6b03366

Lebegue, E., Agullo, J., & Belanger, D. (2018). Electrochemical Behavior of Pyridinium and N -Methyl Pyridinium Cations in Aqueous Electrolytes for CO2 Reduction. *ChemSusChem*, *11*, 219–228. https://doi.org/10.1002/cssc.201701745

Li, Y. C., Zhou, D., Yan, Z., Gonc, R. H., Salvatore, D. A., Berlinguette, C. P., & Mallouk, T. E. (2016). Electrolysis of CO2 to Syngas in Bipolar. *ACS Energy Letters*, *1*, 1149–1153. https://doi.org/10.1021/acsenergylett.6b00475

Lim, C.-H., Holder, A. M., Hynes, J. T., & Musgrave, C. B. (2014). Reduction of CO2 to Methanol Catalyzed by a Biomimetic Organo-Hydride Produced from Pyridine. *Journal of the American Chemical Society*, *136*(45), 16081–16095. https://doi.org/10.1021/ja510131a

Lim, C.-H., Holder, A. M., & Musgrave, C. B. (2013). Mechanism of Homogeneous Reduction of CO2 by Pyridine: Proton Relay in Aqueous Solvent and Aromatic Stabilization. *Journal of the American Chemical Society*, *135*(1), 142–154. https://doi.org/10.1021/ja3064809

Lin, P. Y., Soriano, A. N., Leron, R. B., & Li, M. H. (2011). Measurements and correlations of electrolytic conductivity and molar heat capacity for the aqueous ionic liquid systems containing [Emim][EtSO4] or [Emim][CF3SO3]. *Experimental Thermal and Fluid Science*, *35*(6), 1107–1112. https://doi.org/10.1016/j.expthermflusci.2011.03.005

Liu, W., Cheng, L., Zhang, Y., Wang, H., & Yu, M. (2008). The physical properties of aqueous solution of room-temperature ionic liquids based on imidazolium: Database and evaluation. *Journal of Molecular Liquids*, *140*(1–3), 68–72. https://doi.org/10.1016/j.molliq.2008.01.008

Liu, Z., Masel, R. I., Chen, Q., Kutz, R., Yang, H., Lewinski, K., … Lutz, D. R. (2015). Electrochemical generation of syngas from water and carbon dioxide at industrially important rates. *Journal of CO2 Utilization*, *15*, 50–56. https://doi.org/10.1016/j.jcou.2016.04.011

Manning, M. P. (1976). *An Investigation of the Bosch Process*. Massachusetts Institute of Technology.

Matsubara, Y., Grills, D. C., & Kuwahara, Y. (2015). Thermodynamic Aspects of Electrocatalytic CO2 Reduction in Acetonitrile and with an Ionic Liquid as Solvent or Electrolyte. *ACS Catalysis*, *5*(11), 6440–6452. https://doi.org/10.1021/acscatal.5b00656

McKellar, M. G., Wood, R. A., & Stoots, C. M. (2011). A Novel Approach To Maximize Waste Recovery in a Life Support System. *41st International Conference on Environmental Systems*, (AIAA 2011-5015), 1–16. https://doi.org/10.2514/6.2011-5015

McKellar, M., Stoots, C., Sohal, M., Mulloth, L., Luna, B., & Abney, M. B. (2010). The Concept and Analytical Investigation of CO2 and Steam Co-Electrolysis for Resource Utilization in Space Exploration. *40th International Conference on Environmental Systems*, (AIAA 2010-6273), 1–26. https://doi.org/10.2514/6.2010-6273

Medina-Ramos, J., DiMeglio, J. L., & Rosenthal, J. (2014). Efficient Reduction of CO2 to CO with High Current Density Using in Situ or ex Situ Prepared Bi-Based Materials. *Journal of the American Chemical Society*, *136*(23), 8361–8367. https://doi.org/10.1021/ja501923g

Medina-Ramos, J., Pupillo, R. C., Keane, T. P., Dimeglio, J. L., & Rosenthal, J. (2015). Efficient conversion of CO2 to CO using tin and other inexpensive and easily prepared post-transition metal catalysts. *Journal of the American Chemical Society*, *137*(15), 5021–5027. https://doi.org/10.1021/ja5121088

Mitlitsky, F., Myers, B., Weisberg, A. H., & A, L. (1999). Applications and Development of High Pressure

PEM Systems. *Portable Fuel Cells Conference*, (UCRL-JC-134539).
Moçoteguy, P., & Brisse, A. (2013). A review and comprehensive analysis of degradation mechanisms of solid oxide electrolysis cells. *International Journal of Hydrogen Energy*, *38*(36), 15887–15902. https://doi.org/10.1016/j.ijhydene.2013.09.045
Morgan, D., Ferguson, L., & Scovazzo, P. (2005). Diffusivities of gases in room-temperature ionic Liquids: Data and correlations obtained using a lag-time technique. *Industrial and Engineering Chemistry Research*, *44*(13), 4815–4823. https://doi.org/10.1021/ie048825v
Muscatello, A. C., & Santiago-Maldonado, E. (2012). Mars In Situ Resource Utilization Technology Evaluation. In *50th AIAA Aerospace Sciences Meeting Including the New Horizons Forum and Aerospace Exposition* (pp. 1–13). https://doi.org/10.2514/6.2012-360
Najafabadi, A. T. (2013). CO2 Chemical Conversion to Useful Products: An Engineering Insight to the Latest Advances Toward Sustainability. *International Journal of Energy Research*, *37*, 485–499. https://doi.org/10.1002/er.3021
NASA. (2018). Technology Readiness Levels. *NPR 7123.1B - Appendix E*, 1–4.
NASA Technology Roadmaps TA 6: Human Health, Life Support, and Habitation Systems. (2015), (May).
NASA Technology Roadmaps TA 7: Human Exploration Destination Systems. (2015), (May).
Neubauer, S. S., Krause, R. K., Schmid, B., Guldi, D. M., & Schmid, G. (2016a). Overpotentials and Faraday Efficiencies in CO2 Electrocatalysis-the Impact of 1-Ethyl-3-Methylimidazolium Trifluoromethanesulfonate. *Advanced Energy Materials*, *6*(9). https://doi.org/10.1002/aenm.201502231
Neubauer, S. S., Krause, R. K., Schmid, B., Guldi, D. M., & Schmid, G. (2016b). Overpotentials and Faraday Efficiencies in CO2 Electrocatalysis–the Impact of 1-Ethyl-3-Methylimidazolium Trifluoromethanesulfonate. *Advanced Energy Materials*, n/a-n/a. https://doi.org/10.1002/aenm.201502231
Neubauer, S. S., Schmid, B., Reller, C., Guldi, D. M., & Schmid, G. (2016). Alkalinity Initiated Decomposition of Mediating Imidazolium Ions in High Current Density CO2 Electrolysis. *ChemElectroChem*. https://doi.org/10.1002/celc.201600461
Noble, R. D., & Gin, D. L. (2011). Perspective on ionic liquids and ionic liquid membranes. *Journal of Membrane Science*, *369*(1–2), 1–4. https://doi.org/10.1016/j.memsci.2010.11.075
Ohno, H. (2005). *Electrochemical Aspects of Ionic Liquids*. (H. Ohno, Ed.). https://doi.org/10.4028/www.scientific.net/KEM.125-126.133
Ohno, H., & Yoshizawa, M. (2002). Ion conductive characteristics of ionic liquids prepared by neutralization of alkylimidazoles. *Solid State Ionics*, *154–155*, 303–309. https://doi.org/10.1016/S0167-2738(02)00526-X
Perry, J., Abney, M. B., Knox, J., Parrish, K., Roman, M., & Jan, D. (2014). Integrated Atmosphere Resource Recovery and Environmental Monitoring Technology Demonstration for Deep Space Exploration. *42nd International Conference on Environmental Systems*, (AIAA 2012-3585), 1–14.
Perry, J. L., Bagdigian, R. M., & Carrasquillo, R. L. (2010). Trade Spaces in Crewed Spacecraft Atmosphere Revitalization System Development. *40th International Conference on Environmental Systems*, (AIAA 2010-6061), 1–9. https://doi.org/AIAA 2010-6061
Perry, M. L., & Fuller, T. F. (2002). A Historical Perspective of Fuel Cell Technology in the 20th Century. *Journal of The Electrochemical Society*, *149*(7), 59–67. https://doi.org/10.1149/1.1488651
Qiao, J., Liu, Y., Hong, F., & Zhang, J. (2014). A review of catalysts for the electroreduction of carbon dioxide to produce low-carbon fuels. *Chemical Society Reviews*, *43*(2), 631–675. https://doi.org/10.1039/c3cs60323g
Reche, I., Gallardo, I., & Guirado, G. (2014). Electrochemical studies of CO2 in imidazolium ionic liquids using silver as a working electrode: a suitable approach for determining diffusion coefficients, solubility values, and electrocatalytic effects. *RSC Adv.*, *4*(110), 65176–65183. https://doi.org/10.1039/C4RA11297K
Rodríguez, H., & Brennecke, J. F. (2006). Temperature and composition dependence of the density and viscosity of binary mixtures of water + ionic liquid. *Journal of Chemical and Engineering Data*, *51*(6),

2145–2155. https://doi.org/10.1021/je0602824
Rosen, B. A., Salehi-khojin, A., Thorson, M. R., Zhu, W., Whipple, D. T., Kenis, P. J. A., & Masel, R. I. (2011). Ionic Liquid – Mediated Selective Conversion of CO2 to CO at Low Overpotentials. *Science*, *334*(6056), 643–644.
Rosen, B. A., Salehi-Khojin, A., Thorson, M. R., Zhu, W., Whipple, D. T., Kenis, P. J. a., & Masel, R. I. (2011). SUPPORT Ionic Liquid-Mediated Selective Conversion of CO2 to CO at Low Overpotentials. *Science*, *334*(6056), 643–644. https://doi.org/10.1126/science.1209786
Rosen, B. A., Zhu, W., Kaul, G., Salehi-khojin, A., Masel, R. I., Soc, J. E., … Salehi-khojin, A. (2013). Water Enhancement of CO2 Conversion on Silver in 1-Ethyl-3-Methylimidazolium Tetrafluoroborate, *160*(2). https://doi.org/10.1149/2.004303jes
Rosen, J. (2016). *Design of Electrolyzer for Carbon Dioxide Conversion to Fuels and Chemicals*. University of Deleware.
Samplatsky, D. J., Grohs, K., Edeen, M., Crusan, J., & Burkey, R. (2011). Development and Integration of the Flight Sabatier Assembly on the ISS. *41st International Conference on Environmental Systems*, (AIAA 2011-5151), 1–9. https://doi.org/doi:10.2514/6.2011-5151
Sanders, G. B. (2010). In-situ resource utilization on Mars - Update from DRA 5.0 Study. *48th AIAA Aerospace Sciences Meeting Including the New Horizons Forum and Aerospace Exposition*, (AIAA 2010-799), 1–12. https://doi.org/10.2514/6.2010-799
Sanders, G. B., Paz, A., Oryshchyn, L., Araghi, K., Muscatello, A. C., Linne, D. L., … Peters, T. (2015). Mars ISRU for Production of Mission Critical Consumables – Options, Recent Studies, and Current State of the Art. *SPACE Conferences and Exposition*, (AIAA 2015-4458), 1–14. https://doi.org/doi:10.2514/6.2015-4458
Schaezler, R. N., & Cook, A. J. (2015). Report on ISS O2 Production, Gas Supply & Partial Pressure Management. *45th International Conference on Environmental Systems*, (ICES-2015-146), 1–12.
Seddon, K. R., Stark, A., Torres, M.-J., Seddon, K. R., Stark, A., & Torres, M.-J. (2000). Influence of chloride, water, and organic solvents on the physical properties of ionic liquids. *Pure and Applied Chemistry* , *72*(12), 2275–2287. https://doi.org/10.1351/pac200072122275
Seo, S., Quiroz-guzman, M., Desilva, M. A., Lee, T. B., Huang, Y., Goodrich, B. F., … Brennecke, J. F. (2014). Chemically Tunable Ionic Liquids with Aprotic Heterocyclic Anion (AHA) for CO2 Capture. *The Journal of Physical Chemistry B*, (118), 5740–5751. https://doi.org/dx.doi.ord/10.1021/jp502279w
Shumar, J. W., See, G. G., Schubert, F. H., & Powell, J. D. (1976). *Solid Electrolyte Oxygen Regeneration System*, *NASA CR 137813*.
Smith, R. D. L., & Pickup, P. G. (2010). Nitrogen-rich polymers for the electrocatalytic reduction of CO2. *Electrochemistry Communications*, *12*(12), 1749–1751. https://doi.org/10.1016/j.elecom.2010.10.013
Soriano, A. N., Doma, B. T., & Li, M. (2009). Carbon dioxide solubility in 1-ethyl-3-methylimidazolium trifluoromethanesulfonate. *The Journal of Chemical Thermodynamics*, *41*(4), 525–529. https://doi.org/10.1016/j.jct.2008.11.001
Součková, M., Klomfar, J., & Pátek, J. (2011). Surface tension of 1-alkyl-3-methylimidazolium based ionic liquids with trifluoromethanesulfonate and tetrafluoroborate anion. *Fluid Phase Equilibria*, *303*(2), 184–190. https://doi.org/10.1016/j.fluid.2011.01.027
Sowmiah, S., Srinivasadesikan, V., Tseng, M. C., & Chu, Y. H. (2009). *On the chemical stabilities of ionic liquids*. *Molecules* (Vol. 14). https://doi.org/10.3390/molecules14093780
Spinner, N. S., Vega, J. A., & Mustain, W. E. (2012). Catalysis Science & Technology Recent progress in the electrochemical conversion and utilization of CO 2, 19–28. https://doi.org/10.1039/c1cy00314c
Sridhar, K. R., & Vaniman, B. T. (1997). Oxygen production on Mars using solid oxide electrolysis. *Solid State Ionics*, *93*, 321–328.
Stanley, C., Barnett, B., Matter, P., Beachy, M., Thompson, J., & Kelly, S. F. (2018). Alternative Carbon Formation Reactors for the Series-Bosch System. *48th International Conference on Environmental Systems*, (ICES-2018-22), 1–7.

Sun, L., Ramesha, G. K., Kamat, P. V., & Brennecke, J. F. (2014). Switching the Reaction Course of Electrochemical CO2 Reduction with Ionic Liquids. *Langmuir*, *30*(21), 6302–6308. https://doi.org/10.1021/la5009076

Sung, J., Jeon, Y., Kim, D., Iwahashi, T., & Iimori, T. (2005). Air – liquid interface of ionic liquid + H2O binary system studied by surface tension measurement and sum-frequency generation spectroscopy. *Chemical Physics Letters*, *406*, 495–500. https://doi.org/10.1016/j.cplett.2005.03.036

Swickrath, M. J., & Anderson, M. S. (2012). The Development of Models for Carbon Dioxide Revitalization. *42nd International Conference on Environmental Systems*, (AIAA 2012-3586), 1–19.

Takada, K. C., Ghariani, A. E., & Van Keuren, S. (2015). Advancing the Oxygen Generation Assembly Design to Increase Reliability and Reduce Costs for a Future Long Duration Mission. *45th International Conference on Environmental Systems*, (ICES-2015-115), 1–16.

Takada, K., Ghariani, A. E., Keuren, S. Van, Owens, A. C., Control, E., Activity, E. V., … Branch, S. (2018). Oxygen Generation Assembly Design for Exploration Missions. *48th International Conference on Environmental Systems*, (ICES-2018-113), 1–15.

Tanner, E. E. L., Batchelor-McAuley, C., & Compton, R. G. (2016). Carbon Dioxide Reduction in Room Temperature Ionic Liquids: The Effect of the Choice of Electrode Material, Cation, and Anion. *The Journal of Physical Chemistry C*, acs.jpcc.6b10564. https://doi.org/10.1021/acs.jpcc.6b10564

Tenney, C. M., Massel, M., Mayes, J. M., Sen, M., Brennecke, J. F., & Maginn, E. J. (2014). A computational and experimental study of the heat transfer properties of nine different ionic liquids. *Journal of Chemical and Engineering Data*, *59*(2), 391–399. https://doi.org/10.1021/je400858t

Tornow, C. E., Thorson, M. R., Ma, S., Gewirth, A. A., & Kenis, P. J. A. (2012). Nitrogen-Based Catalysts for the Electrochemical Reduction of CO $_2$ to CO. *Journal of the American Chemical Society*, *134*(48), 19520–19523. https://doi.org/10.1021/ja308217w

Uerdingen, M., Treber, C., Balser, M., Schmitt, G., & Werner, C. (2005). Corrosion behaviour of ionic liquids. *Green Chemistry*, *7*(5), 321–325. https://doi.org/10.1039/b419320m

Vermaas, D. A., & Smith, W. A. (2016). Synergistic Electrochemical CO2 Reduction and Water Oxidation with a Bipolar Membrane. *ACS Energy Letters*, *1*(6), 1143–1148. https://doi.org/10.1021/acsenergylett.6b00557

Wang, G., Pan, J., Ping, S., & Yang, H. (2018). Gas phase electrochemical conversion of humidified CO2 to CO and H2 on proton-exchange and alkaline anion-exchange membrane fuel cell reactors. *Journal of CO2 Utilization*, *23*, 152–158. https://doi.org/10.1016/j.jcou.2017.11.010

Wang, Y., Hatakeyama, M., Ogata, K., & Wakabayashi, M. (2015). Activation of CO2 by ionic liquid EMIM – BF4 in the electrochemical system: a theoretical study. *Physical Chemistry Chemical Physics*, *17*, 23521–23531. https://doi.org/10.1039/C5CP02008E

Weekes, D. M., Salvatore, D. A., Reyes, A., Huang, A., & Berlinguette, C. P. (2018). Electrolytic CO2 Reduction in a Flow Cell. *Acc. Chem. Res.*, *51*, 910–918. https://doi.org/10.1021/acs.accounts.8b00010

Whipple, D. T., Finke, E. C., & Kenis, P. J. A. (2010). Microfluidic Reactor for the Electrochemical Reduction of Carbon Dioxide : The Effect of pH. *Electrochemical and Solid State Letters*, *13*(9), B109–B111. https://doi.org/10.1149/1.3456590

Wickham, D. T., Gleason, K. J., Engel, J. R., & Systems, R. (2015). Continued Advancement of Supported Liquid Membranes for Carbon Dioxide Control in Extravehicular Activity Applications. *45th International Conference on Environmental Systems*, (ICES-2015-164), 1–15.

Wu, J., Yadav, R. M., Liu, M., Sharma, P. P., Tiwary, C. S., Ma, L., … Ajayan, P. M. (2015). Achieving Highly Efficient, Selective, and Stable CO $_2$ Reduction on Nitrogen-Doped Carbon Nanotubes. *ACS Nano*, *9*(5), 5364–5371. https://doi.org/10.1021/acsnano.5b01079

Yamamoto, T., Tryk, D. A., Fujishimal, A., & Ohata, H. (2002). Production of syngas plus oxygen from CO2 in a gas-diffusion electrode-based electrolytic cell. *Electrochimica Acta*, *47*(20), 3327–3334. https://doi.org/10.1016/S0013-4686(02)00253-0

Zakrzewska, M. E., & Nunes Da Ponte, M. (2018). Influence of Water on the Carbon Dioxide Solubility in [OTf]- and [eFAP]-Based Ionic Liquids. *Journal of Chemical and Engineering Data*, *63*(4), 907–912.

https://doi.org/10.1021/acs.jced.7b00521
Zhan, Z., & Zhao, L. (2010). Electrochemical reduction of CO2 in solid oxide electrolysis cells. *Journal of Power Sources*, *195*(21), 7250–7254. https://doi.org/10.1016/j.jpowsour.2010.05.037
Zhang, X., O'Brien, J. E., O'Brien, R. C., Hartvigsen, J. J., Tao, G., & Housley, G. K. (2013). Improved durability of SOEC stacks for high temperature electrolysis. *International Journal of Hydrogen Energy*, *38*(1), 20–28. https://doi.org/10.1016/j.ijhydene.2012.09.176
Zhao, S.-F., Horne, M., Bond, A. M., & Zhang, J. (2016). Is the Imidazolium Cation a Unique Promoter for Electrocatalytic Reduction of Carbon Dioxide? *The Journal of Physical Chemistry C*, *120*(42), 23989–24001. https://doi.org/10.1021/acs.jpcc.6b08182
Zhou, T., Chen, L., Ye, Y., Chen, L., Qi, Z., Freund, H., & Sundmacher, K. (2012). An overview of mutual solubility of ionic liquids and water predicted by COSMO-RS. *Industrial and Engineering Chemistry Research*, *51*(17), 6256–6264. https://doi.org/10.1021/ie202719z

APPENDICIES

APPENDIX A: SUMMARY OF PUBLICATIONS AND PRESENTATIONS

Holquist, J. B., Klaus, D. M., Nabity, J. A., and Abney, M. A. (2015). Opportunities and Challenges for Direct Oxygen Generation using Electrochemical Carbon Dioxide Reduction Catalyzed by Room Temperature Ionic Liquids (poster, 2nd place), *45th International Conference on Environmental Systems*, Bellevue, WA.

Holquist, J. B., Klaus, D. M., Nabity, J. A., and Abney, M. A. (2016). Electrochemical Carbon Dioxide Reduction with Room Temperature Ionic Liquids for Space Exploration Missions, ICES-2016-314, pp. 1–19.

Holquist, J. B., Klaus, D. M., Nabity, J. A., and Abney, M. B. (2016). Ionic Liquid Selection and Initial Test Results for Electrochemical Carbon Dioxide Reduction (poster, 1st place), *46th International Conference on Environmental Systems*, Vienna, Austria, July 2016.

Electrochemical Carbon Dioxide Reduction with Room Temperature Ionic Liquids for Space Exploration Missions. *46th International Conference on Environmental Systems* (ICES), Vienna Austria, July 2016 (presentation)

Holquist, J. B., Klaus, D. M., Nabity, J. A., and Abney, M. B. (2016). Design of a Vacuum-Assisted Product Removal, Ionic Liquid-based, Carbon Dioxide Electrolyzer, ICES-2018-32, pp. 1–9.

Design of a Vacuum-Assisted Product Removal, Ionic Liquid-based, Carbon Dioxide Electrolyzer. *48th International Conference on Environmental Systems*, Albuquerque, NM, July 2018 (presentation).

Holquist, J. B., Paley, M. S., and Klaus, D. M. (20XX). Density, Viscosity, and Conductivity of Seven Binary Mixtures of N-Heterocycle Cation-Varied Ionic Liquids and Water. [In Preparation – Working Title].

Holquist, J. B., and Klaus, D.M. (20XX). Experimental Evaluation of Trifluoroacetate Ionic Liquids with 7 Varied N-Heterocycle Cations for Electrochemical Reduction of Carbon Dioxide in Aqueous Solutions at Silver Electrodes. [In Preparation – Working Title].

APPENDIX B: FITTING COEFFICIENTS

Table 18. Redlich-Kister fitting equation coefficients for correlating the excess molar volume V^E ($cm^3 \cdot mol^{-1}$) for the binary mixtures of water (x_1) and each ionic liquid ($1-x_1$).

T / K	A_0	A_1	A_2	A_3	A_4
H_2O + [bmpyrr][TFA]					
296.2	-2.296	1.043	-0.230	1.694	-0.749
H_2O + [bmpy][TFA]					
295.0	-2.695	1.152	-0.530	2.387	-1.402
H_2O + [bmpz][TFA]					
296.2	-1.518	0.579	-0.978	2.032	0.248
H_2O + [bmim][TFA]					
294.6	-3.030	0.697	0.600	0.251	-1.387
H_2O + [bm3tri][TFA]					
294.7	-1.671	1.268	0.299	1.137	-3.373
H_2O + [bm4tri][TFA]					
295.7	-1.487	1.793	-0.824	1.751	-3.199
H_2O + [emim][OTf]					
295.4	0.285	0.438	0.201	0.357	-1.339

Table 19. Casteel-Amis fitting equation coefficients for correlating the conductivity κ ($mS \cdot cm^{-1}$) for the binary mixtures water (x_1) and each ionic liquid ($1-x_1$). Note that the x_{max} in the fit from Equation 5 is the molar fraction of the IL.

T / K	a	b	x_{max} at κ_{max}	κ_{max}
H_2O + [bmpyrr][TFA]				
296.2	0.386	4.075	0.054	23.967
H_2O + [bmpy][TFA]				
295.0	0.330	3.995	0.045	27.123
H_2O + [bmpz][TFA]				
296.2	0.402	3.493	0.055	31.737
H_2O + [bmim][TFA]				
294.6	0.420	3.198	0.065	28.004
H_2O + [bm3tri][TFA]				
294.7	0.430	3.081	0.064	32.949
H_2O + [bm4tri][TFA]				
295.7	0.407	3.502	0.055	35.468
H_2O + [emim][OTf]				
295.4	0.428	1.602	0.102	36.619

Table 20. Redlich-Kister fitting equation coefficients for correlating the excess viscosity Δη (mPa·s) for the binary mixtures of water (x_1) and each ionic liquid ($1-x_1$). Standard deviations ($cm^3 \cdot mol^{-1}$) are also presented.

T / K	A_0	A_1	A_2	A_3	A_4
H_2O + [bmpyrr][TFA]					
295.5	-33.27	0.86	-1.36	14.68	0.83

H_2O + [bmpy][TFA]					
295.1	-35.31	29.07	16.57	-21.15	-17.51
H_2O + [bmpz][TFA]					
296.3	-152.77	-71.76	-4.72	8.73	-18.72
H_2O + [bmim][TFA]					
296.0	-43.09	13.89	27.67	-21.23	-33.74
H_2O + [bm3tri][TFA]					
295.2	-59.86	-15.11	-19.33	-7.53	21.17
H_2O + [bm4tri][TFA]					
296.2	-91.55	-24.05	19.25	13.98	-1.28
H_2O + [emim][OTf]					
295.2	-43.81	-19.98	-11.53	-15.43	10.92

APPENDIX C: NMR Spectra

NMR Spectra of 1-ethyl-3-methylimidazolium trifluoromethanesulfonate, [emim][OTf], in D_2O

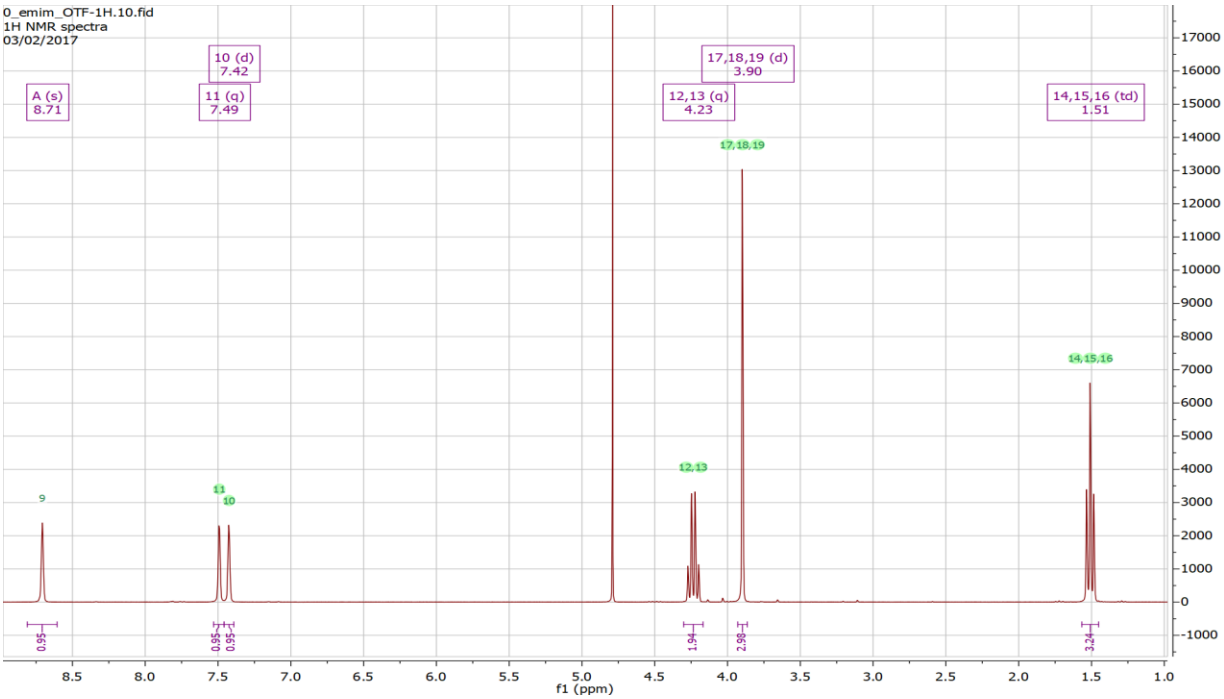

Figure 41. ^{1}H NMR spectrum of [emim][OTf] in D_2O

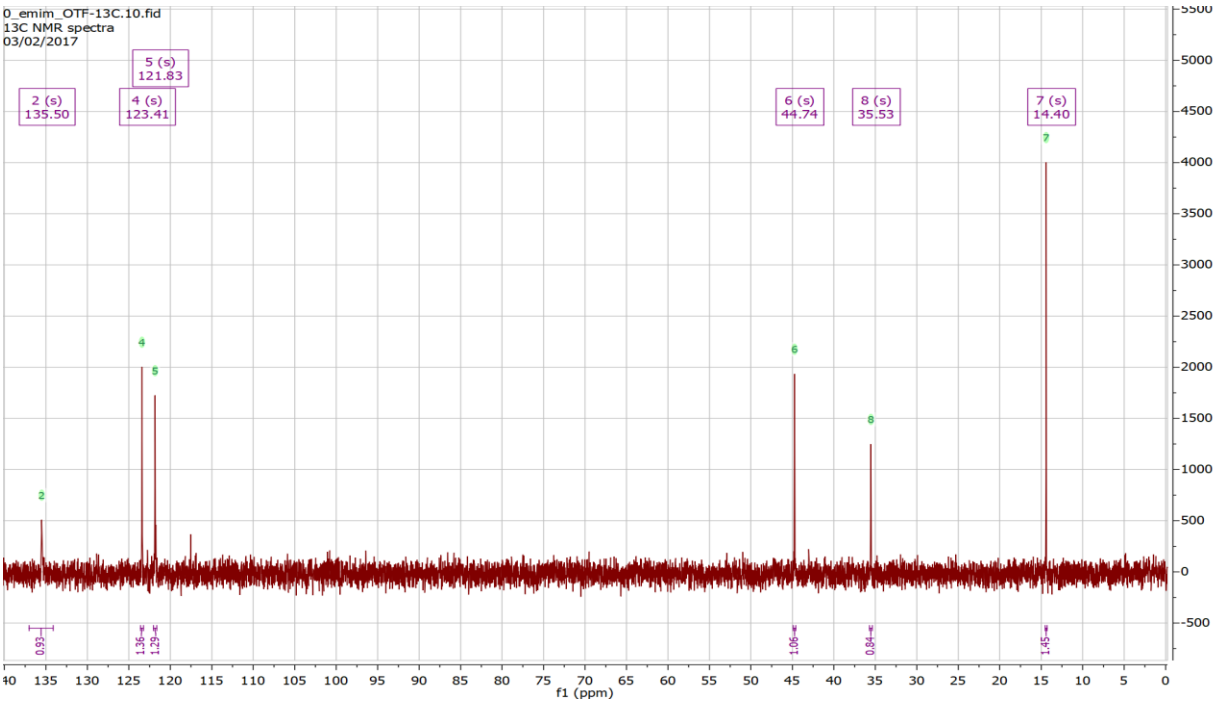

Figure 42. ^{13}C NMR spectrum of [emim][OTf] in D_2O

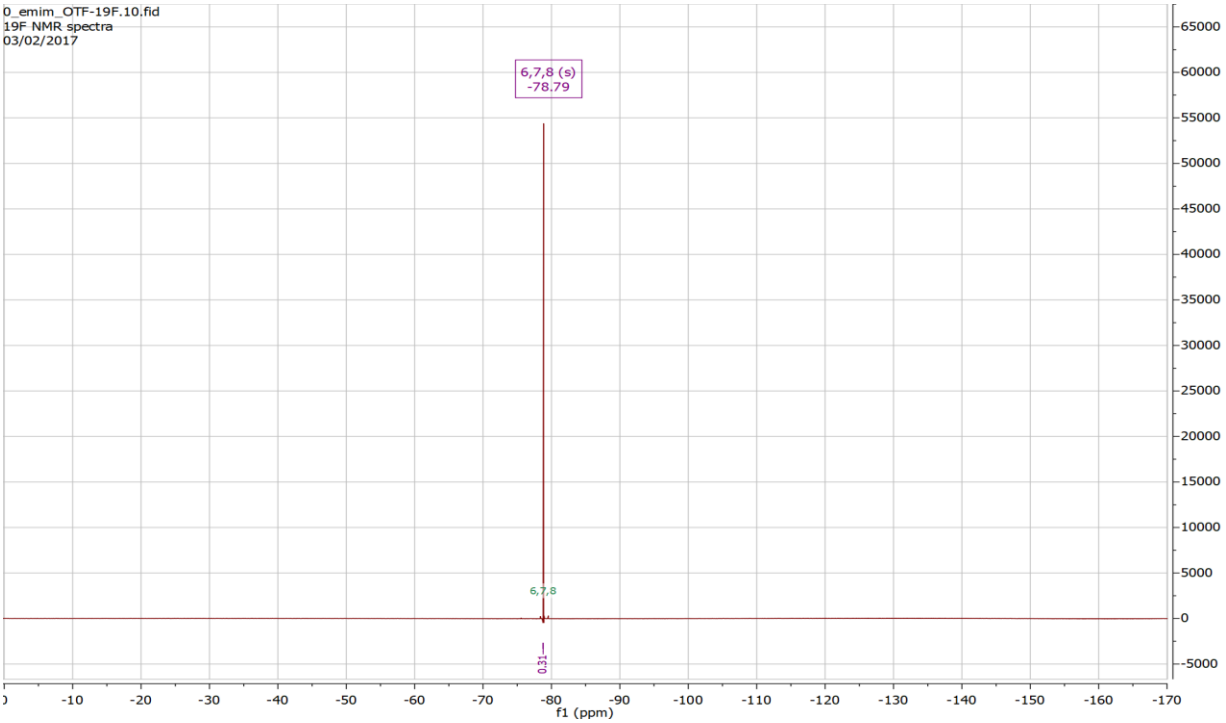

Figure 43. ^{19}F NMR spectrum of [emim][OTf] in D_2O

NMR Spectra of 1-butyl-1-methylpyrrolidinium trifluoroacetate, [bmpyrr][TFA], in D_2O

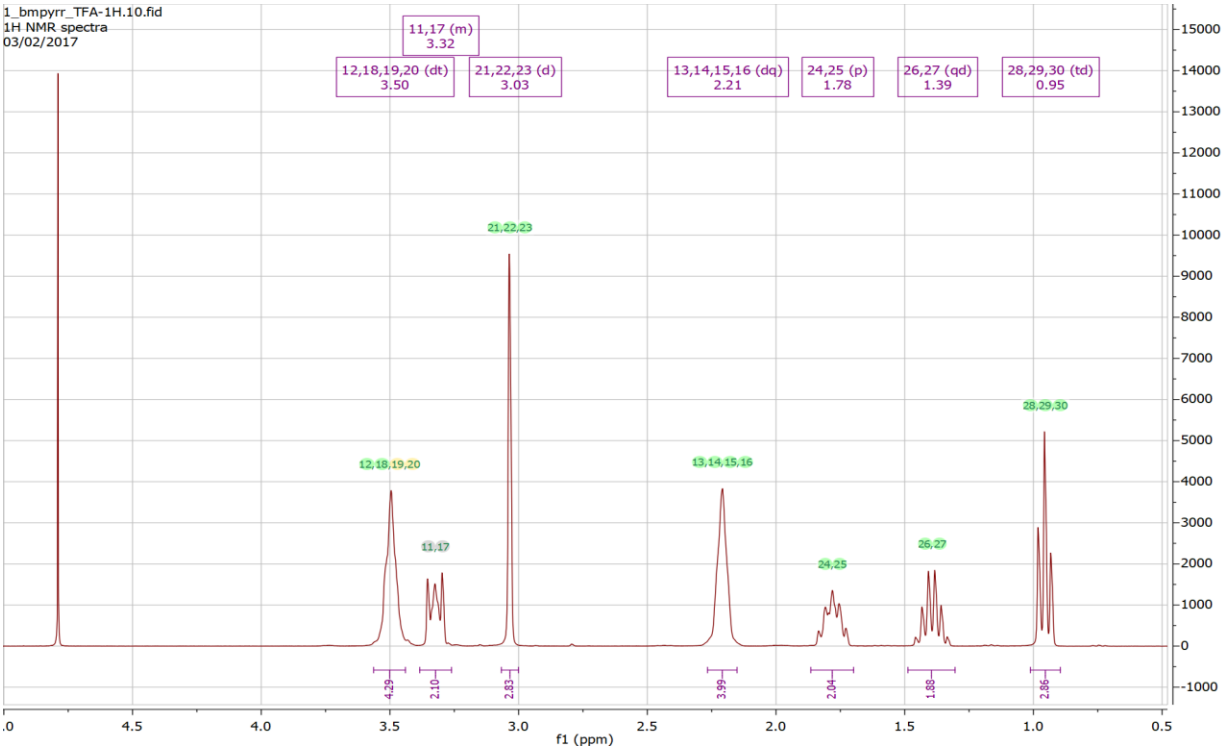

Figure 44. ^{1}H NMR spectrum of [bmpyrr][TFA] in D_2O

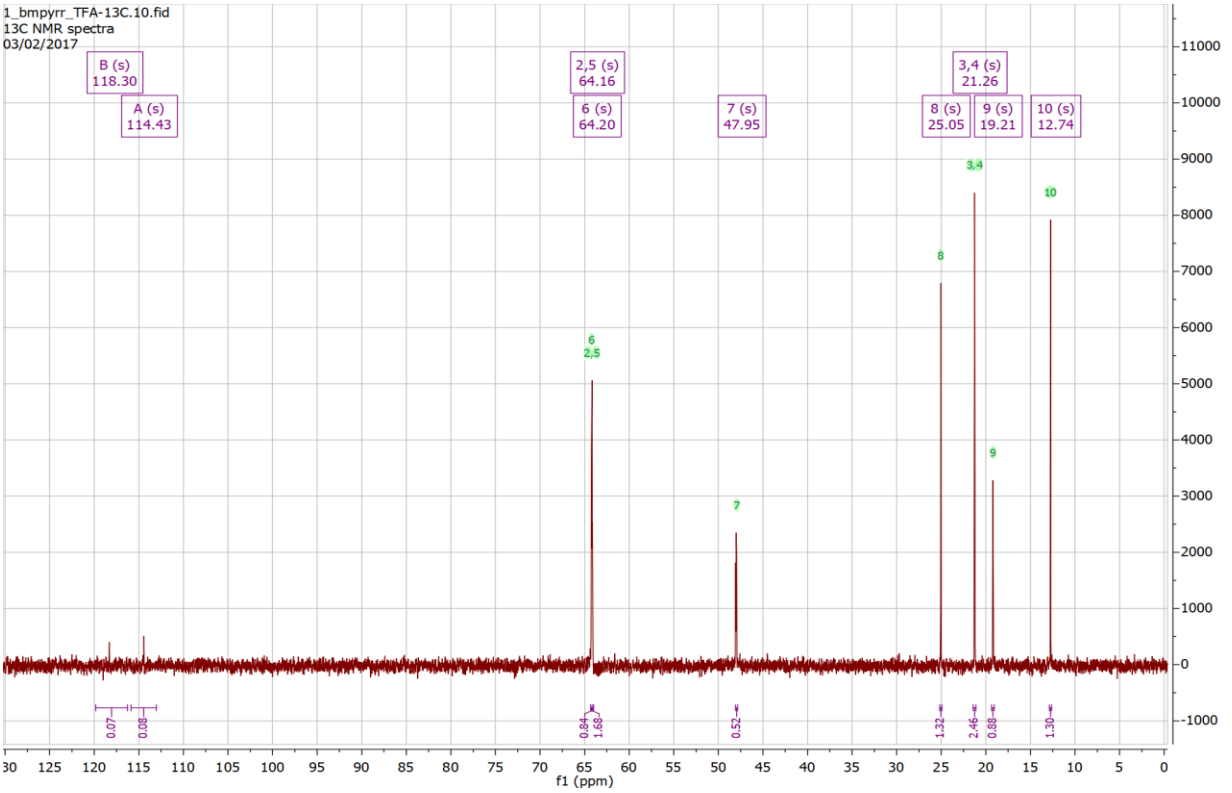

Figure 45. ^{13}C NMR spectrum of [bmpyrr][TFA] in D_2O

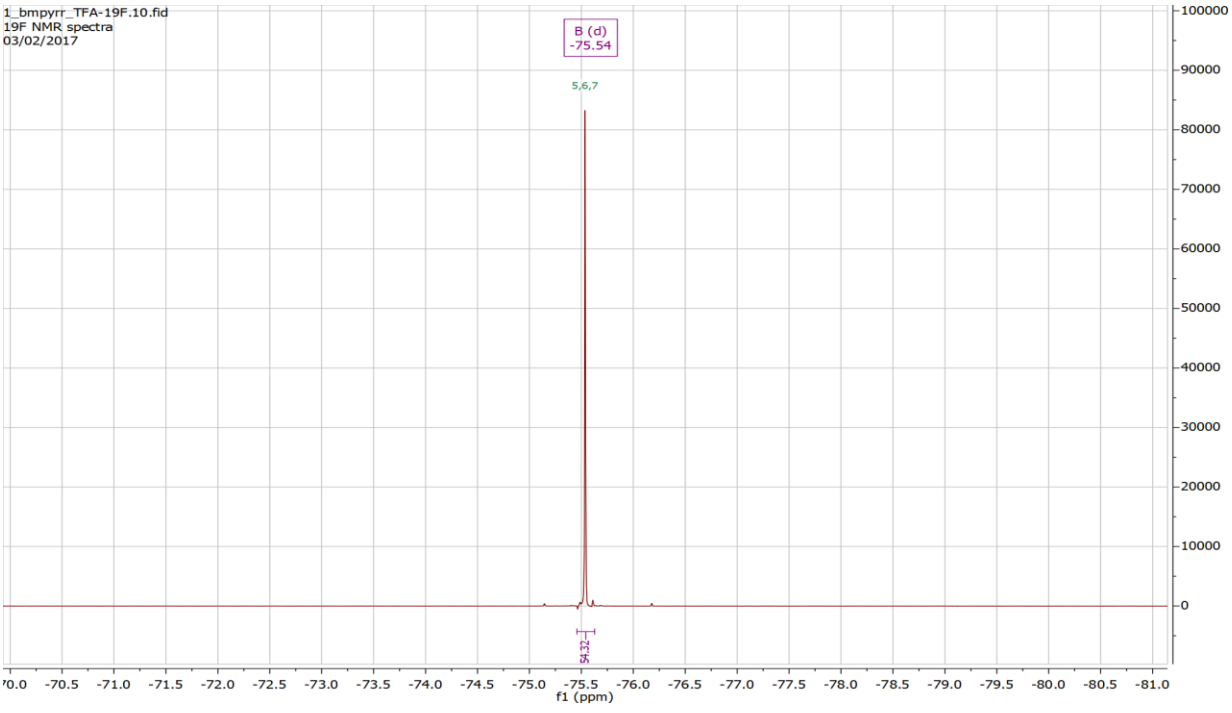

Figure 46. ^{19}F NMR spectrum of [bmpyrr][TFA] in D_2O

NMR Spectra of 1-butyl-3-methylpyridinium trifluoroacetate, [bmpy][TFA], in D_2O

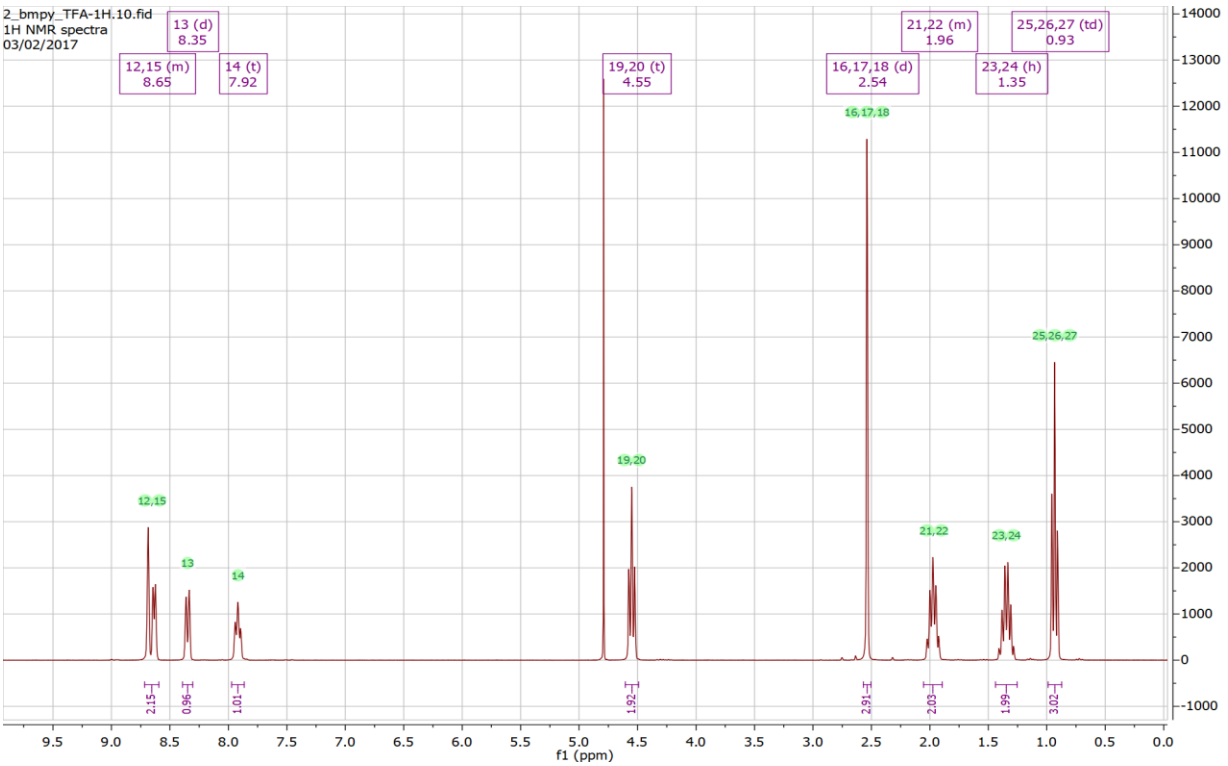

Figure 47. ^{1}H NMR spectrum of [bmpy][TFA] in D_2O

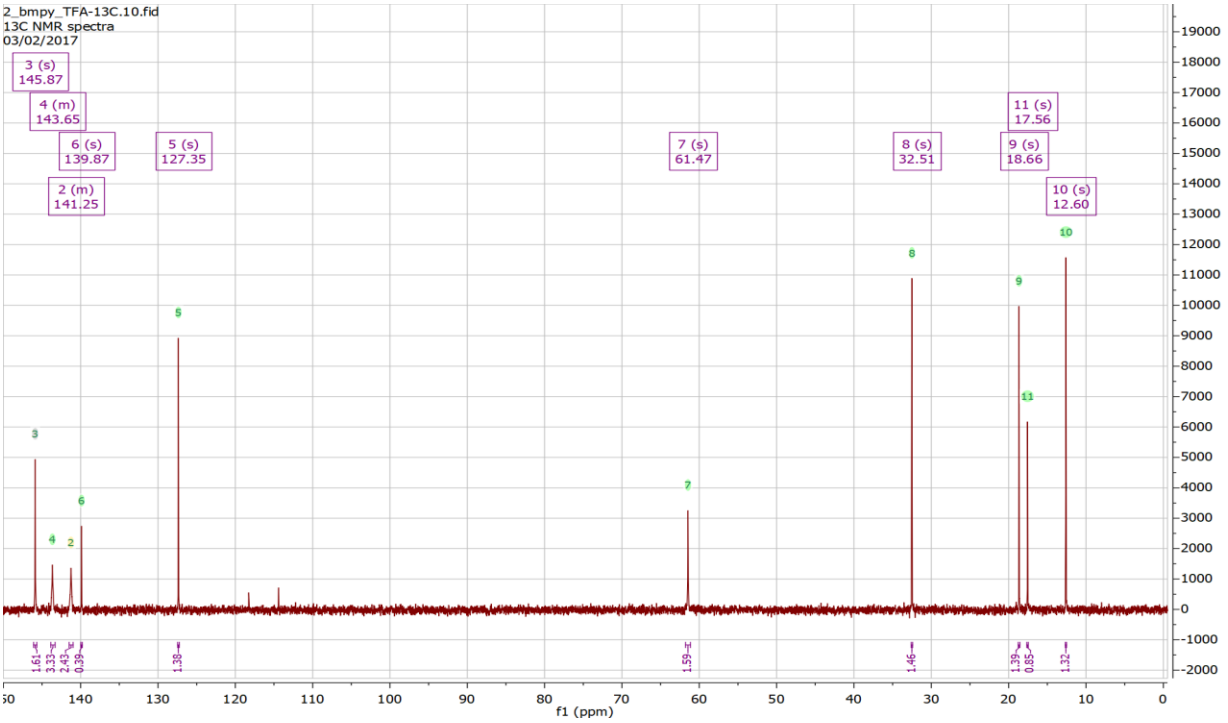

Figure 48. ^{13}C NMR spectrum of [bmpy][TFA] in D_2O

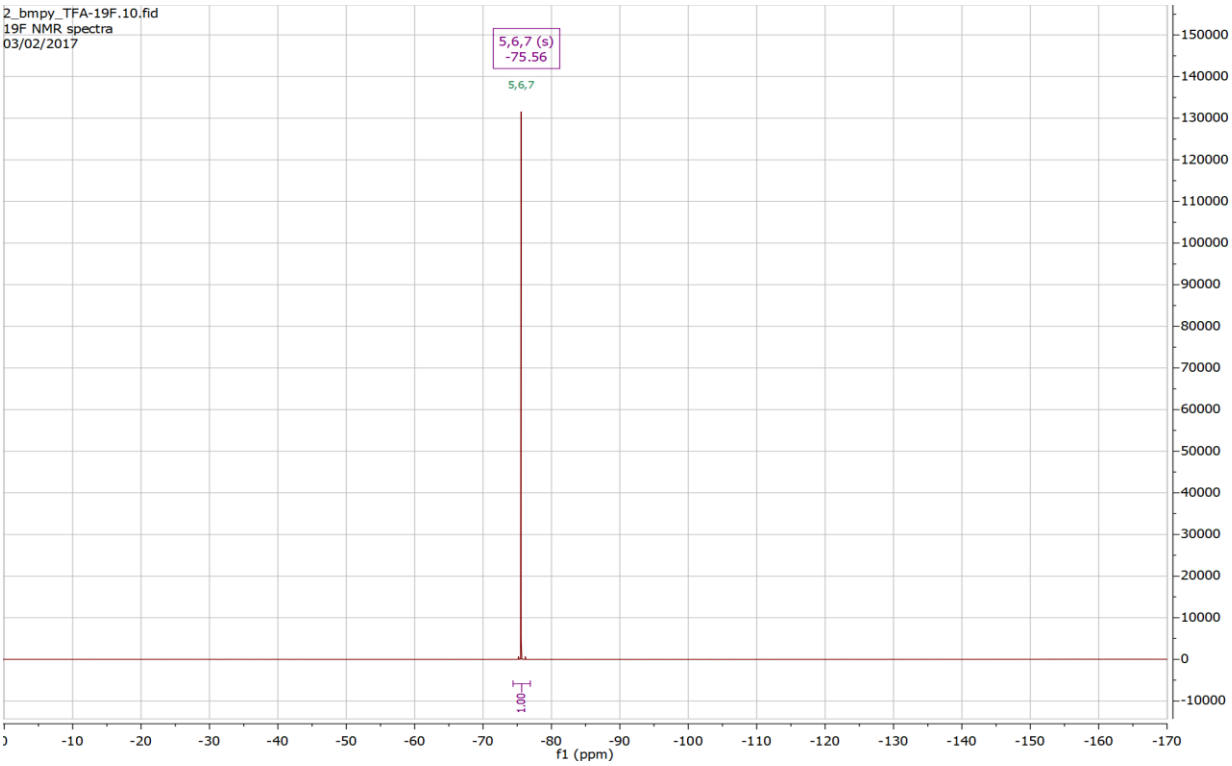

Figure 49. ^{19}F NMR spectrum of [bmpy][TFA] in D_2O

NMR Spectra of 1-butyl-2-methylpyrazolium trifluoroacetate, [bmpz][TFA], in D_2O

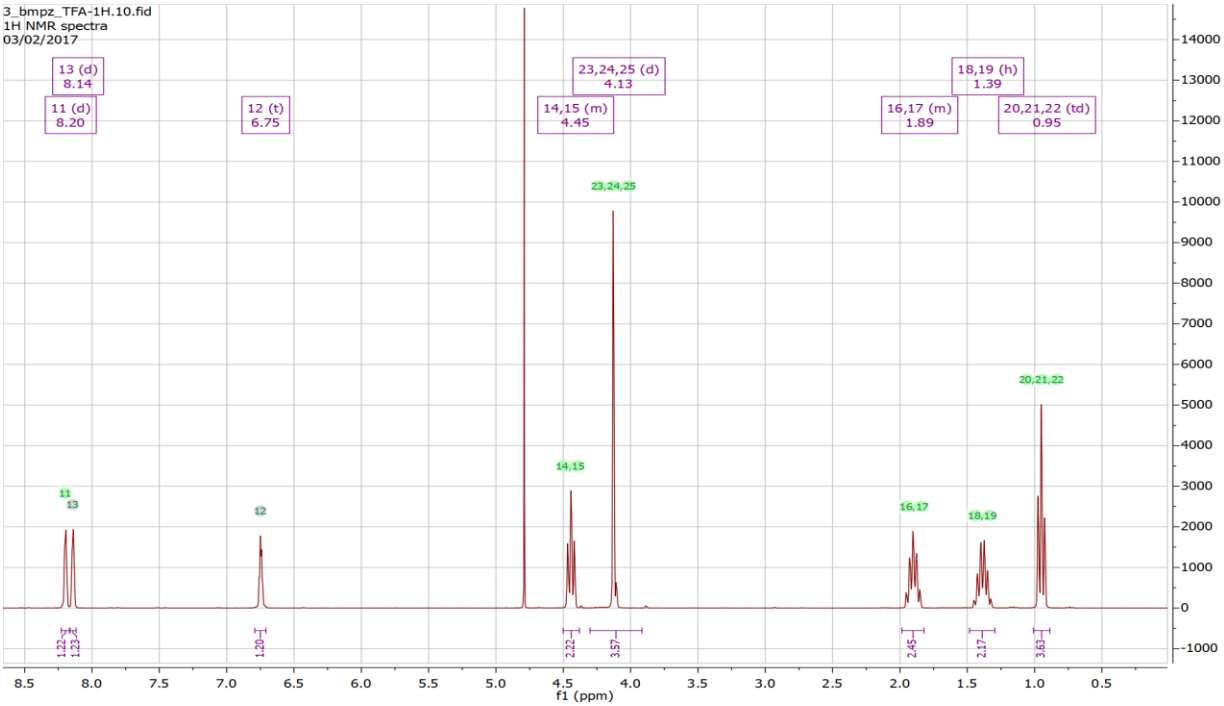

Figure 50. ^{1}H NMR spectrum of [bmpz][TFA] in D_2O

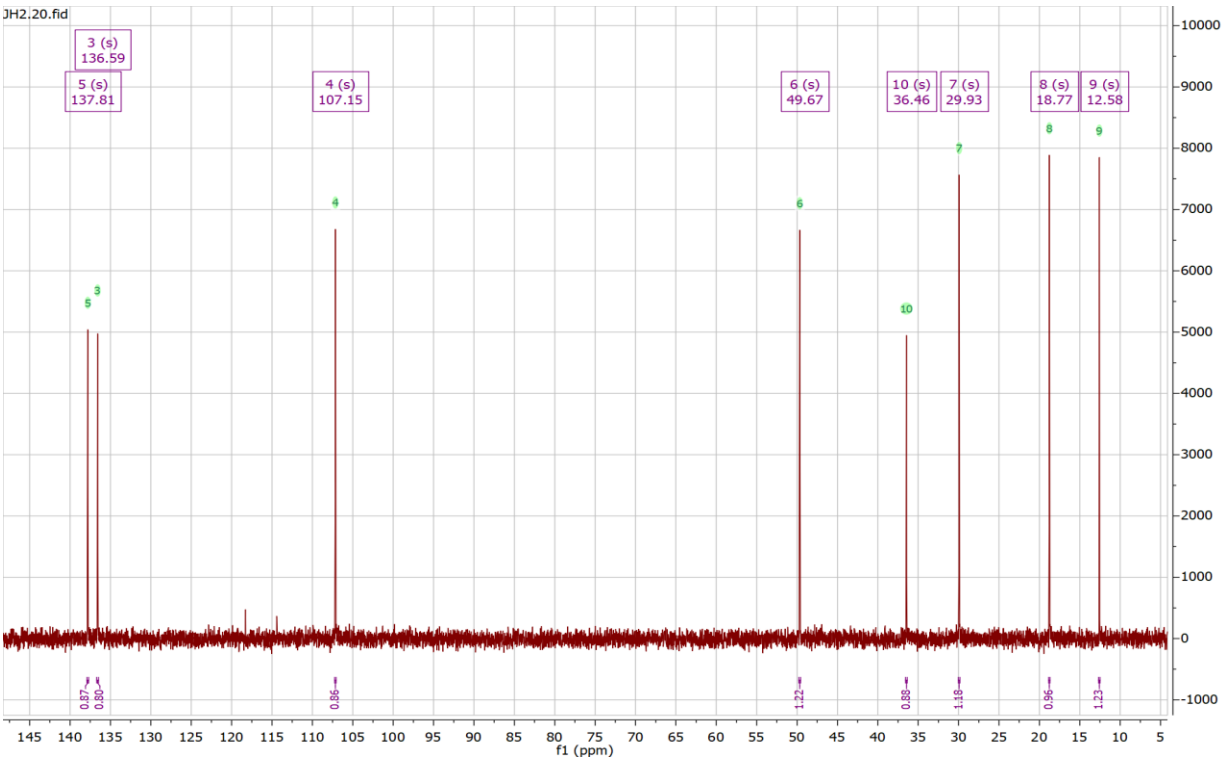

Figure 51. ^{13}C NMR spectrum of [bmpz][TFA] in D_2O

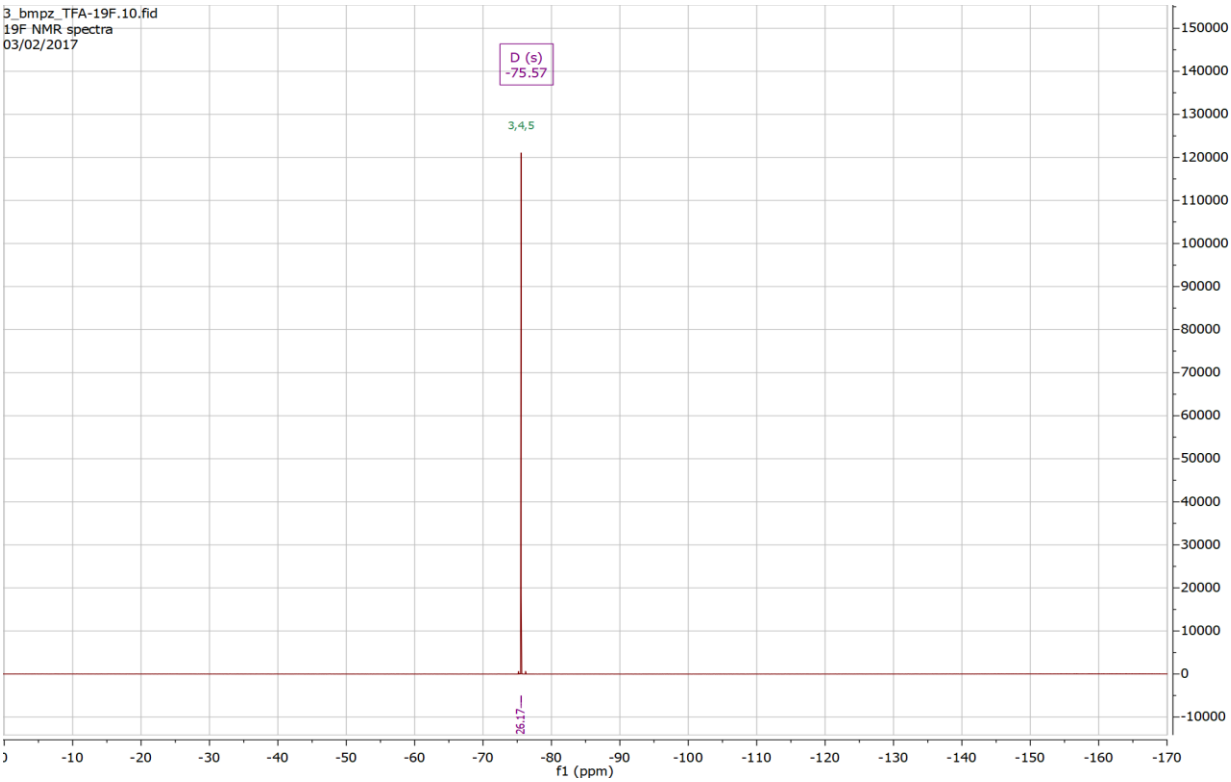

Figure 52. ^{19}F NMR spectrum of [bmpz][TFA] in D_2O

NMR Spectra of 1-butyl-3-methylimidazolium trifluoroacetate, [bmim][TFA], in D_2O

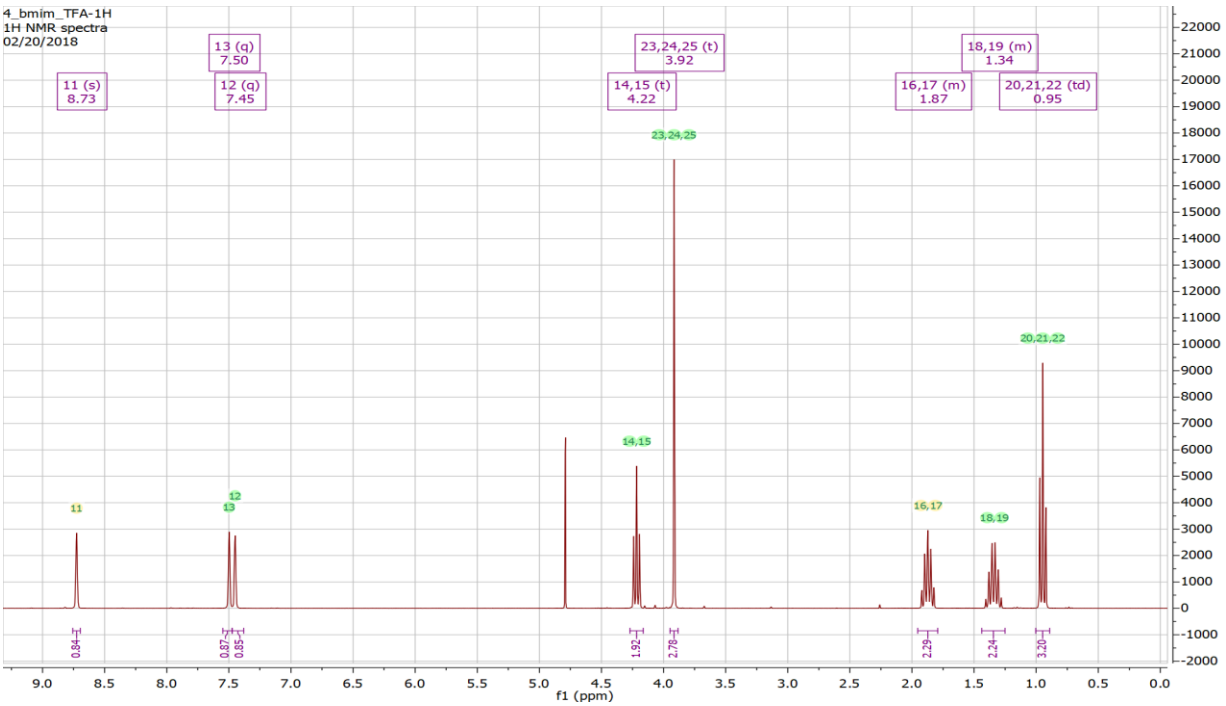

Figure 53. ^{1}H NMR spectrum of [bmim][TFA] in D_2O

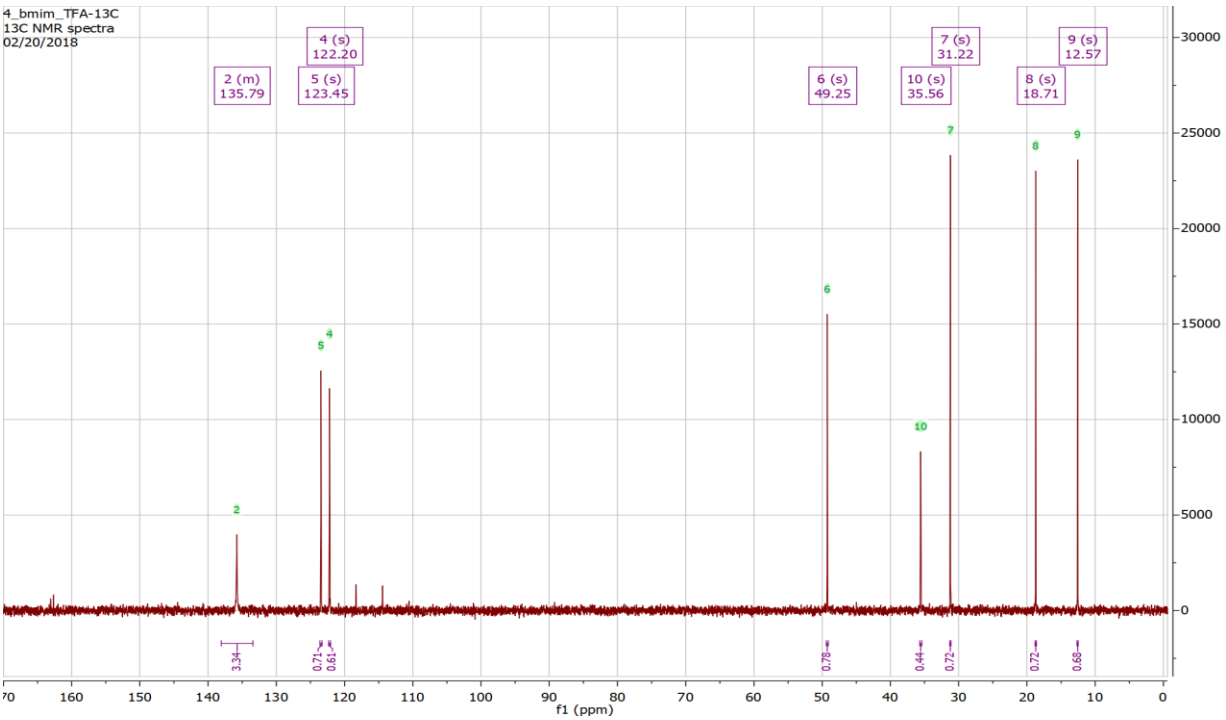

Figure 54. ^{13}C NMR spectra of [bmim][TFA] in D_2O

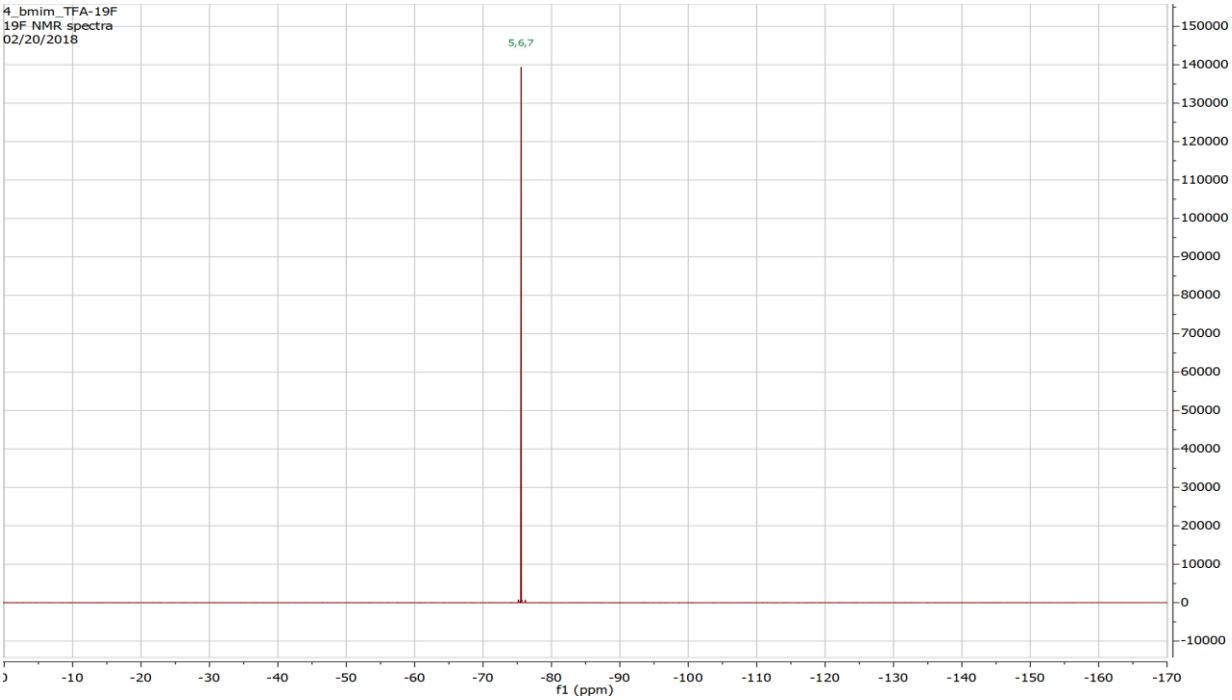

Figure 55. ^{19}F NMR spectrum of [bmim][TFA] in D_2O

NMR Spectra of 1-butyl-3-methyl-1,2,3-triazolium trifluoroacetate, [bm3tri][TFA], in D_2O

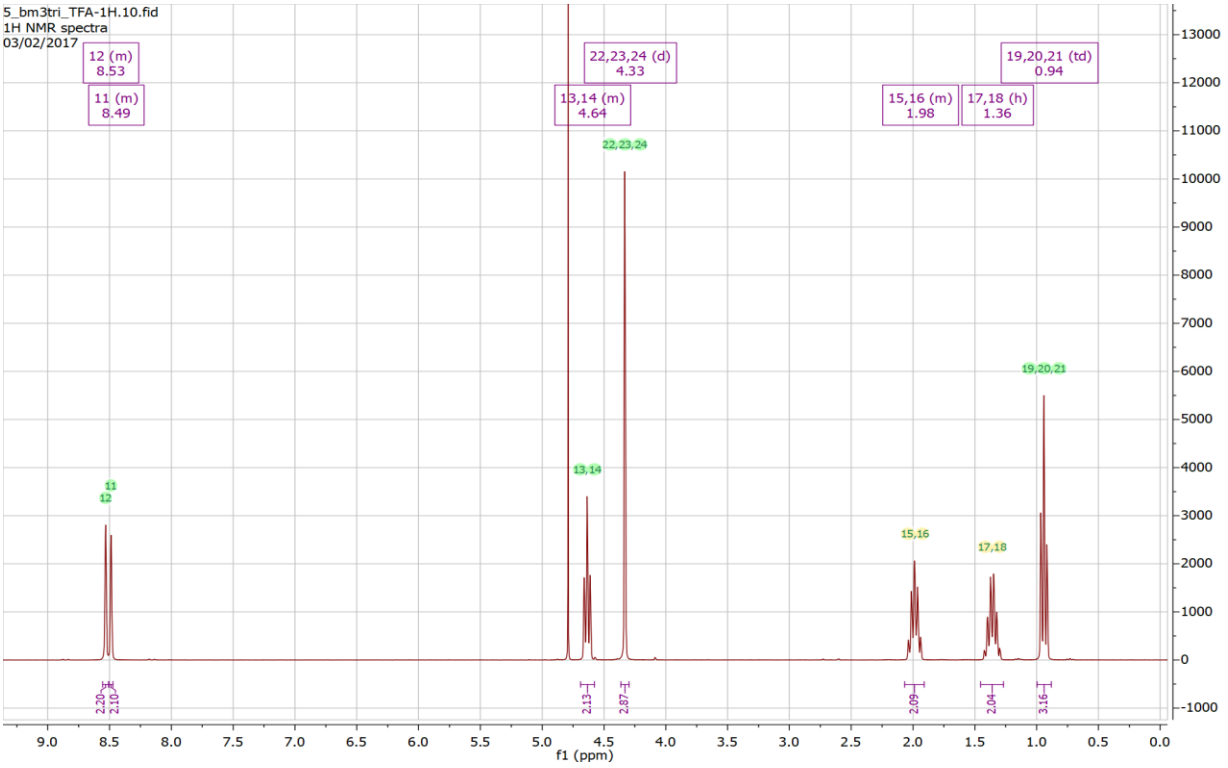

Figure 56. ^{1}H NMR spectrum of [bm3tri][TFA] in D_2O

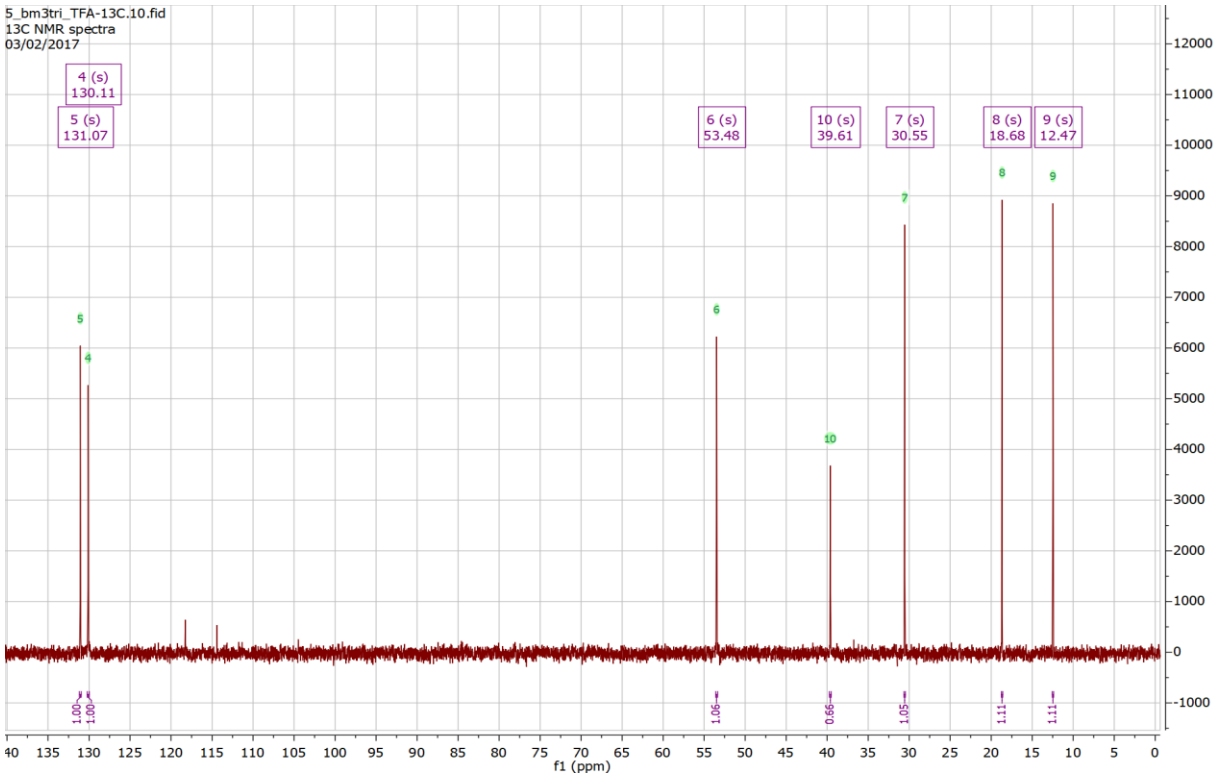

Figure 57. ^{13}C NMR spectrum of [bm3tri][TFA] in D_2O

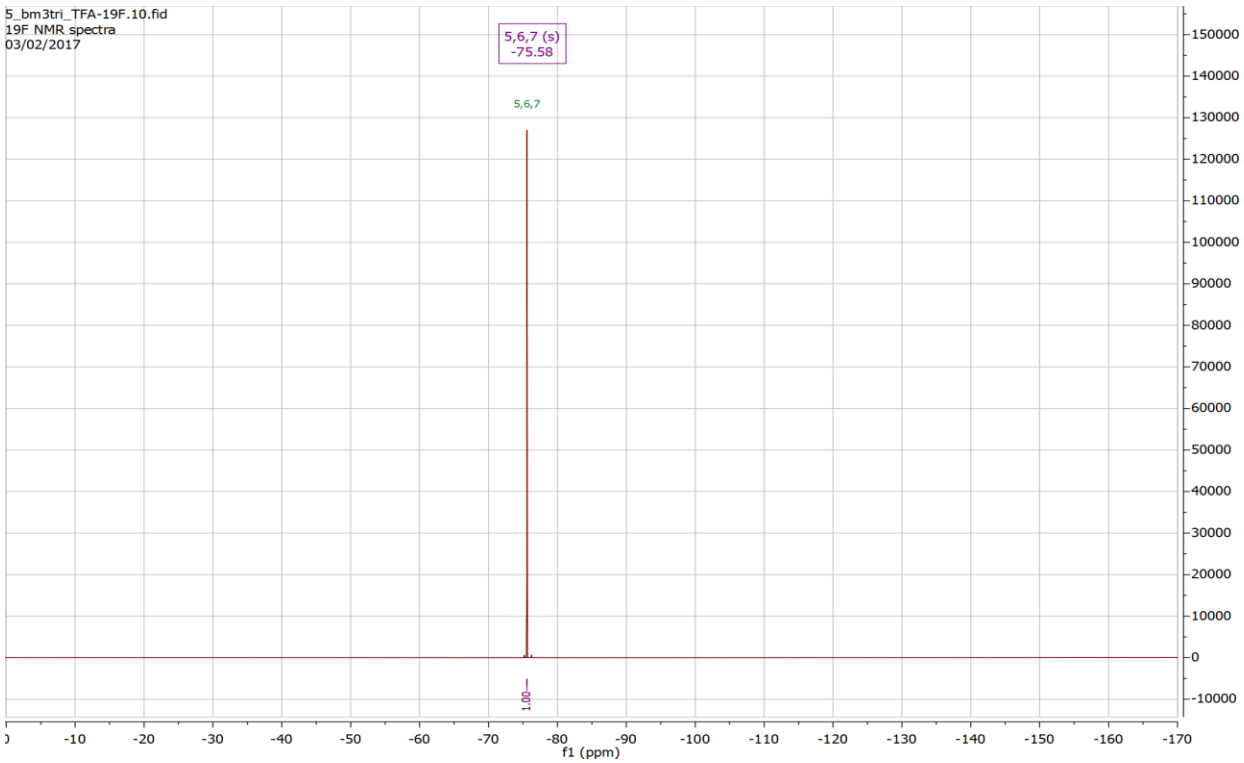

Figure 58. ^{19}F NMR spectrum of [bm3tri][TFA] in D_2O

NMR Spectra of 1-butyl-4-methyl-1,2,4-triazolium trifluoroacetate, [bm4tri][TFA], in D_2O

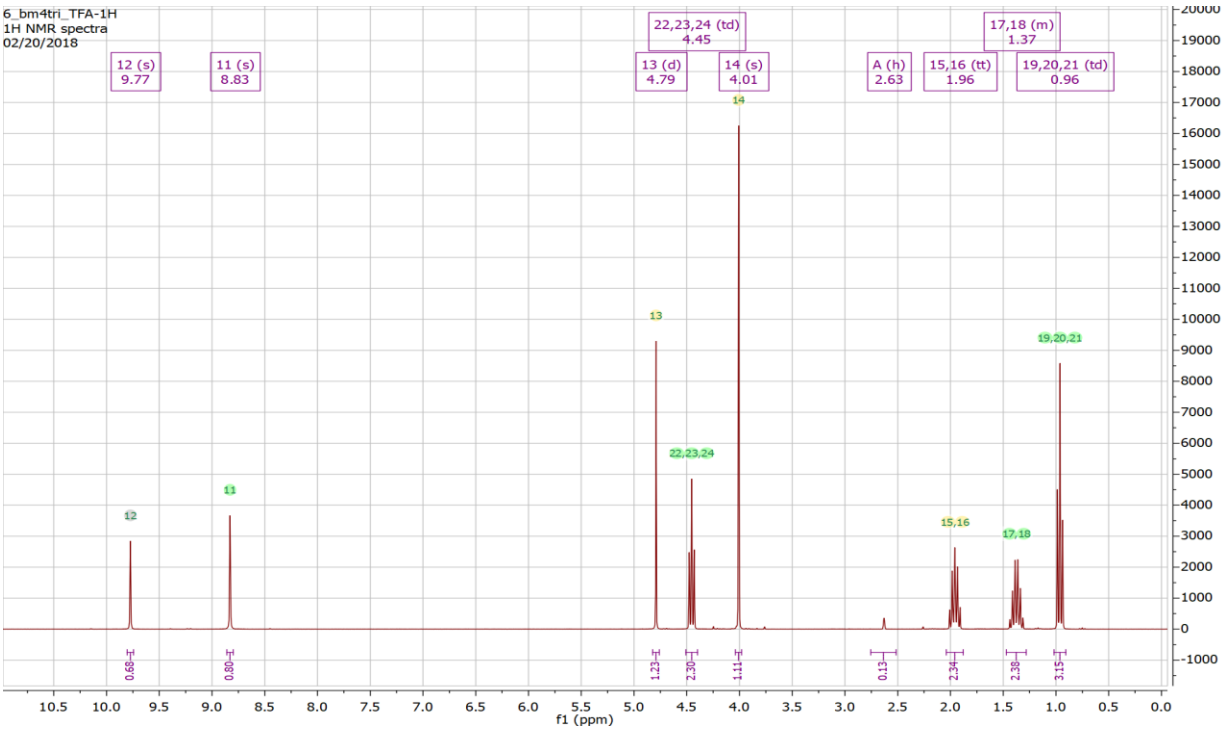

Figure 59. ^{1}H NMR spectrum of [bm4tri][TFA] in D_2O

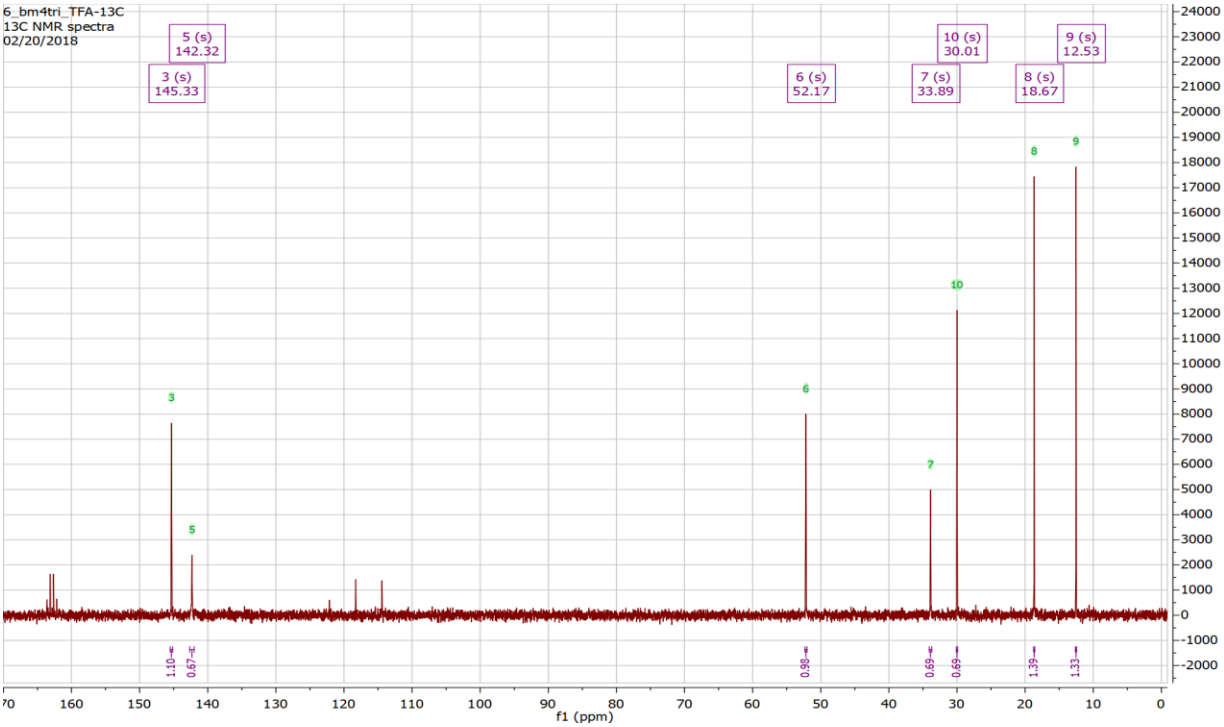

Figure 60. ^{13}C NMR spectrum of [bm4tri][TFA] in D_2O

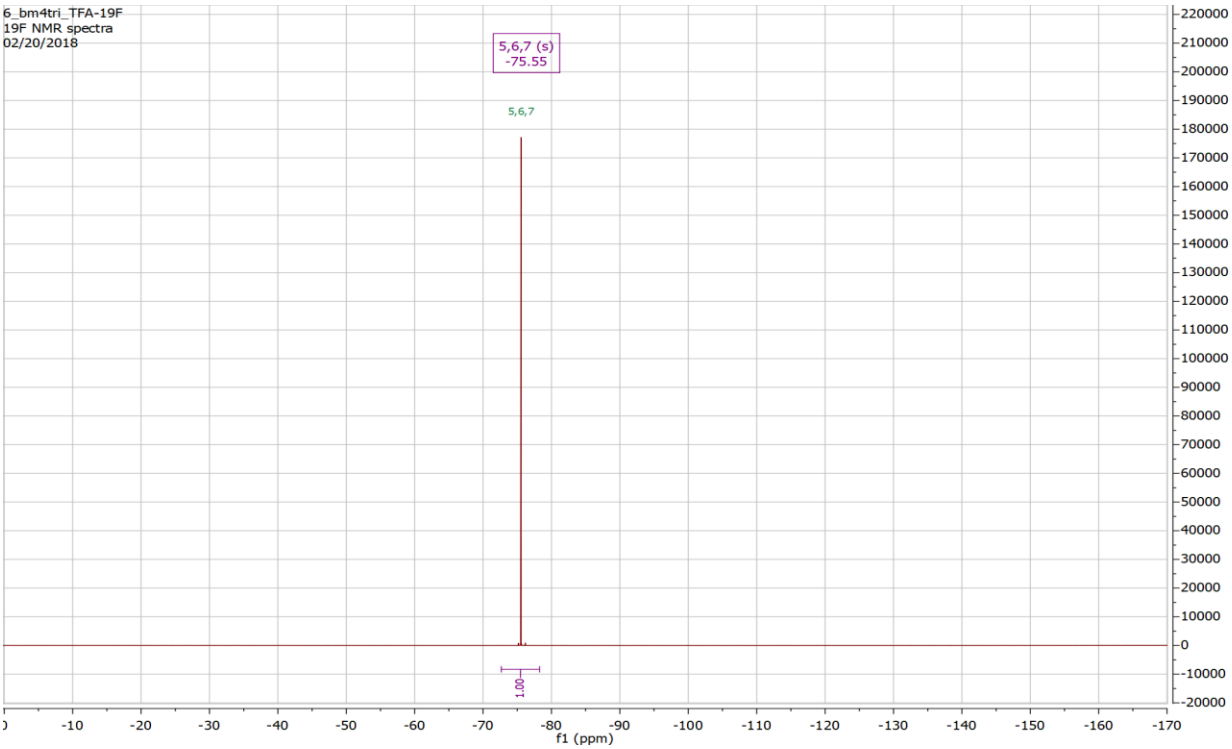

Figure 61. ^{19}F NMR spectrum of [bm4tri][TFA] in D_2O